Universität des Saarlandes

Fachrichtung Physik

Red blood cell flow in in-vivo and in-vitro network

Dissertation
zur Erlangung des Grades
des Doktors der Naturwissenschaften
der Naturwissenschaftlich-Technischen Fakultät
der Universität des Saarlandes
von

Yazdan Rashidi

Saarbrücken
2023

Tag des Kolloquiums:	15.01.2024
Dekan:	Univ.-Prof. Dr. Ludger Santen
Berichterstatter:	Univ.-Prof. Dr. Christian Wagner Univ.-Prof. Dr. Ralf Seeman
Vorsitz:	Univ.-Prof. Dr. Rolf Pelster
Akad. Mitarbeiter:	Dr. Reza Shaebani

Abstract

The precise partitioning of red blood cells (RBCs) in the complex network of our circulatory system plays a crucial role in delivering oxygen to various organs and tissues. This phenomenon, crucial for overall health, is particularly significant in the context of diseases that impair blood flow, such as diabetes and malaria. The classical Zweifach-Fung effect has provided a foundational model, explaining that daughter branches with higher flow rates collect a greater number of RBCs. However, it has been demonstrated that deviations from this model occur in small capillaries.

In the first part of this thesis, through in vivo experiments, we illuminate the phenomenon of lingering RBCs at bifurcations. Notably, we reveal that as the lingering effect increases, deviations from the Zweifach-Fung model become more pronounced. Crucially, a linear correlation emerges between the lingering effect and the deviation from Zweifach-Fung model. Our investigation also investigated the differnces characteristics of bifurcations to pinpoint the origins of this intriguing lingering effect.

The second part of our study employs in vitro experiments to analyze the development of the cell-free layer (CFL) after bifurcations, where asymmetrical CFLs manifest in the daughter branches. To facilitate these experiments, we employ a method of RBC rigidification using glutaraldehyde. Our findings paint a distinct picture: the CFL develops at a markedly higher velocity for healthy RBCs compared to rigid RBCs.

In sum, this comprehensive exploration of RBC partitioning and CFL development in microvascular bifurcations sheds new light on the intricacies of hemodynamics. Our results offer insights that extend beyond the confines of laboratory experiments, potentially impacting our understanding of blood flow in both health and disease.

Zusammenfassung

Die präzise Aufteilung der roten Blutzellen (engl. red blood cells, RBCs) im komplexen Netzwerk unseres Kreislaufsystems spielt eine entscheidende Rolle bei der Sauerstoffversorgung zu den Organen und zum Gewebe. Dieses Phänomen, das für die allgemeine Gesundheit entscheidend ist, hat besonders in Zusammenhang mit Krankheiten, die den Blutfluss beeinträchtigen, wie Diabetes und Malaria, eine hohe Bedeutung. Der so genannte klassische Zweifach-Fung-Effekt hat ein grundlegendes Modell geliefert, das erklärt, dass Gefäße mit höheren Durchflussraten eine größere Anzahl von RBCs aufweisen. Es wurde jedoch gezeigt, dass Abweichungen von diesem Modell in kleinen Kapillaren auftreten.

Im ersten Teil dieser Arbeit beleuchten wir durch in-vivo-Experimente ein Phänomen, bei dem RBCs an Verzweigungen verweilen, dem so genannten "lingering" Effekt. Beachtenswert ist, dass mit zunehmendem Verweilen (engl. lingering) an der Bifurkation die Abweichungen vom Zweifach-Fung-Modell deutlicher werden. Hiebei zeigt sich eine lineare Korrelation zwischen dem Verweileffekt und der Abweichung vom Zweifach-Fung-Modell. Wir untersuchen auch die unterschiedlichen Eigenschaften von Verzweigungen, um die Ursprünge dieses faszinierenden Verweileffekts zu ermitteln.

Der zweite Teil unserer Studie verwendet in-vitro-Experimente, um die Entwicklung der zellfreien Schicht (engl. cell-free layer, CFL) nach Verzweigungen zu analysieren, wobei asymmetrische CFLs in den Tochterzweigen auftreten. Zur Durchführung dieser Experimente verwenden wir eine Methode zur Versteifung der RBCs unter Verwendung von Glutaraldehyd. Unsere Ergebnisse zeichnen ein deutliches Bild: die CFL entwickelt sich bei gesunden RBCs im Vergleich zu versteiften RBCs mit einer deutlich höheren Geschwindigkeit.

Zusammenfassend liefert diese umfassende Untersuchung der Aufteilung der RBCs und der Entwicklung der CFL in mikrovaskulären Verzweigungen neue Erkenntnisse im Bereich der Hämodynamik. Unsere Ergebnisse bieten Einblicke, die über die Grenzen von Laborexperimenten hinausgehen und möglicherweise unser Verständnis des Blutflusses sowohl in der Gesundheit als auch bei Krankheiten beeinflussen können.

List of author's publication

- **Y. Rashidi, G. Simionato, Q. Zhou, T. John, A. Kihm, M. Bendaoud, T. Krüger, M. O. Bernabeu, L. Kaestner, M. W. Laschke, M. D. Menger, C. Wagner, and A. Darras**
  Red blood cell lingering modulates hematocrit distribution in the microcirculation.
  Biophysical journal, 122(8), 1526–1537.

- **Y. Rashidi, O. Aouane, A. Darras, T. John, J. Harting, C. Wagner, and S. M. Recktenwald**
  Cell-free layer development and spatial organization of healthy and rigid red blood cells in a microfluidic bifurcation.
  Soft Matter, 2023, 19, 6255-6266

- **S. M. Recktenwald, K. Graessel, Y. Rashidi, J. N. Steuer, T. John, S. Gekle, and C. Wagner**
  Cell-free layer of red blood cells in a constricted microfluidic channel under steady and time-dependent flow conditions.
  Phys. Rev. Fluids 8, 074202

Eidesstattliche Erklärung

Hiermit versichere ich an Eides statt, dass ich die vorliegende Arbeit selbstständig und ohne Benutzung anderer als der angegebenen Hilfsmittel angefertigt habe. Die aus anderen Quellen oder indirekt übernommenen Daten und Konzepte sind unter Angabe der Quelle gekennzeichnet. Die Arbeit wurde bisher weder im In- noch im Ausland in gleicher oder ähnlicher Form in einem Verfahren zur Erlangung eines akademischen Grades vorgelegt.

Ort, Datum

Yazdan Rashidi

The Dedication

To my lovely wife, **Hadis**, for her unwavering patience, compassion, and love.

To my parents, **Soleiman** and **Sedigheh**, and my sisters and brother, **Habibeh**, **Mahboubeh**, and **Saman**, thank you so much for everything! Words can hardly describe my thanks and appreciation for you.

Contents

List of Figures

List of Tables

Chapter 1

Introduction

Throughout history, blood has captivated the human imagination. In the rich tapestry of Greek mythology, the concept of blood held mystical qualities. For instance, it was believed that the blood flowing from the left vein of the Gorgon Medusa possessed a poisonous nature, while the blood coursing through her right arm had the power to bring the deceased back to life. These mythological narratives underscore the age-old fascination with blood, simultaneously raising questions about its purpose and its potential for both health and harm. One intriguing chapter in the story of blood is the practice of bloodletting, which involved the deliberate removal of blood from an individual with the hope of curing different diseases. This procedure, dating back to antiquity and persisting until the 19th century, was based on the belief that excess or "bad" blood needed to be purged from the body to restore health. However, in the majority of cases, bloodletting proved to be more harmful than curative, a stark reminder of the evolving understanding of blood's role in the human body. In the 17th century, a pioneering attempt at blood transfusion was made by Jean-Baptiste Denis, who endeavored to transfuse veal's blood into Antoine du Mauroy, a patient suffering from mania. While the patient initially survived the first transfusion, a tragic hemolytic accident occurred during the second attempt, leading to his death. This unfortunate incident shed light on the complexities of blood as a fluid. Remarkably, the existence of red blood cells (RBCs) began to surface in scientific discourse during the 17th century. Scientists such as Marcello Malpighi and Jan Swammerdam were among the first to mention these cellular structures. However, it was Dutch scientist Anthony van Leeuwenhoek who is often credited with the discovery of RBCs. His achievement was made possible by his remarkable skill in crafting single-lens microscopes capable of magnifying objects at least 250 times their actual size. This historical journey through the perception and exploration of blood sets the stage for a comprehensive examination of its properties, functions, and significance in the context of medical science and human health—a journey that this thesis will continue to unravel.

The RBC, also known as erythrocyte, constitutes a staggering 99% of all blood cells, playing a pivotal role in the circulatory system. It is distinctive form is that of a flexible biconcave disc, measuring approximately 8 μm in diameter. This remarkable cellular

adaptation is meticulously designed for a singular purpose: the transportation of oxygen from the lungs to the body's various tissues. The key to its oxygen-carrying capacity lies in its rich cargo of hemoglobin. Remarkably, over its relatively short lifespan of approximately 120 days, a single RBC embarks on an astonishing journey, covering an estimated distance of around 300 miles as it persistently travels the complex network of arteriovenous circulation. This extraordinary feat involves the RBC making repeated passages through the capillary bed, where the average diameter of these microvessels is only 3 μm [1–4].

The human microcirculation is an complex network of tiny blood vessels that includes arterioles, venules, and capillaries. These microvessels play a crucial role in ensuring the normal functioning of organs and tissues by facilitating the perfusion of blood [5]. One notable characteristic of blood flow within the microcirculation is its marked heterogeneity in terms of hematocrit (Ht), which refers to the volume fraction of RBCs within the blood. This heterogeneity arises as a direct consequence of the uneven distribution of RBCs, relative to the flow split, as blood travels through successive bifurcations or branching points in the microvascular system. This phenomenon is commonly known as the Zweifach-Fung effect and is a result of the prevalent presence of cell-free layers (CFLs) within microvessels [6, 7]. Under certain extreme conditions, particularly at smaller bifurcations, some of the smaller branches may receive only the plasma from the feeding branch and are entirely devoid of RBCs. This phenomenon is referred to as "plasma skimming" and was first described by August Krogh, a pioneering physiologist [8]. It represents a remarkable aspect of microcirculatory dynamics, highlighting the complex interplay between blood components and vessel geometry in the microvascular system. This phenomenon of plasma skimming underscores the complexity and adaptability of the human microcirculation, where blood flow patterns can vary significantly based on the vessel size and architecture, ultimately impacting the distribution of oxygen and nutrients to various tissues and organs.
Extensive research efforts have been dedicated to investigating the factors that influence the distribution of RBCs at vascular or artificial bifurcations, both in living organisms (in vivo) [9,10] and controlled laboratory settings (in vitro) [11–14]. In this pursuit, various studies have contributed valuable insights into this complex phenomenon. Fenton and colleagues conducted experiments using bioplastic bifurcating channels with diameters ranging from 20 to 100 micrometers. Their work identified three critical variables that significantly affect RBC partitioning: the Ht of the blood entering the bifurcation, the diameter of the vessels involved, and the fractional flows within the daughter branches [11]. These findings underscored the importance of these factors in determining how RBCs are distributed within bifurcations. These observations were further substantiated by Pries and collaborators, who examined multiple arteriolar bifurcations within the rat mesentery. Through their extensive in vivo studies, Pries and colleagues developed a robust empirical model known as the phase-separation model (PSM) [10]. This model provides a quantitative description of the phase-separation process that occurs at microvascular bifurcations. Over time, the PSM has evolved with refinements in its parametric formulation, resulting in an increasingly accurate representation of the

complex dynamics of blood flow within microcirculatory systems. The PSM, with its enhanced parametric formulations, has become a valuable tool widely used in the field of microcirculatory research. It serves as a framework for understanding and predicting how RBCs are distributed within vascular bifurcations, shedding light on the complex mechanisms that govern blood flow in the microcirculatory system.
In the realm of experimental investigations, the study of phase separation processes occurring in vivo comes with inherent challenges and uncertainties. These challenges encompass factors like the precision of photometric measurements, the influence of physiological compensatory mechanisms, and the effects of regulatory responses within the living organism. These complexities can introduce variability and make it challenging to obtain precise data in vivo. On the other hand, in vitro experiments face their own set of critical challenges that need to be satisfactorily addressed. These challenges include the need to accurately replicate the geometric realities of microvascular bifurcations, addressing issues related to concentration constraints, achieving independent measurement of plasma and cell velocities, and determining Ht levels with precision. These factors are particularly relevant when attempting to mimic and quantify the phase separation process using microfluidic bifurcation setups that involve small channels. However, recent research, both in computational simulations (in silico) and in vitro, has revealed significant deviations from this empirical model. These deviations have been observed for various reasons and in different contexts. It has become increasingly clear that RBC partitioning at bifurcations, especially in the smallest vessels within the microvascular network, tends to deviate more significantly from the predictions of the empirical model. In the reverse partitioning, the lower flowrate daughter branch receives a higher flux of RBCs compared to what would be expected based on the overall volumetric flowrate proportions. This phenomenon is supported by observations of a small attractive force that draws RBCs toward the lower flowrate channels, particularly for RBCs near the dividing streamlines [15–18].
In a study by Shen and colleagues [13], they conducted experiments using microchannels that were 20 μm wide and 8 μm deep, perfusing them with blood at different Ht levels. At low Ht, individual RBCs were observed to flow off the centerline, resulting in reverse partitioning. Additional studies, including those by Pries, Sherwood, and others, have also associated reverse partitioning behavior with disturbances occurring at nearby upstream bifurcations or multifile flow patterns in the mother branch [13, 19, 20].

Bagchi and colleagues conducted extensive numerical investigations into the time-dependent correlation between single-cell lingering times and the geometry of microvascular networks. However, these studies did not explicitly delve into the causal relationship between the lingering of RBCs and their overall distribution through bifurcations. Subsequent work by the same group combined a continuum model with cellular simulations to distinguish the effects of plasma skimming and cell screening. More recently, their research explored how changes in the fraction of lingering RBCs, specifically between rigidified and healthy cells, are related to deviations from the identity of RBC flow rates and overall blood flow rates [16, 21].

In our reasearch, we systematically investigate how the lingering of RBCs impacts

their distribution at highly confined capillary-level bifurcations within the microcirculation. This microvascular environment differs from previous studies in that the cells literally squeeze through narrow spaces, and there is a negligible CFL present, in contrast to prior investigations. To achieve this understanding, the study involves a combination of carefully designed in vivo experiments and complementary in silico simulations conducted over timescales longer than the typical lingering time, which are relevant for physiological conditions. The detailed discussion of these results can be found in Chapter 3 of the thesis [22].

Zuo and colleagues investigate how RBCs are distributed at bifurcations [23], which are points where vessels branch into two smaller vessels. Understanding this distribution is crucial for optimizing microfluidic devices and developing new strategies for diagnosing and treating blood-related diseases. In their experiments, diluted RBC suspensions were used. The results showed variations in flow rates within the vascular network, leading to significant heterogeneity in RBC concentration (Ht) in downstream generations of vessels. This heterogeneity indicated that not all branches received an equal RBCs. To delve into the underlying mechanisms causing this heterogeneity, the researchers employed parallel simulations using the immersed-boundary-lattice-Boltzmann method. Their simulations revealed that the primary factor contributing to the observed heterogeneity was perturbations occurring upstream in the CFL of blood. Additionally, they found that this deviation was not rectified between consecutive bifurcations, particularly under conditions of reduced flow, due to a suppressed hydrodynamic lift. Interestingly, the study showed that, in the dilute regime of RBC suspensions, these upstream perturbations in the CFL played a more significant role in determining RBC distribution than the local fractional flow at the bifurcation points. This led to an inherent bias where some daughter branches received fewer RBCs, or even none, despite an equal flow rate. Overall, this research highlighted the importance of considering CFL asymmetry throughout a vascular network, as it resulted in a non-uniform phase separation of RBCs that deviated from established empirical predictions [23].

In our study, we set out to investigate the impact of RBC rigidity on their behavior within a T-junction microfluidic channel. To achieve this, we intentionally induced artificial rigidity in RBCs using a substance called glutaraldehyde. We then observed and analyzed their spatial distribution at various positions within a microfluidic T-junction. Our investigation focused on how RBC distribution evolved across the width of the channel and the formation of a CFL along both the mother and subsequent daughter channels. To provide a meaningful comparison, we conducted experiments with rigidified and healthy RBCs at the same Ht, ranging from 0.1% to 5%. Furthermore, we explored the development of the CFL within the daughter vessels of the bifurcation. For a more comprehensive discussion and interpretation of the results, please refer to Chapter 4 of this thesis [24].

Chapter 2

Background

This chapter provides a comprehensive summary of the thesis, presenting a broad overview of its main contents, while emphasizing crucial findings from existing literature. The aim is to facilitate a deeper comprehension of subsequent chapters, namely chapters 3, 4.

2.1 Blood

Blood, a vital and complex physiological fluid, possesses remarkable characteristics attributed to its complex composition and crucial functions within the human body. It can be best described as a two-phase fluid, consisting of plasma and formed elements, which include RBCs, white blood cells (WBCs), and platelets as shown in Fig. 2.1. By volume, plasma accounts for approximately 54%, while RBCs make up 45%, leaving the remaining 1% mainly composed of WBCs and a small fraction of platelets. These components play distinct roles in maintaining overall health and homeostasis [2–4]. Traditionally, plasma's fluid dynamics have been viewed as that of a Newtonian fluid, with a measured viscosity ranging from $1.15mPas$ to $1.35mPas$ at the physiological temperature of 37 degrees Celsius. However, more recent studies have revealed that plasma exhibits viscoelastic behavior, as shown by investigations conducted by Brust et al. (2013) and Varchanis et al. (2018).

2.1.1 Red blood cells

RBCs, also known as erythrocytes, are the most abundant cellular components in blood. Structurally, they are relatively simple, lacking a nucleus and primarily consisting of a flexible membrane enclosing cytosol and hemoglobin. Their characteristic shape resembles biconcave discs with a thick rim and a thinner, sunken center (termed discocytes). The average diameter and thickness of RBCs are approximately 8μm and 2μm, respectively as shown in Fig. 2.2. Their volume averages around ranging from 80 *to* $100\mu\text{m}^3$, and their surface area is approximately 125 *to* $145\mu\text{m}^2$ [25].

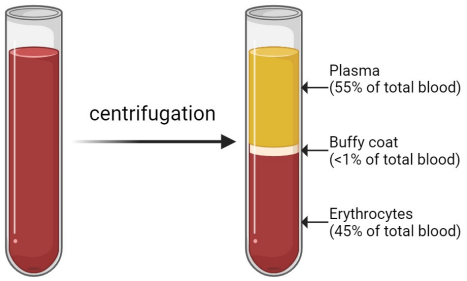

Figure 2.1: Human blood composition. plasma (water, proteins, nutrients, hormones), buffy coat (platelets, WBCs), erythrocytes (RBCs).

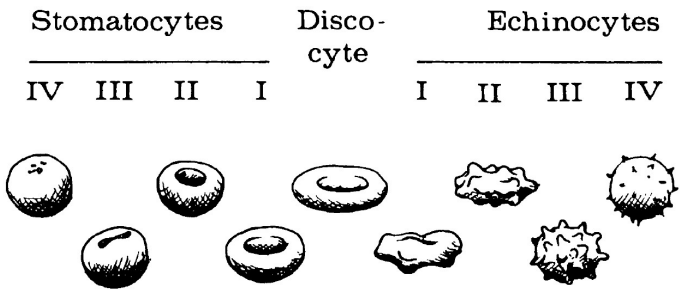

Figure 2.2: RBCs exhibit a diverse range of shapes, falling into distinct categories such as stomatocytes and echinocytes, commonly referred to as the SDE-scale. In the midst of this scale lies the discocyte shape, which is the prevailing and most typical RBC cell shape found under normal physiological conditions in healthy individuals. The image has been adapted from reference [1].

Changes in the osmolality of the surrounding media can induce distinct morphological transformations in RBCs. When exposed to a hypotonic solution, RBCs assume a monconcave cup-like shape, resulting in what is known as a stomatocyte. On the other hand, when the solution is hypertonic, spicules form on the surface of RBCs, leading to a different shape called an echinocyte. These transitions in RBC shapes are not solely influenced by changes in osmolality but can also be triggered by variations in pH, ATP concentration [26], and the addition of specific drugs like sodium salicylate (which yields echinocytosis) or chlorpromazine (which yields stomatocytosis). The shift from stomatocyte to echinocyte shapes is not abrupt; instead, it occurs gradually, resulting in a continuous shape transformation along what is known as the stomatocyte-discocyte-echinocyte (SDE) scale. This scale encompasses the spectrum of RBC shapes, ranging from the cup-like stomatocyte to the discocyte (a normal, disc-shaped RBC) and ultimately to the spiculated echinocyte [1, 27, 28].

2.1.2 Platelets

Platelets are anuclear cell fragments derived from the cytoplasm of BM megakaryocytes [29] that circulate in the bloodstream of humans for 7-10 days. With a diameter up to 3 μm, making them significantly smaller than RBCs and WBCs.
For more than a century, we have known that platelets play a vital role in hemostasis, preventing excessive bleeding. The complex molecular processes governing their adhesive function have been extensively studied. Beyond their role in clotting, platelets also have an important job in monitoring and maintaining the health of the endothelium layer (the inner lining of blood vessels) [30, 31].

However, when platelet-endothelial interactions become disrupted, they can contribute to the development of atherosclerosis, a condition characterized by the buildup of plaque in arteries. Specific proinflammatory signals lead to increased adhesion of endothelial cells to platelets, triggering the release of various inflammatory molecules from the platelets. This creates a positive feedback loop that further activates endothelial cells. Moreover, platelets bound to the endothelial surface are highly effective at recruiting WBCs from the flowing blood and enhancing their adhesion and movement to the site of inflammation. This dysregulated interplay among platelets, endothelial cells, and WBCs promotes the inflammatory process underlying the development of atherosclerosis [32].

2.1.3 Leukocytes

Leukocytes, also called WBCs, make up less than 1% of the total blood volume. They play a crucial role in defending the body against diseases and getting rid of harmful substances. Unlike RBCs, they have a nucleus. There are two main types of leukocytes: granulocytes and agranulocytes. Granulocytes, including neutrophils, eosinophils, and basophils, have spherical shapes with lobed nuclei and visible granules in their cytoplasm. They respond to various stimuli and are non-specific in their actions. Agranulocytes consist of lymphocytes and monocytes, which have fewer visible granules and are important for specific immune functions. Leukocytes leave the bloodstream and spend most of their time in tissues, defending against infections and removing damaged cells and toxins. They can move through capillary walls via diapedesis and exhibit amoeboid movement to travel within tissues. When there is an injury or infection, chemical molecules attract leukocytes to the affected area, a process known as positive chemotaxis. This leads to a gathering of leukocytes to fight off pathogens and damaged cells. Phagocytosis is a crucial ability possessed by neutrophils, eosinophils, and monocytes, as it allows them to engulf and absorb other cells and particles [33].

The production of leukocytes starts in the bone marrow from myeloid stem cells. Monocytes and neutrophils share a common progenitor, while eosinophils and basophils have separate progenitor cells. Monocytes later become macrophages in the tissues. Lymphocytes, on the other hand, develop from a common progenitor in the bone marrow and then migrate to lymphoid tissues (like the thymus, spleen, and lymph nodes) for further maturation and replication. Various factors stimulate the formation of leukocytes,

often released by mature leukocytes to recruit more of their kind to sites of infection or injury. As a result, during infections, the number of leukocytes in the body increases significantly [33].

2.1.4 Plasma

Blood plasma is the liquid part of blood that contains mostly water, proteins, minerals, hormones, and glucose. It makes up a significant portion of the blood and plays a crucial role in various bodily functions. Plasma exhibits shear thinning, meaning it flows more easily under shear stress. At low shear rates, RBCs can form temporary aggregates called rouleaux, which break up at high shear rates. The rouleaux formation is caused by the presence of plasma proteins like fibrinogen. Interestingly, during shear flow, the plasma behaves like a Newtonian fluid, meaning its viscosity remains constant. However, in elongational flow, plasma shows significant viscoelastic effects, meaning it has both elastic and viscous properties. These viscoelastic effects are observed in specialized experiments, such as the capillary breakup extensional rheometer and a microfluidic contraction-expansion device. The viscoelastic behavior of plasma is crucial to understand for medical and engineering applications related to blood flow and other biofluids [34].

2.2 Cardiovascular system

The study of microvessels began in the 17th century when microscopes were invented. Malpighi discovered the capillary system, and van Leeuvenhoek described the complex network of small blood vessels in eels' tails, even measuring the speed of RBCs in small vessels. Around 1830, a French physician named Poiseuille conducted important experiments on how blood flows in tubes to better understand the factors influencing blood flow in the vessels [35]. The findings from those studies are the foundation of our current knowledge about how blood flows in both larger blood vessels and the microcirculation. In the 1930s, a Swedish physiologist named Fåhræus explored the special characteristics of blood flow in small glass tubes. His work laid the groundwork for further research on microvascular flow and the study of blood's rheological properties (hemorheology) [36]. Since the 1960s, there has been a renewed interest in the study of the microcirculation, leading to significant advancements in understanding its mechanics [10, 37–39]. Recent experimental techniques, such as intravital microscopy and image analysis, as well as the use of fluorescent probes microscopy for in vivo measurements, have greatly improved our ability to describe the microcirculation. As researchers have developed more direct methods to study the microcirculation, they can now make meaningful comparisons between findings from in vitro and in vivo rheological experiments. This comparison is providing new insights into the unique characteristics of the microcirculation and how blood flows through these small blood vessels [1, 3, 10, 40].

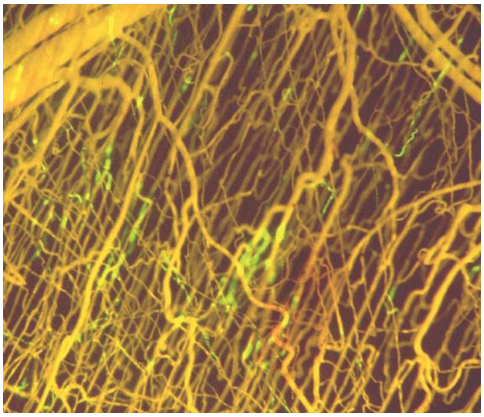

Figure 2.3: The image described is a microvascular network of the hamster cremaster muscle. The area shown in the image is approximately 1.5 $mm \times 1.5$ mm. The image has been adapted from reference [5].

2.2.1 Microvascular architecture

The flow properties of blood within the body's microvascular network are influenced by the network's geometry. Microvascular networks can vary in size, ranging from a few vessels to thousands of vessels. They are supplied by one or more feed arterioles or arteries and drained by one or more collecting venules or veins. These networks are typically three-dimensional, except in certain tissues like the mesentery. The angioarchitecture and hemodynamics of microvascular networks have been studied to some extent in various organs and tissues, including skeletal muscle, heart, brain, kidney, liver, mesentery, bone, eye, cochlea, and tumors. Each of these networks is highly specialized to meet the specific needs of the corresponding organ or tissue. Figure 2.3 illustrates an example of microvascular network of the hamster cremaster muscle [5].

The arterial vascular network consists of a series of cylindrical segments with decreasing diameter and increasing numbers of parallel channels as they progress from the aorta to the capillary beds of individual organs. The thickness of the vessel wall changes with vessel diameter. Moving from the outside inward, the vessel wall consists of layers of connective tissue, vascular smooth muscle, internal elastic lamina or basement membrane, and endothelial cells. As the vessel diameter decreases, the width of each layer, except the basement membrane and endothelium, also decreases. During dilation of an arteriole, its lumen becomes approximately circular. However, during arteriolar constriction, the lumen may change to have an irregular star-shaped cross-section, mainly due to bulging endothelial cells. Arterioles have an abundance of sympathetic nerve fibers that release a neurotransmitter called norepinephrine from varicosities in the nerves. Vascular smooth muscle and endothelial cells in the arterioles communicate with adjacent cells through gap junctions. These junctions allow the spread of electrical depolarization and provide a means of coordinating constriction and dilation responses of adjacent vascular segments by decremental conduction with a length constant of about 1 mm. This coordination ensures smooth and efficient blood flow regulation throughout the arterial

network [41].
The interplay between the increasing number of vessels and the decreasing vessel diameter and length creates a significant pressure gradient through the arterial network. This pressure gradient is most pronounced in the arterioles, which are small arteries with a high ratio of wall thickness to lumen diameter. The unique anatomical structure of arterioles allows for the regulation of blood flow primarily through changes in vessel diameter, known as vasodilation or vasoconstriction. By adjusting their diameter, arterioles can change the hydrodynamic resistance, which is the ratio of pressure drop to volumetric flow rate, following a principle similar to Poiseuille's law. For instance, a twofold uniform dilation of a vascular segment leads to an approximately 16-fold change in resistance in that segment. However, this relationship is somewhat modified by the Fåhræus-Lindqvist effect. The region of the arteriolar network where the pressure gradient is steepest is also where the most active changes in vessel diameter typically occur. This means that the small arterioles are crucial in regulating blood flow and distributing it to different tissues and organs according to their specific needs [42].

Capillaries play a crucial role in facilitating the exchange of substances between the blood and the surrounding tissues. In the peripheral circulation of humans, the total surface area of capillaries is approximately 70 square meters, providing a vast area for efficient exchange [43]. Capillaries are designed to minimize the diffusion distance between blood and tissues, allowing for rapid exchange of certain molecules while acting as a barrier to others. They are specialized to enable the exchange of nutrients and waste products, maintain fluid balance, facilitate communication between endocrine glands and target organs, allow bulk transfer between organs, and aid in immunological defense, among other functions. Fluid transfer across the capillary wall occurs through bulk flow in specialized channels and gaps between adjacent endothelial cells. For macromolecular transfer in capillaries and venules, processes like endocytosis and transcytosis are the primary mechanisms. In the brain and kidneys, specialized extraluminal structures regulate the movement of solutes and solvent molecules. Effective fluid balance between blood and tissues relies on regulatory mechanisms that maintain hydrostatic pressure within narrow limits in the capillaries [43].

The immediate postcapillary venules, which have an inner diameter of $6 - 8$ μm, collect blood from several capillaries. Similar to capillaries, these venules are simple endothelial tubes surrounded by a basement membrane, which, along with the surrounding parenchymal cells, provides mechanical support for the endothelium. The walls of larger venules have a composition similar to that of arterioles but are thinner. In skeletal muscle tissue, venules with a diameter of less than 50 μm do not have a smooth muscle layer. However, the venous network still resembles the branching architecture of arterioles, with more numerous vessels and individual segments being shorter and wider compared to arterioles. In some vascular beds, arterial and venous vessels run side by side through a portion of the network, allowing for direct exchange of vasoactive agents between the vessels [44].

2.2.2 Flow in arterioles

In arterioles, the flow velocity varies during the cardiac cycle, exhibiting a pulsatile nature. As blood travels to more distal vessels, the pulsatility becomes increasingly attenuated. When measuring velocity in arterioles with a diameter of 60 μm or less, blunted velocity profiles with some degree of asymmetry are observed. This blunting effect becomes more pronounced in smaller vessels [45–47]. In the context of a vessel with a radius R, the velocity profiles, v(r, t) , are axisymmetric and can be described in cylindrical coordinates $(\mathrm{r}, \theta, \mathrm{z})$ using an empirical relationship.

$$v\left(r,t\right) = v_{max}\left(1 - \left(\frac{r}{R}\right)^{K}\right) f\left(t\right) \tag{2.1}$$

Here, the symbol f(t) represents a periodic function that varies over time and is phase-shifted with respect to the cardiac cycle. The parameter K quantifies the extent of the blunted or flattened velocity profiles observed in these vessels [47]. Blunting is typically anticipated when the size of RBCs becomes a considerable portion of the vessel diameter. Despite this, in numerous instances, the velocity profile remains almost parabolic. Blunting of velocity profiles can also take place in larger arterioles, due to the RBCs aggregation especially at lower shear rates [5].

2.2.3 Flow in capillaries

As mentioned earlier, since the diameter of capillaries is often smaller than the size RBC, the RBCs undergo deformation, adopting shapes similar to croissants or slippers as they navigate through capillaries. The speed of individual RBCs can be used to measure the flow of cells within capillaries, the number of RBCs per unit of time (RBC flux).
Experimental studies on capillary flow have served as a fertile field for developing mathematical models to understand the motion of RBCs within capillaries. These models come in various forms, with both analytical and numerical solutions [48]. Most models treat the RBC membrane as a flexible shell undergoing deformations [49]. The primary resistance to flow is often attributed to the thin plasma film between the RBC and the vessel wall. These models have explored both axisymmetric and nonaxisymmetric scenarios, even considering flow in noncylindrical capillaries with irregularities meant to simulate endothelial cell protrusions. Research has explored the impact of the endothelial glycocalyx in capillaries. One mechanoelectrochemical model involves a mixture of fluids, a porous deformable matrix, and mobile ions [50]. Electrical charges on glycosaminoglycan (GAG) chains largely determine the glycocalyx's resistance to mechanical deformation in this model. Another model emphasizes the role of oncotic pressure generated by plasma proteins adhering to the endothelial surface layer (ESL) in determining ESL stiffness [51].

2.2.4 Flow in venules

In the venular network, flow resistance is influenced by flow rate, particularly in species where RBC aggregation occurs. RBC aggregation is more common in athletic species and less common in sedentary species. In skeletal muscle tissue, the venous vascular resistance exhibits a relationship with flow rate. For instance, in species where RBC aggregation is present, venous vascular resistance in skeletal muscle tissue is inversely proportional to flow rate. However, this nonlinearity is diminished when the muscle is perfused with RBCs suspended in Dextran-40, a substance that prevents RBC aggregation [52]. In this context, when the flow rate is reduced significantly from the control level, the venous resistance doubles. Conversely, when the flow rate is increased fourfold from the control level, the resistance decreases by 60%. This characteristic could play a crucial role in sustaining normal capillary hydrostatic pressure during substantial increases in blood flow, which commonly occurs during exercise in skeletal muscle [53].

2.3 Cell-free layer

In the complex network of blood vessels, a unique phenomenon takes place. Adjacent to the vessel walls, a distinctive area devoid of RBCs emerges, referred to as the CFL. The origin of this CFL lies in the behavior of RBCs. These cells possess the remarkable ability to change their shape and move within the bloodstream. This adaptability causes them to move away from the vessel walls, creating a space. This motion is termed "axial migration" of RBCs [54]. Interestingly, the width of this CFL varies based on factors like the concentration of RBCs in the bloodstream, known as Ht. When the number of RBCs is higher, the CFL becomes narrower. This is due to the interactions between RBCs becoming more pronounced, intensifying the collective push towards the vessel wall. Exploring this process reveals an complex interplay of forces. The formation of clusters of RBCs, within the blood flow enhances the axial migration phenomenon. These aggregates amplify the movement of individual RBCs away from the vessel wall [53, 55].
In the early 20th century, the phenomenon of RBCs and plasma separation within vascular network, as observed by August Krogh, [8]. Renowned investigators, among them Robin Fåhraeus, extensively examined this phenomenon, seeking elucidation on its implications for the rheological attributes of blood within microtubular contexts [56, 57]. Simultaneously, researchers have investigated the complex dynamics that govern the thickness of the CFL within microcirculatory vessels. They have examined its multifaceted associations with hemorheological factors, including vessel diameter, Ht concentrations, the propensity of erythrocyte aggregation, deformability attributes, the arrangement of the glycocalyx layer, and the rate of volumetric blood flow [51, 58–61]. Recent scientific has been notably aroused by the mechanisms that govern the emergence of the CFL within the microcirculation. firstly, the substantial impact of the CFL on the rheological behavior of blood within small arterial and venous pathways [53]; secondly, its amplification of the plasma skimming phenomenon within end-stage arterioles, potentially leading to a diverse distribution of erythrocytes in the complex network of

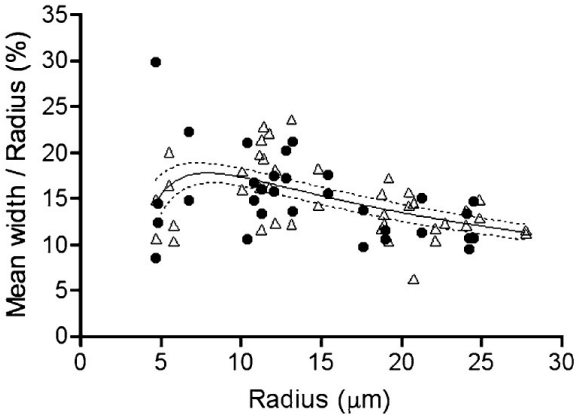

Figure 2.4: CFL thickness relative to arteriolar radius pre and post infusion of Dextran 500 with an average molecular mass of 460 kDa (indicated as before (•) and after (Δ) dextran infusion). The curve shown as a solid line represents a non-linear regression model, while the accompanying dashed lines portray the 95% confidence interval of the regression curve. The image has been adapted from reference [59].

capillaries [10, 60, 62].
In summation, the complex interplay between RBCs dynamics and plasma separation within the vascular network, has profound insights into the hemodynamic intricacies at play within the microvascular landscape. This, in turn, has enriched our comprehension of vascular physiology and pathophysiology, auguring implications that resonate across diverse domains, from basic vascular biology to clinical hemodynamics.

2.3.1 Impact of vessel diameter on the CFL

The thickness of the CFL is correlated to the diameter of the blood vessel. This relationship is demonstrated in Fig. 2.4 and has been investigated by Kim [59]. Their findings in arterioles within the rat cremaster muscle unveiled that as vessel redious ranged from 5 to 8 μm, the CFL thickness constituted slightly larger portion of the radius. However, this trend shifted as the radius increased from 8 to 25 μm, leading to a decline in the fraction from 18% to 12%.

Likewise, other in vivo analyses were conducted in microvessels (internal diameter $10-40$ μm) within isolated rabbit mesenteries, where human RBCs suspended in saline at 30% Ht were perfused [63,64]. These investigations unveiled a logarithmic correlation between the mean width of the CFL and the vessel diameter (when the vessel diameter is bigger that 10 μm) [65].

To understand the relationship between shear rate (the ratio of average flow velocity to vessel diameter) and CFL formation, three factors require consideration: vessel diameter, average flow velocity, and RBCs aggregation. In cases where the influence of RBCs aggregation on CFL formation is minimal, typical of arteriolar flows at normal arterial pressure, the CFL width generally increases with higher flow rate [59].

2.3.2 Impact of blood rheological characteristics on the CFL

RBCs aggregation, plays a pivotal role in promoting of the CFL. In controlled laboratory investigations involving small tubes, the motion of RBCs toward the center of flow became notably accentuated with heightened levels of RBCs aggregation. This effect correspondingly led to an increasing in the width of the CFL [66]. Similarly, the use of an isolated rabbit mesentery model demonstrated that as the concentration of Dextran 70, a substance that enhances RBCs aggregation, was increased, the CFL thickness proportionally increased [64]. This phenomenon contributes, in part, to the reduction of local Ht in microvessels, known as the Fåhræus effect, as well as the decline in effective viscosity, referred to as the Fåhræus-Lindqvist effect.
The deformability of RBCs is primarily governed by intrinsic factors such as the arrangement of their cytoskeleton and the thickness of intracellular viscosity. External factors which can be change by RBCs ageing, most notably the mechanical shear forces acting on the cells, also play a pivotal role. Changes in these cellular attributes can impede deformability, thereby notably affecting the flow of blood, especially when flow rates are slow. This alteration can result in decreased axial movement of the cells. Given that the creation of a distinct CFL mainly occurs under conditions of low shear rates, compromised deformability of RBCss can reduce their mobility within the bloodstream. This, in turn, extremely impacts the spatial distribution of RBCs within tiny blood vessels, consequently exerting an influence on the dimensions of the CFL. Empirical investigations have indicated a minor reduction in the thickness of the CFL when the deformability of RBCs reduce, as observed in both experiments conducted within living organisms and within controlled laboratory environments [67–69].
Ht, a important rheological parameter that significantly influences the flow resistance within microcirculatory vessels [70], also significantly effect on the development of the CFL. Considering that the width of the CFL holds an inverse correlation with the width of the core of RBCs, alterations in Ht induce changes in the volume fraction occupied by the central region of RBCs within the vessel. Moreover, the interactive forces arising from collisions between RBCs experience modifications with higher Ht levels, counteracting the axial migration of these cells. As a result, the width of the CFL reduces, by increasing the Ht of the blood [64].

2.4 Fåhræus effect

Blood's distinct nature, characterized by its particulate and non-continuous composition, gives rise to a notable phenomenon: the creation of regions near vessel walls that are devoid of cells or have a lower cell concentration. This occurrence, observed since the nineteenth century and earlier, isn't confined to in vivo contexts—it's also noticeable in glass tubes. Thus, it's not solely a result of endothelial surface layer effects. However, the exact reasons behind this occurrence remain partially shrouded in mystery. Due to the finite size or center of mass of RBCs , they can't approach the vessel wall too closely (size exclusion effect); there's a minimum distance estimated at around 1 μm, based on the

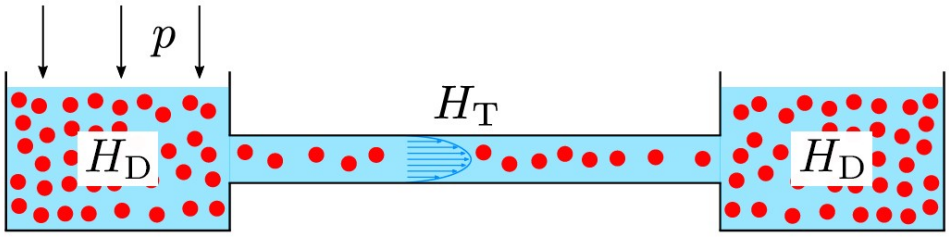

Figure 2.5: Visual representation of the Fåhræus effect: A depiction involving two reservoirs containing RBCs that are linked by a narrow tube, where the capillary's diameter corresponds to the equilibrium size of RBCs. Evidently, as cells flow within the capillary, a distinct cell-depleted layer emerges in proximity to the tube walls. As a result, these cells exhibit a higher average velocity compared to the surrounding fluid. This phenomenon is attributed to the Poiseuille flow profile. The image has been adapted from reference [72].

typical thickness of an unstressed RBC being roughly 2 μm. Nevertheless, observations suggest that this CFL often extends beyond this limit, indicating a propensity for cells to migrate from the vessel wall towards its centerline. This migration behavior has been experimentally validated and appears to be influenced by the complex mechanical interactions between deformable RBCs and the intricate flow field enveloping them. Under conditions of very low flow rates or heightened tendencies for cell aggregation, the development of a central aggregated core within the vessel can substantially increase the CFL region [71].

This lateral migration of RBCs results in the consequential effect of diminishing their concentration in the region of slower motion next to the vessel wall. Consequently, the average velocity of RBCs (v_c) increases compared to the average velocity of the entire suspension (v_b). Fåhræus observed that such a disparity in velocities leads to changes in the volume concentration of RBCs within the tube (tube Ht, H_T), relative to the volume concentration in the fluid entering or exiting the tube (discharge Ht, H_D). When the mean velocity of RBCs exceeds the mean flow velocity of the suspension, these cells move through the tube more swiftly, reducing their transit time and leading to a decrease in tube Ht relative to the discharge Ht. This phenomenon is known as the Fåhræus effect (see Fig. 2.2) [56, 57].

Based on experimental data, a parametric description of the Fåhræus effect in relation to the discharge Ht and the dimensions of the tube or vessel was formulated [20]:

$$\frac{H_T}{H_D} = H_D + (1 - H_D) \cdot \left(1 + 1.7e^{-0.415D} - 0.6e^{-0.011D}\right) \tag{2.2}$$

Here, D represents the tube diameter, which is equivalent to twice the radius ($D = 2r$) of the tube. It's important to note that the numerical values provided in this equation, as well as in the subsequent parametric explanations of rheological phenomena, are derived from outcomes obtained using human blood [20].

2.5 Fåhræus-Lindqvist effect

The complex nature of blood viscosity is governed by a multitude of factors, including Ht, plasma protein concentration, temperature, shear forces, and the geometrical characteristics of the measuring instrument. Pioneering research by Martini and Fåhræus and Lindqvist [57] uncovered a significant phenomenon: a substantial reduction in the apparent viscosity of blood within tubes spanning diameters from 400 to 50 μm. This phenomenon, termed the Fåhræus-Lindqvist effect, holds particular importance when considering the assessment of apparent viscosity in the context of blood flow within the vascular system. It is noteworthy that blood vessels exhibit a wide spectrum of diameters, spanning an impressive four orders of magnitude, ranging from large systemic vessels with diameters of around $\approx 3\ cm$ to skeletal muscle capillaries with diameters $3\ \mu m$.
The Fåhræus-Lindqvist effect has been substantiated in vitro by numerous researchers, who have illustrated that the reduction in apparent blood viscosity persists down to diameters of approximately $\approx 10\ \mu m$ [73–78]. As diameters diminish further, nearing the minimal cylindrical diameter of regular human erythrocytes ($\approx 2.7 \mu m$), Gerbstadt and Gaehtgens [76] observed a sharp increase in viscosity. Empirical characterizations of blood viscosity as a function of tube diameter have been established through the synthesis of data from various sources [10, 42, 76, 79, 80]. Such compilations serve as a foundational requirement for constructing and utilizing hydrodynamic models of the cardiovascular system, particularly in the context of the terminal vascular bed. This is essential as the contribution of microvessels of different sizes to total peripheral resistance is significantly influenced by the diameter-dependent fluctuations in blood viscosity. Hydrodynamic models for vascular perfusion have emerged as invaluable tools, facilitating the correlation of insights gleaned from comprehensive organ studies with observations derived from individual microvessels [10, 42, 79, 80].
In the effort to quantify this viscosity decrease, "apparent viscosity" denoted as μ_a [72]. While Newtonian fluids adhere to the Hagen-Poiseuille law (2.7), which establishes a direct relationship between volumetric flow rate and pressure gradient, this law doesn't apply to blood suspensions due to their non-Newtonian behavior. However, we can define the apparent viscosity μ_a as follows:

$$\mu_a = \frac{\pi r^4 \Delta P}{8Ql} \tag{2.3}$$

The hydrodynamic resistance of the fluid can be linked to the flow characteristics of a Newtonian fluid passing through a vessel with a diameter of $2r$ and a length of l. This flow is driven by a volumetric flow rate Q generated by a pressure gradient ΔP [72]. Figure 2.6 illustrates the apparent viscosity across various species and suspending media. To accommodate the shift in suspending media, the apparent viscosity is normalized by the viscosity of the surrounding medium, resulting in a term referred to as the relative apparent viscosity.

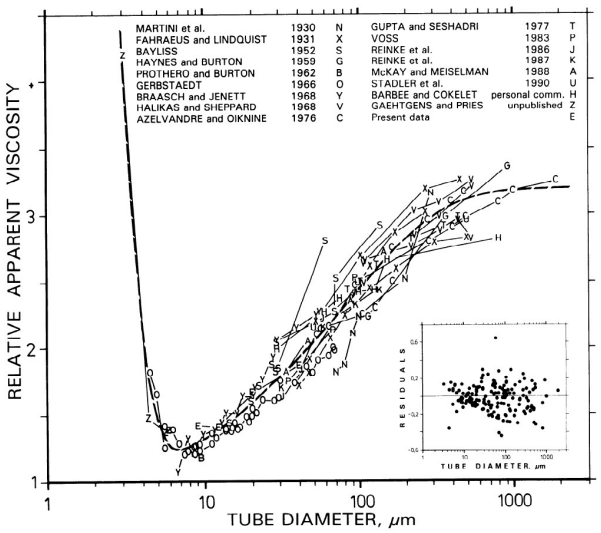

Figure 2.6: Relative apparent viscosity of red cell suspensions with a Ht of 0.45, flowing through glass tubes with inner diameters ranging from 3.3 to 1978 μm. The image has been adapted from reference [60].

2.6 Partitioning of RBCs

Understanding of blood flow and its complex correlation with the mechanical characteristics of its constituents holds the potential to drive advancements in biomedical technology. This knowledge could find applications in areas such as the development of blood substitutes and innovative transfusion techniques. An intriguing challenge in the realm of blood circulation lies in comprehending the intricacies of perfusion within the complex networks of blood vessels, particularly in the microvasculature where RBCs execute their essential roles. This pursuit gains prominence due to its direct implications on human health. A notable instance is the irregular distribution of Ht observed within the microcirculation of the heart, which has far-reaching repercussions. This anomalous distribution gives rise to zones of occlusion, a phenomenon identified in numerous individuals possessing outwardly healthy coronary arteries. These aberrant traffic zones manifest as areas deprived of adequate oxygen supply to the surrounding tissues, ultimately culminating in the onset of cardiac ischemic disease.
The dominant factor governing the non-uniformity of blood distribution in microvascular networks is the partitioning of RBCs at bifurcation points. RBCs defy passivity in their behavior; their flexible shapes and dynamic nature play a pivotal role, especially since their dimensions closely match those of blood capillaries. Within the realm of microcirculation, a widely recognized phenomenon is the Zweifach [6] and Fung [7] effect [10, 37] as shown in Fig. 2.7(a). Considering a bifurcation, where a vessel devided to the other branches, it becomes evident that the branch with a lower flow rate, we call it secondary daughter branch (SD), experiences a reduction in RBCs content in comparison to the parent vessel. Conversely, the daughter branch with a higher flow rate, we call it main

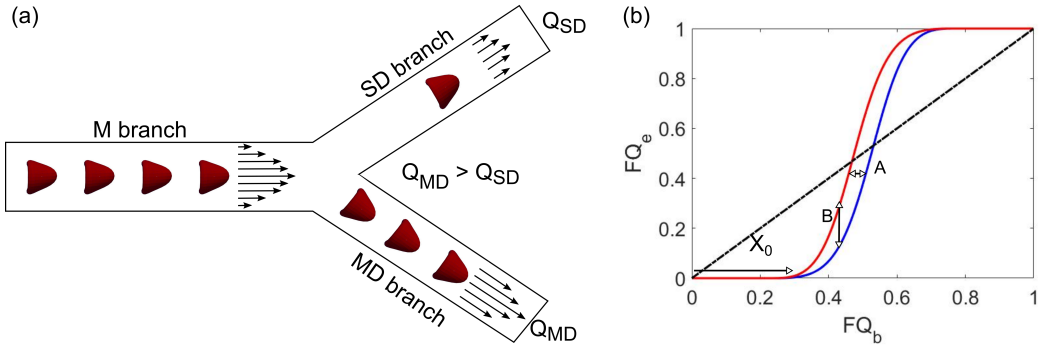

Figure 2.7: Panel (a) depicts the Zweifach-Fung effect, the daughter branches with higher flow rates exhibit an increased capacity to collect a higher number of RBCs. (b) A schematic representation illustrating the correlation between the flow of red blood cells (FQ_e) and blood flow (FQ_b) at bifurcation within the microvascular network.

daughter branch (MD), witnesses an enrichment in RBCs. In quantitative terms, if the parent vessel maintains a total volumetric flow rate of Q_M and an RBC volumetric flux of N_M, and the daughter branch with the lower flow rate, is characterized by Q_{SD} and N_{SD}, then $\frac{N_{SD}}{N_M} < \frac{Q_{SD}}{Q_M}$. Notably, as the flow rate diminishes, the Ht in the daughter branch might plummet to zero, while attaining elevated levels in the other branch. This physiological occurrence profoundly impacts oxygen and metabolite transport.

Pries et al. [20,40] conducted a study on 65 bifurcation sites within the rat mesentery. Through regression analysis, they established an empirical correlation between the division of blood flow in the two daughter vessels and the corresponding division of RBCs in these vessels as shown in Fig. 2.7(b).

$$\mathrm{FQ_e} = \begin{cases} 0, & \text{if } FQ_b < X_0, \\ 1, & \text{if } FQ_b > 1 - X_0, \\ \dfrac{1}{1+e^{-\left[A+B\,\mathrm{logit}\left(\frac{FQ_b - X_0}{1-2X_0}\right)\right]}}, & \text{otherwise.} \end{cases} \tag{2.4}$$

where $\mathrm{logit}(x) = \ln\left(\dfrac{x}{1-x}\right)$ and A, B, X_0 are related to the geometry of the bifurcation and the Ht in the mother vessel:

$$\begin{aligned} A_{MD} = -13.29\,\frac{D_{MD}^2/D_{SD}^2 - 1}{D_{MD}^2/D_{SD}^2 + 1}(1 - H_M)/D_M,\ A_{SD} = -A_{MD}, \\ B = 1 + 6.98\left(\frac{1 - H_M}{D_M}\right),\ X_0 = 0.964\left(\frac{1 - H_M}{D_M}\right), \end{aligned} \tag{2.5}$$

where H refers to the measured Ht. The subscripts indicate in which vessel the quantity is considered.

2.7 Particle focusing

In 1961, a significant discovery was made by Segre and Silberberg. They observed that in a fluidic channel, millimeter-sized particles that entered randomly could undergo lateral migration towards the channel wall. This surprising phenomenon, known as the "tubular pinch effect," occurred within a 1 cm diameter tube [81]. This observation challenged the prevailing belief at the time, which held that suspended particles would move towards the centerline of the channel, where shear forces are lower. This unexpected lateral migration behavior of particles was attributed to fluid inertia. Following this discovery, numerous theoretical investigations were conducted to provide a physical explanation for this phenomenon [82–84].
As microfluidics technology developed, fluid mechanics converged with microelectromechanical systems (MEMS), leading to further exploration of the particle migration phenomenon in smaller microfluidic channels (micrometer range). Researchers not only validated the theoretical predictions through experiments but also showcased various applications that control the potential of fluid inertia within microchannels. The combined body of research investigating fluid inertia in microchannels and its practical applications has come to be known as "inertial microfluidics" [84].

2.7.1 Fluid inertia

For a fully developed and steady-state pressure-driven flow through a tube of circular cross-section, the velocity distribution can be obtained by solving the Navier–Stokes equation:

$$\rho \mathbf{u} \cdot \nabla \mathbf{u} = -\nabla p + \mu \nabla^2 \mathbf{u} \tag{2.6}$$

Because of the geometric simplifications (no radial and swirl velocity components; $u_r = u_\theta = 0$, the flow is axisymmetric; $\frac{\partial}{\partial \theta} = 0$, and velocity is constant; fully developed in axial velocity; and $\frac{\partial u_z}{\partial z} = 0$, the convection term becomes zero and the Navier–Stokes equation is reduced to a Hagen–Poiseuille equation:

$$\nabla p = \mu \nabla^2 u_z \tag{2.7}$$

The steady-state Hagen–Poiseuille equation implies that there is neither convective momentum transfer nor acceleration, and therefore, no inertial effects regardless of the Reynolds number (Re) [85]. Reynolds number ($Re = \frac{\rho U L_c}{\mu}$): a dimensionless parameter describing the ratio of inertial and viscous forces, where ρ is the fluid density, U is the mean flow velocity, L_c is the characteristic length of the channel, and μ is the fluid viscosity).It is important to note that the flow is considered to remain within the laminar regime, characterized by Re is less than 2100. Consequently, there may be situations where Re remains nonzero while inertia is negligible. This apparent contradiction poses a challenge in the context of inertial microfluidics, as it initially suggests the absence of inertial effects in microchannels. However, it is crucial to emphasize that fluid inertia

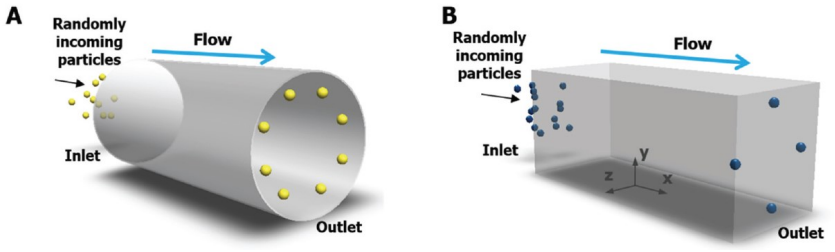

Figure 2.8: Particle migration can lead to inertial focusing in various geometries, including (A) tubular and (B) square channels. The image has been adapted from reference [87].

does indeed play a role. This paradox is resolved when minor perturbations are introduced, leading to a non-zero convection term ($\mathbf{u} \cdot \nabla \mathbf{u} \neq 0$). Therefore, when the Re is moderate, typically on the order of $\mathcal{O}(10^0 - 10^2)$, inertial effects become noticeable in microchannels under two conditions: (1) when the fluid contains particles and (2) when channel curvature is present. In these scenarios, inertia induces particle migration and/or generates transverse flow patterns, such as Dean flow in a curved channel. The initial inertial effect is referred to as "inertial particle focusing," while the latter is termed "secondary flow."" [86].

2.7.2 Particle focusing in straight tube and square channel

Inertial particle focusing presents a "passive" occurrence, wherein particles (or cells) within microchannels autonomously migrate sideways to specific locations, devoid of any external influence or force. This phenomenon is depicted in Fig. 2.8. To observe inertial particle focusing, the following prerequisites must be met: (1) confinement and (2) a shear rate gradient. The notion of confinement entails that the particle dimension should be proportionate to the channel's characteristic length (often referred to as the blockage ratio, $\kappa = \frac{a}{L_c}$, where a signifies particle diameter and L_c signifies the channel's characteristic length). This aspect is pivotal for the phenomenon of "particle-wall interaction," elucidated subsequently. Consequently, detecting inertial effects when nanoscale particles are introduced into microchannels at moderate Re values becomes complex. Secondly, a curvature within the velocity field (also recognized as a gradient of shear rate) surrounding the particle (or geometry) becomes essential. This condition enables the emergence of "inertial asymmetry" encompassing the particle/cell, thereby inciting lateral migration (refer to Fig. 2.9). Typically, a substantial shear rate gradient is induced in the velocity profile through pressure-driven flow, often facilitated by a syringe pump.

To systematically explain these conditions, consider a particle flowing within a confined microchannel, where two distinct directional forces come into play: the inertial lift forces [82, 84]. As a result of the difference between these two lift forces, the particle undergoes lateral migration across the streamlines until the net force around it becomes

zero. While a detailed theoretical explanation of particle migration from a fluid mechanics perspective is available elsewhere. Fluid inertia acting on a particle leads to inertial lift forces. In a circular channel, this results in the formation of a particle annulus (Fig. 2.8(A)), while in a square channel with its four-fold symmetry, particles migrate towards the midpoint of one of the wall's edges (Fig. 2.8(B)), contingent upon the particle's initial entry point into the channel. Importantly, it should be noted that inertial particle focusing doesn't imply the particles will accumulate or concentrate at the focusing locations. Instead, it signifies that the particles will transfer through one of the focusing positions (Fig. 2.8). The interplay between the two lift forces guides the particle either toward the channel's centerline or its wall, giving rise to the term "inertial particle migration".
For a more precise explication of particle migration mechanics, our discourse shall be confined to "neutrally buoyant particles" suspended within incompressible Newtonian fluids. Notably, the dimensions of biological cells (ranging from a few to tens of micrometers) align remarkably well with the aforementioned confinement condition. At this point, we have deferred the consideration of particle rotation; however, we shall delve into rotational effects subsequently. Due to the parabolic nature of the velocity profile as governed by the Hagen–Poiseuille equation, particles tend to migrate toward the channel wall. This directional migration can be elucidated as follows: imagine Fig. 2.9, where a particle is placed within the Poiseuille flow. Owing to the parabolic nature of the velocity curve, fluid velocity near the wall is lower compared to the flow velocity near the center of the channel. Consequently, a region of lower pressure manifests on the wall-side of the particle, exerting a force that propels the particle away from the channel's centerline. This motive force is termed the shear-gradient lift force (FSL). Conversely, as the particle draws closer to the channel wall, an interaction between the particle and the wall introduces a vertical pressure imbalance, owing to the asymmetric wakes generated behind the particle. This imbalance in the force push the particle away from the wall and toward the channel's centerline, as demonstrated in Fig. 2.9. The force guiding the particle toward the channel's center is referred to as the wall-effect lift force (FWL).

In order to witness the inertial effects within microchannels, specific conditions of length and flow rate (or pressure) need to be met. Di Carlo elucidated that the necessary channel length (L_f) for achieving equilibrium particle focusing can be determined using the following formulation [84]:

$$L_f = \frac{\pi \mu L_c^2}{\rho U_m a^2 f_L} \tag{2.8}$$

The lift force coefficient f_L, ranging between 0.02 and 0.05, and the maximum velocity U_m are pertinent in this context. This length is determined by equating the inertial lift ($F_L = f_L \cdot \rho U^2 a^4 / H^2$, where H represents the channel dimension in the particle migration direction) with the Stokes drag. To empirically observe distinct inertial particle migration, microfluidic channels typically of a few millimeters or more in length are employed. While introducing sheath fluids could potentially reduce the necessary focusing length, it's crucial to account for inertial effects on co-laminar flow generation [88].

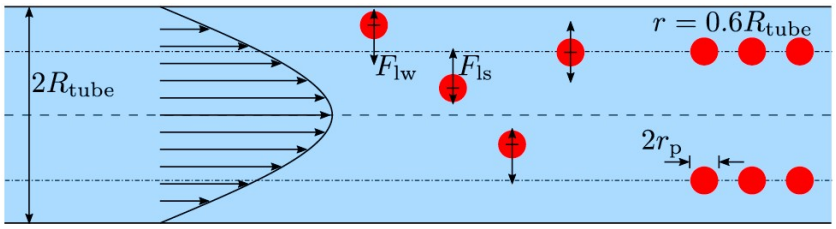

Figure 2.9: Illustration depicting the flow characteristics of a dilute particulate suspension within the intermediate to high Re range, Re = $\mathcal{O}(10^1)$. This scenario bears resemblance to the experimental configuration described in reference [81]. Within the Poiseuille flow profile, two distinct forces exert their influence on the particles: firstly, the FSL propels particles away from the channel center, and secondly, the FWL directs particles towards the center of the channel. The magnitude of these forces depend on the particles' lateral position. The image has been adapted from reference [72].

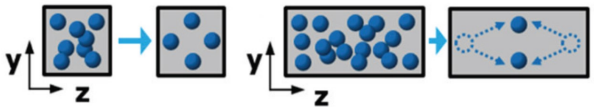

Figure 2.10: Particle focusing profiles in square channels and rectangular channels. The image has been adapted from reference [87].

2.7.3 Particle focusing in rectangular channels

Within a square channel, owing to its inherent symmetry, the phenomenon of particle focusing is directed towards one of the four equilibrium positions, as elaborated in the earlier section (see Fig. 2.8(B)). Interestingly, this scenario changes when a rectangular cross-section channel is employed, resulting in a reduction of equilibrium positions from four to two. Illustrated in Fig. 2.10, particle focusing takes place near the midpoints of the broader faces of the channel. It's important to note that whether dealing with high or low aspect ratio channels, the particles exhibit an inclination to migrate towards the wider faces. Although the channel's aspect ratio does not change the total number of equilibrium positions (which remains four), Gossett et al. have hypothesized that for rectangular channels, the equilibrium positions along the shorter faces tend to be unstable. Even the slightest perturbations from these unstable equilibrium points lead particles to migrate towards the longer faces of the channel, a phenomenon underpinned by the interaction between FSL and FWL. On a vertical axis, particles experience a significant FSL along the y-axis, causing them to move away from the centerline (as indicated by the blue line in Fig. 2.10). Conversely, on a horizontal axis, due to a flattened velocity profile along the wider face of the channel (z-axis), particles are subjected to more pronounced FWL, which push them toward the center (z-axis), resulting in the establishment of just two equilibrium positions. Importantly, recent work by Liu et al. has highlighted that in conditions of relatively higher Re, all four equilibrium positions remain stable [89].

Chapter 3

In vivo experiment

In this chapter, we provide an overview of the outcomes obtained from an experimental study conducted in vivo. The primary focus is to elucidate the impact of lingering effects on the partitioning of RBCs within microvascular bifurcations, deviating from the Zweifach-Fang prediction. The simulation part was done in collaboration with the *biofm* group at Edinburg University ("Charles" Qi Zhou, Michael Bernabeu and Timm Krueger). Specifically, we explore how the physical properties of the RBCs influence their movement through the microvasculature. The findings presented in this chapter have been published in Biophysical Journal [22].

3.1 Introduction

The main function of RBCs is to transport oxygen (O_2) around the body by blood flows, through a complex network, from large arteries to very tiny capillaries [13]. Despite being considered the model cells for studying membrane properties [90], there are still many challenges to understanding RBCs, particularly in relation to certain diseases [91]. For instance, malaria, an infectious disease killing around 400.000 people every year [92], modifies the membrane's shape and rigidity of red cells, as well as their interaction with endothelial cells [93]. Accordingly, it has been observed that these changes cause significant modifications of the in vivo blood flow [94] and can be directly correlated with the mortality [95]. For some other diseases, such as neuroacanthocytosis, the modifications of the cells' membrane properties are considered the main characteristic of the disease. Neuroacanthocytosis is a family of genetic disease where erythrocytes patients present irregular membrane with disordered, asymmetric spikes and a higher rigidity [96–98]. In human subjects, neuro-acanthocytosis is characterized by neurological disorders, such as chorea, parkinsonism or dystonia. These disorders usually appear around the twenties with a progressive degradation, usually leading to premature death. The deformed red cells are thought to be responsible for the main symptoms of the disease, but there is currently no clear mechanistic explanation [96, 99, 100]. To sum up, from a fundamental point of view, the quantitative and mechanistic link between the detailed properties of red cells and their in vivo blood flow is still a challenging question. One topic where

this link is particularly puzzling is the partition of red cells in the daughter branches at bifurcations. Indeed, uneven partition is usually observed, leading to heterogenous Hts (i.e. cells volume fraction) in the various vessels [9].
The most commonly observed situation is that the outflow with the higher flow rate collects a higher proportion of red cells [10], which corresponds to the so-called Zweifach-Fung effect. This is correlated with the Fåhræus effect, stating that the cells usually migrate away from the vessel walls [101]. Indeed, this effect implies that the cells are located in the regions with higher velocities, which are also the ones collected by the vessel with the higher flow rate [102].
However, deviations from this Zweifach-Fung effect have been reported, in particular for rigid red cells in vitro [13]. Moreover, in capillary networks, it has been highlighted that the membrane interactions of the cells with the endothelial layer at the apex of the bifurcation leads to some lingering of the cells in the bifurcation [21]. Such lingering has been shown to influence the temporal behavior of the cells in the daughter vessels, both in numerical simulations [21] and in vivo [103]. In vivo results proposed that this lingering can also actually induce a significant deviation from the classical Zweifach-Fung partitioning [103]. Thus, this study aims to investigate in vivo influence of lingering on the partitioning of RBC in micro-circulation.

3.2 Experimental setup

3.2.1 Permissions

The experiments conducted as part of this study involved the use of golden Syrian hamsters and adhered to the German legislation governing the protection of animals. The experimental protocols were subjected to review and approval by the local governmental animal protection committee, and permission was granted under the designated permission number 25/2018. Throughout the course of the experiment, the hamsters were housed in accordance with standard practices. They were maintained under a consistent 12-hour light/12-hour dark cycle, simulating a normal day-night cycle and water and food were provided ad libitum.

3.2.2 Animal preparation

For the dorsal skinfold chamber implantation, hamsters aged between 5 and 7 weeks and weighing between 55 and 70 grams were selected. The surgical procedure was conducted under deep anesthesia, employing a combination of 150 mg/kg ketamine (Serum Bernburg AG) and 0.25 mg/kg domitor (Orion Pharma) administered intraperitoneally (i.p.). To manage intraoperative pain, a single injection of carprofen (10 mg/kg, Zoetis) was administered subcutaneously (s.c.).

The surgical technique followed a previously established protocol [104]. In summary, the dorsal region of the hamster's skin was shaved, and a titanium chamber, consisting of two frames, was implanted onto the lifted dorsal skinfold (refer to Fig. 3.1). The

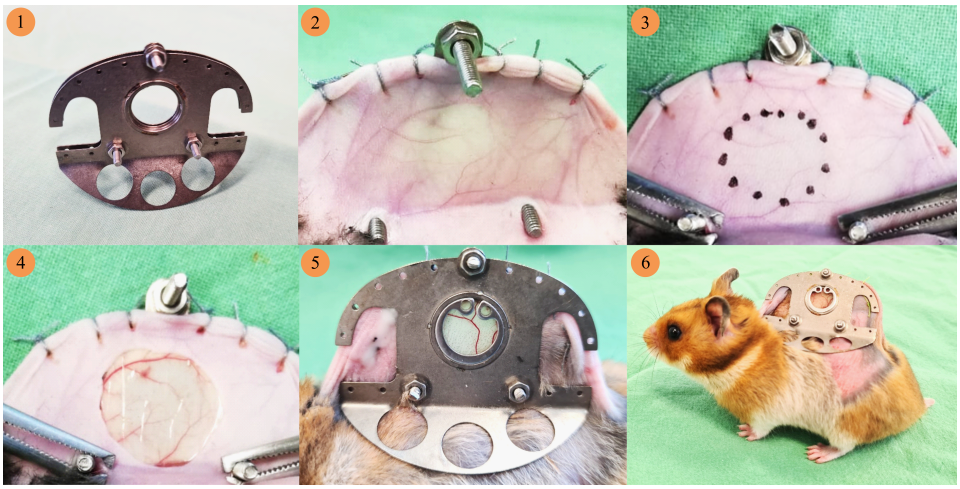

Figure 3.1: Dorsal skinfold chamber implemented on the back of a hamster. The image has been adapted from reference [22].

circular observation window on one of the frames, with a diameter of 10 mm, allowed for subsequent visualization of blood perfusion. The first layers of skin, including the cutis, subcutis, and retractor muscle, were carefully removed from the designated area to expose the striated skin muscle. A cover glass was then placed over the observation window and secured with a snap ring. Post-surgery, the hamsters were given a recovery period of 72 hours to allow for proper healing and adaptation to the implanted chamber. This recovery phase aimed to minimize any potential postoperative complications or distress in the animals.

Hamsters were anesthetized as described above prior to intravital microscopy. To visualize blood perfusion, a retro-orbital injection of 100 µl of a fluorescent plasma marker, FITC-dextran (50 mg/ml, 150 kDa, Sigma Aldrich) were injected retro-orbitally and the animals were fixed on a plexiglas stage, as illustrated in Fig. 3.2(a). Several capillary bifurcations in different areas of the chamber window were chosen for epifluorescence microscopy (Axio Examiner A1, Zeiss). FITC-dextran was excited with a 488 nm LED (Colibri 7, Zeiss) and image contrast was enhanced by simultaneously using blue light that is absorbed by hemoglobin, making RBCs appear darker. Imaging was performed with 20x (LD A-Plan, NA=0.35, Zeiss), 50x (LD EC epiplan -Neofluar, NA=0.55, Zeiss) or 100x (LD C Epiplan-Neofluar 100x, NA=0.75, Zeiss) air objectives. Video acquisition was carried out with a digital camera (Hamamatsu Orca Flash 4.0, C13440) using the software ZEN 3.1 Blue (Zeiss). A series of video frames were captured at varying intervals based on the flow velocity (100 to 170 fps). During acquisition, 2x2 binning was applied to increase image quality. An example of an obtained image is given in Fig. 3.2(b).

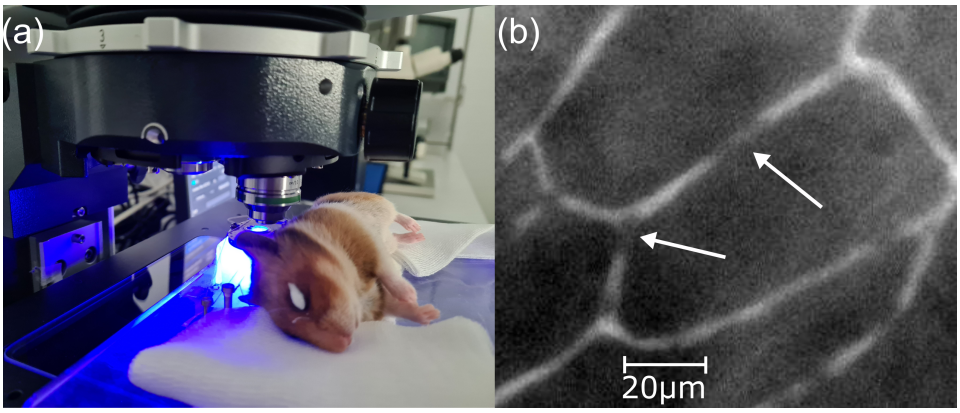

Figure 3.2: (a) Anesthetized hamster placed underneath the objective of an epifluorescence microscope. (b) Example of a microvascular network imaged by fluorescence microscopy. The dyed plasma appears bright, while RBCs in the capillaries and the surrounding tissues are dark (arrows). The image has been adapted from reference [22].

3.3 Image analysis

To minimize the impact of movement caused by breathing, muscle contraction, and expansion during the imaging process, a skinfold chamber was utilized to immobilize the animals on the microscope plane. However, slight movements still occurred, resulting in translations of the microscopic field of view in the image sequence, as depicted in Fig. 3.3(a). To determine the motion of RBCs within the vessels, a translation correction method was applied to the image sequence. Each image was translated by the maximum value obtained from its 2D-correlation with the first image in the sequence. This correction process resulted in a movie where the vessels and surrounding tissues appeared stationary, as shown in Fig. 3.3(b). Subsequently, a Gaussian filter with a standard deviation of 2 pixels was applied to despeckle the images. A mask is drawn around the vessels. The creation of this mask is facilitated by also considering the image showing the standard deviation of each pixel intensity along time, which is higher in the vessels with transient (dark) RBCs and offers a guide to the eye for the mask drawing, as demonstrated in Fig. 3.3(c). The diameters of the various vessels were calculated by determining twice the average distance from the skeleton pixels of the masks to the vessel borders, utilizing standard Matlab functions bwmorph and bwdist. This process is illustrated in Fig. 3.3(c). The image series is then inverted and binarized inside the mask area with a threshold based on a user-defined fraction of the Otsu threshold [105]. Otsu thresholding was chosen as the average intensity of the images tended to slightly flicker. However, it was observed that the automated threshold algorithm overestimated the threshold required to detect the entire RBCs. Therefore, a user-defined ratio was implemented to adjust the threshold, as depicted in Fig. 3.3(d).

The Ht H was computed from the measured area fraction ϕ_s in experimental images as $H = \phi_s \frac{V_{RBC}}{A_{RBC}\pi R_v}$, where the correcting factor contains the ratio of the cell volume V_{RBC}

(approx. $56.5\mu m^3$), the vessel diameter R_v and the measured single-cell area A_{RBC} in the considered vessel (computed for each vessel as the average of 10 single cells to exclude the interference of aggregated cells). This approach is similar to what has been done previously [13], aimed at circumventing the need of counting exact cell number for H calculation. A straightforward derivation goes as below: first we define N the number of cell in the vessel. We then consider the vessel to be approximated by a cylinder of volume $L\pi R_v^2$ with projected area LR_v. The area fraction or RBC can be calculated as $\phi_s = NA_RBC/LR_v$, whereas $H = NV_{RBC}/L\pi R_v^2$. Combining the above equation to eliminate N, which is not easy to determine from the experimental images with RBCs close to each other, we obtain the aforementioned relationship between H and ϕ.

To determine the center of mass for each detected RBCs, we employed the widely-used MATLAB function "WeightedCentroid." This function applies a weighted average calculation based on the pixel locations and intensities within the RBC region of interest. The formula used to calculate the center of mass is $R = \frac{\sum_{i=1}^{N}\sum_{j=1}^{N}[x_i,y_j]I(x_i,y_j)}{\sum_{i=1}^{N}\sum_{j=1}^{N}I(x_i,y_j)}$. Where N represents the total number of pixels within the RBC region. The variables x_i and y_j denote the coordinates of each pixel, while $I(x_i, y_j)$ corresponds to the intensity value of the addressed pixel. To calculate the weighted center of mass, the formula considers the contribution of each pixel's location (x_i, y_j) and its associated intensity $I(x_i, y_j)$. The numerator of the equation represents the summation of the products of each pixel's x and y coordinates with their respective intensities. The denominator represents the sum of all intensities within the RBC region. By dividing the weighted sum of x and y by the sum of intensities, we obtain the coordinates (R_x, R_y) representing the center of mass of the detected RBC.

After calculating the center of mass for each detected RBC, we employed a tracking algorithm, as described in [106], to determine the velocity of the RBCs. Due to various factors such as variations in light intensity along the vessels and the occurrence of collisions and transient aggregations among the RBCs, it was not feasible to reliably track all RBCs throughout their entire trajectories. However, our focus was primarily on bifurcations where the Ht levels in both the mother vessel and the two daughter vessels were low enough to allow for the distinction of individual RBCs. In these regions, we were able to successfully track and extract the spatial distribution of RBC velocity using a technique known as Particle Tracking Velocimetry (PTV). By performing PTV on the tracked RBCs within the bifurcation regions, we obtained valuable information about their velocity patterns. This analysis provided insights into the flow characteristics and dynamics of individual RBCs within the vessel network. These spatial distribution and velocity data served as a foundation for further analyses and investigations in our study.

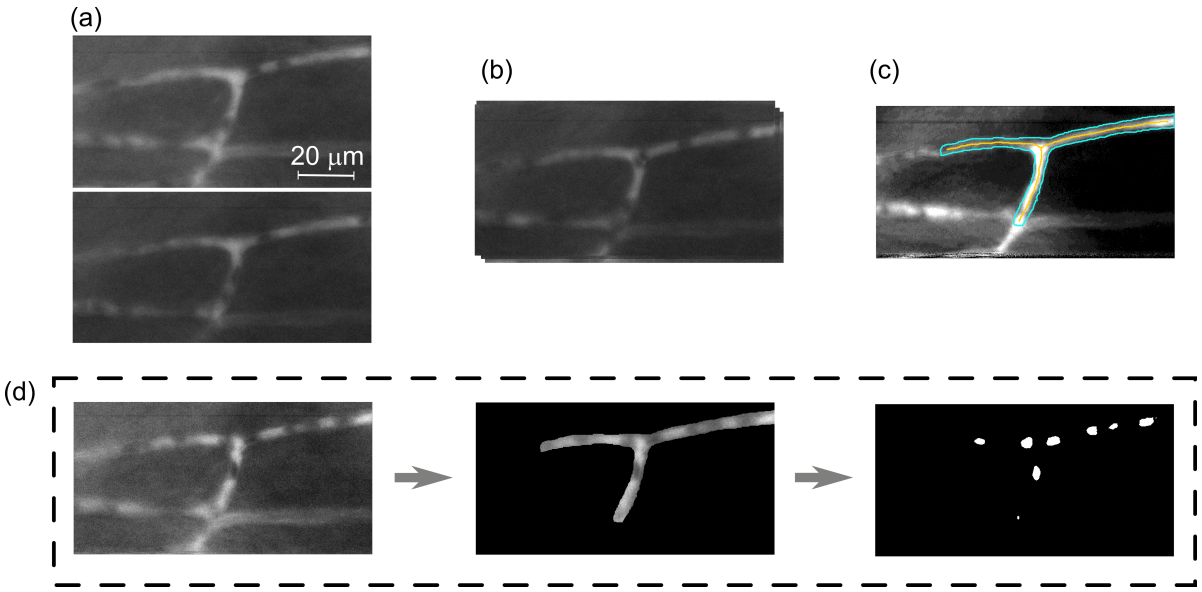

Figure 3.3: (a) Slight translations of the microscopic field of view, due to the breathing and muscle contraction and expansion of the hamster. (b) In order to remove those slight movements in the microscopic field of view, we translated each image by the maximum of its 2d correlation with the first image. A 2D Gaussian filter was applied to remove small defects in each image (to despeckle image series). (c) Mask drawn by hand around the vessels. Skeleton pixels of the mask were depicted with the yellow color, using standard Matlab functions (bwmorph). (d) The drawn mask was applied to select the Region Of Interest (ROI) of the microscopic field of view and then we binarized the images to detect RBCs. The image has been adapted from reference [22].

3.4 Numerical simulation

Complementary simulations for RBC flow in representative capillary bifurcations were conducted by the BioFM group at the University of Edinburgh. The simulations utilized *HemeLB* (`https://github.com/hemelb-codes/hemelb`) and employed the immersed-boundary-lattice-Boltzmann method, following their previous approach [17]. First, three-dimensional (3D) luminal surface models were reconstructed from binary masks of the capillary bifurcations using open-source software *PolNet* [107], assuming circular cross-sections of varying diameter along each vessel. Then the flow domain enclosed by the luminal surface was uniformly discretized into cubic lattices of fine voxel size $\Delta x = 0.25\ \mu m$, aimed at resolving cell dynamics with high resolution at the bifurcation apex. To initialize the simulation, inflow/outflow boundary conditions based on experiment-measured time-average volume flow rates were imposed at the end of the mother vessel (M) and the main daughter branch (MD, the daughter branch with higher flow rate) of each bifurcation, and a reference pressure for the secondary daughter branch (SD, the daughter branch with lower flow rate). No-slip boundary conditions were imposed at the vessel wall. The simulation time step length was $\Delta t = 1.04 \times 10^{-6} s$.

The simulation for each bifurcation was initialized with (RBC-free) plasma flow. Once the plasma flow became converged, RBCs were randomly inserted from the M vessel through a cylindrical flow inlet with constant feeding Ht (H_{F}) as measured from experiments. When RBCs reached the end of MD or SD, they were removed from the simulation domain. Each RBC was modeled as a cytosol-filled capsule with an isotropic and hyperelastic membrane consisting of 5120 triangular facets. The mechanical properties of the RBCs were governed by elastic moduli governing different energy contributions, such as shearing and bending of the membrane. The cytosol was treated as a Newtonian fluid with the same viscosity as the suspending medium, *i.e.* blood plasma. The viscosity of the RBC membrane itself was not considered. In order to probe the effect of confinement, two different RBC diameters were considered ($D_{\mathrm{rbc}} = 6\ \mu m$ corresponding to normal hamster RBCs and $8\ \mu m$ incidentally corresponding to human RBCs). Two different membrane rigidity levels (stain modulus $\kappa_s = 5 \times 10^{-6}, 5 \times 10^{-5} N/m$ for representing a normal and a hardened cell) were considered. Regarding the cell-wall interaction, a repulsive potential inversely decaying with the cell-wall distance has been implemented. High-enough resolution was used to ensure the cell-wall distance does not fall below one lattice grid.

3.5 RBCs partitioning: the Pries model

We initially assessed the average RBC velocity V and mean diameter D for each indiviual segment. Following a similar approach as previous studies [10, 103, 108], we used the following equation:

$$\langle Q \rangle = \langle V \rangle \pi \left(\frac{D}{2} \right)^2 \tag{3.1}$$

Where, $\langle Q \rangle$ represents the average flow rate, $\langle V \rangle$ denotes the average velocity, and D corresponds to the diameter of the segment. This equation allows us to estimate the flow rate based on the measured velocities and segment diameters. According to the principle of mass conservation, the total volume flow rate from the mother vessel, denoted as Q_M, is divided into the daughter branches, satisfying the equation $Q_M = Q_{MD} + Q_{SD}$. To ensure compliance with this conservation law and minimize experimental errors, the values obtained from Equation (3.1) were corrected using a normalization process described by Pries et al. in previous similar measurements [10]. Similarly, the measured erythrocyte flow rates, denoted as $E_i = H_i Q_i$, where H_i represents the local Ht, were also corrected to satisfy the relationship $E_M = E_{MD} + E_{SD}$.

The Zweifach-Fung effect is a phenomenon that describes the uneven distribution of RBCs at bifurcations within the circulatory system. According to this effect, the branch with a higher flow rate will collect a greater proportion of RBCs compared to the other branch. This observation was first reported by Zweifach and Fung in the 1950s and has been supported by subsequent research. The Zweifach-Fung effect is closely related to the Fåhræus effect, which states that RBCs tend to migrate away from the vessel walls, resulting in higher concentrations of RBCs in regions with higher fluid velocities. This effect arises due to the combination of RBC deformability. As RBCs approach a bifurcation, the branch with a higher flow rate experiences stronger hydrodynamic forces, leading to a greater influx of RBCs into that particular branch. Pries et al. established an empirical law to describe the Zweifach-Fung effect, specifically focusing on the relationship between the fractional blood flow (FQ_b) and the fractional erythrocyte flux (FQ_e) in microvascular bifurcations. The fractional blood flow FQ_b for each daughter vessel is calculated by dividing the flow rate in the respective daughter vessel by the flow rate in the mother vessel. On the other hand, the fractional erythrocyte flow rate FQ_e for each daughter vessel is determined by comparing the average Ht in the individual daughter vessel to that in the mother vessel.:

$$\mathrm{FQ_e} = \begin{cases} 0, & \text{if } FQ_b < X_0, \\ 1, & \text{if } FQ_b > 1 - X_0, \\ \frac{1}{1+e^{-\left[A+B\ \mathrm{logit}\left(\frac{FQ_b - X_0}{1-2X_0}\right)\right]}}, & \text{otherwise.} \end{cases} \tag{3.2}$$

where $\mathrm{logit}(x) = \ln\left(\dfrac{x}{1-x}\right)$ and A, B, X_0 are related to the geometry of the bifurcation and the Ht in the mother vessel:

$$\begin{aligned} A_{MD} = -13.29\ \frac{D_{MD}^2/D_{SD}^2 - 1}{D_{MD}^2/D_{SD}^2 + 1}(1 - H_M)/D_M,\ A_{SD} = -A_{MD}, \\ B = 1 + 6.98\left(\frac{1 - H_M}{D_M}\right),\ X_0 = 0.964\left(\frac{1 - H_M}{D_M}\right), \end{aligned} \tag{3.3}$$

where H refers to the measured Ht. The subscripts indicate in which vessel the quantity is considered. Pries et al. determined their model by varying the feeding Ht in single bifurcations and obtain fairly good results for single bifurcations. The question we want

to answer here is why the bifurcations scatter around the average of this well-defined relationship Eq.(3.2), knowing that the effects of the vessels geometry and the feeding Ht are already considered in their model. To do this experimentally, we will looking at a set of bifurcations, and see how their deviation from the average behavior correlate with other control parameters. In particular, the lingering seems to be a good candidate to explain such deviations in small capillaries. Indeed, the initial study of Pries et al. analyzed arteriolar bifurcations with characteristic diameters about 8µm or bigger, i.e. bigger than the main diameter of the RBCs. In this lower-confinement level, the lingering behavior, if any, is not supposed to play a significant role in the partitioning of cells. In our study, the vessel diameters range is 3.5-5.6 µm, i.e. smaller than the diameter of the RBCs. Such high confinement definitely favors the lingering of RBCs, in agreement with previously published simulations [18], since most cells have to interact with the vessel walls at the bifurcation.

3.6 Results

3.6.1 Deviation from Pries model

In Fig. 3.4(a, b, c), we present three representative bifurcations, including two Y-shaped and one T-shaped configuration. In these bifurcations, all required parameters could be extracted from the image sequences. We calculated the empirical predictions by Eq.(3.2) for each bifurcation that we could observe experimentally (9 in total), and defined the deviations from the model as $\delta ZF = |\Delta FQ_e{}^{EX} - \Delta FQ_e{}^{ZF}|$. We noted $\Delta FQ_e = FQ_{e(MD)} - FQ_{e(SD)}$ the difference in fractional erythrocyte flow rates between the main daughter vessel (MD) and the secondary daughter vessel (SD), and the expressions EX and ZF refer to the experimental data and the empirical prediction, respectively. To calculate the predicted fractional erythrocyte flow rate FQ_e^{ZF}, we utilized Eq.(3.2), where the fractional blood flow rate FQ_b was determined through experimental measurements. Figure 3.5(a) provides a schematic representation of this process. Figure 3.5(b) illustrates the comparison between the measured data and the prediction of the Pries empirical model for all the bifurcations depicted in Fig. 3.4(a, b, c).

3.6.2 Lingering effect

To detect the lingering of RBCs at bifurcations, First, we defined a circular region around the bifurcation apex with a diameter of $6, \mu$m, which corresponds to the main diameter of a hamster RBC (Fig. 3.6(a)). Red blood cells were considered to linger if their center of mass fell within this circle and simultaneously exhibited a velocity lower than the local minimum detected in the probability density function (PDF) of RBC velocities (Fig. 3.6(b)). The velocity PDF shown in Fig. 3.6(b) was obtained by considering the mother vessel and the bifurcation area. In this study, we characterized flow and cell statistics within specific time intervals ranging from 10 to 20 seconds.

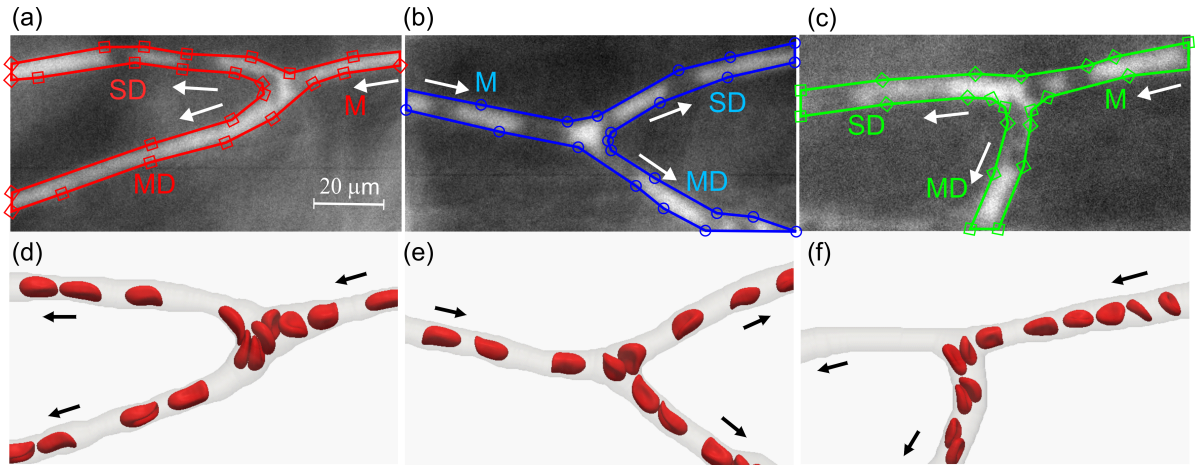

Figure 3.4: (a, b, c) Three bifurcations selected from the experiments hereafter referred to as "BIF-a", "BIF-b", "BIF-c", respectively. The mother vessel (M), the main daughter (MD) and secondary daughter (SD) are annotated and the arrows indicate the flow direction. The plasma was stained with fluorescent dye, which is bright in the images. Dark areas in the vessels indicate the RBCs. The border of the masks used to analyze the bifurcations are depicted in colored symbols. Consistent colors and symbols are used for these bifurcations throughout the article. (d, e, f) Simulated RBC flow in reconstructed bifurcations (resp. (a, b, c)), as characterized experimentally. The image has been adapted from reference [22].

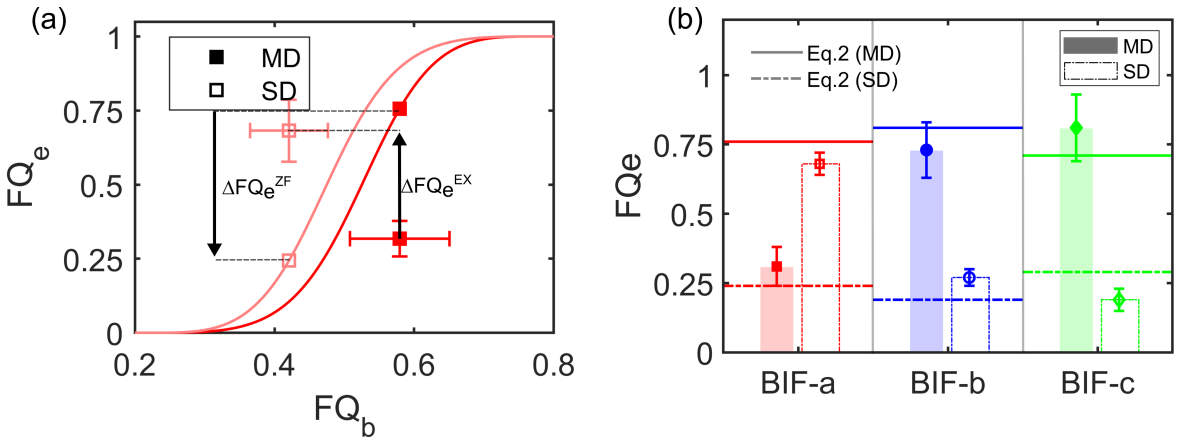

Figure 3.5: (a) Comparison of experimental RBC fluxes against the empirical predictions (for "BIF-a" as in Fig. 3.4(a)). The axes FQ_e and FQ_b are for the fractional RBC flux and fractional blood flow, respectively. We calculated deviation from the Zweifach-Fung prediction as $\delta ZF = |\Delta FQ_e(EX) - \Delta FQ_e(ZF)|$. (b) The bars show experimental results against the lines, which are empirical predictions by Eq.3.2. The data here are for the three characteristic bifurcations in Fig. 3.4(a,b,c), with consistent colors and symbols. Dashed lines and hollow symbols refer to the secondary daughter vessel (with lower fractional flow rate FQ_b). Note the inversion of the Zweifach-Fung effect for "BIF-a". The image has been adapted from reference [22].

These intervals were chosen to be longer than the transit time of individual RBCs but still short enough to ensure quasi-steady flow conditions, where no systematic trend or significant changes in the volume flow rates were observed. Within these well-defined intervals, self-consistent observables could be accurately determined. To quantify the extent of RBC lingering at each bifurcation, we first calculated the average duration of lingering events, denoted as $\langle\tau\rangle$. The total lingering time was obtained by summing the durations of all detected lingering events. We then defined the characteristic average lingering time, $\langle\tau\rangle$, as the ratio of the total lingering time to the number of RBCs. Since this time is highly correlated with the flow rate and the transit time of an RBC through the bifurcation, we normalized it by the characteristic advection time, $t_s = R/\langle V_M\rangle$, where $R = 3$ μm represents the radius of the circular region defined in Fig. 3.6(a), and $\langle V_M\rangle$ is the average velocity in the mother vessel. The time t_s serves as a characteristic time for the advection of cells through the lingering detection area (Fig. 3.6(b)). We defined the ratio of these two characteristic times as $Pe_\lambda = \langle\tau\rangle/t_s$. The ratio Pe_λ defines the equivalent of a Péclet number, since it compares two characteristic times of different transport modes at the bifurcation (lingering and advection).

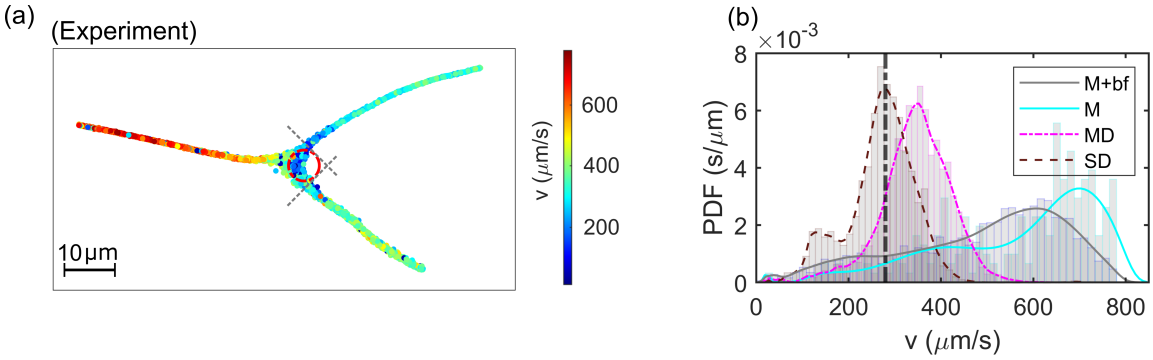

Figure 3.6: (a) Spatial distribution of RBC velocities obtained through particle tracking in experiment for "BIF-b". Lingering is considered to occur if a cell is inside the red circle (6 μm, size of a typical hamster RBC) with a velocity lower than the threshold velocity, which is determined as a local minimum in the probability density function (PDF) of velocities obtained from the mother vessel and the bifurcation area (M+bf), as shown in panel (b). For comparison, the velocity PDFs for the main and secondary daughter branches (MD and SD), and the mother vessel (M) are also shown. The image has been adapted from reference [22].

3.6.3 Lingering effect and partitioning

In Fig. 3.7(a), which includes data from 9 different bifurcations (as detailed in Table 3.1), we observe a strong correlation between the deviation δZF from the Zweifach-Fung prediction (Eq.(3.2)) and Pe_λ. The Pearson correlation coefficient of 0.74 (with a significance level of $p < 0.05$) indicates a significant relationship between these two variables. This correlation suggests that the lingering of RBCs at bifurcations, as quantified by Pe_λ, plays a crucial role in the deviation from the expected partitioning of RBCs. Interestingly, in some cases, we observed a reversal of the partitioning due to the lingering effect. This reversal is particularly evident in the (red) characteristic bifurcation highlighted in Fig. 3.4(a). In this case, the main daughter branch, which typically exhibits a higher fractional blood flow rate (FQ_b), shows a lower fractional erythrocyte flow rate (FQ_e). This phenomenon, known as reversed partitioning, has been reported in previous studies [13, 15, 23]. In our data, we only observed this reverse partitioning for the highest $Pe_\lambda \approx 1.75$.

The correlation between the lingering intensity of RBCs and their partitioning at the bifurcations, represented by Pe_λ and δZF, was also evaluated for the simulation data (Fig. 3.7(b)) using a similar approach as for the experimental data. Interestingly, a strong association was found, indicating a linear increase in δZF with respect to Pe_λ. The Pearson correlation coefficient of 0.71 (with a significance level of $p < 0.05$) suggests a significant relationship between these two variables in the simulations. However, it is important to note that the absolute magnitude of δZF and Pe_λ in the simulation data was substantially smaller compared to the experimental data in Fig. 3.7(a). In fact, the maximum P'eclet number observed in the simulations was only $Pe_\lambda = 0.65$, whereas

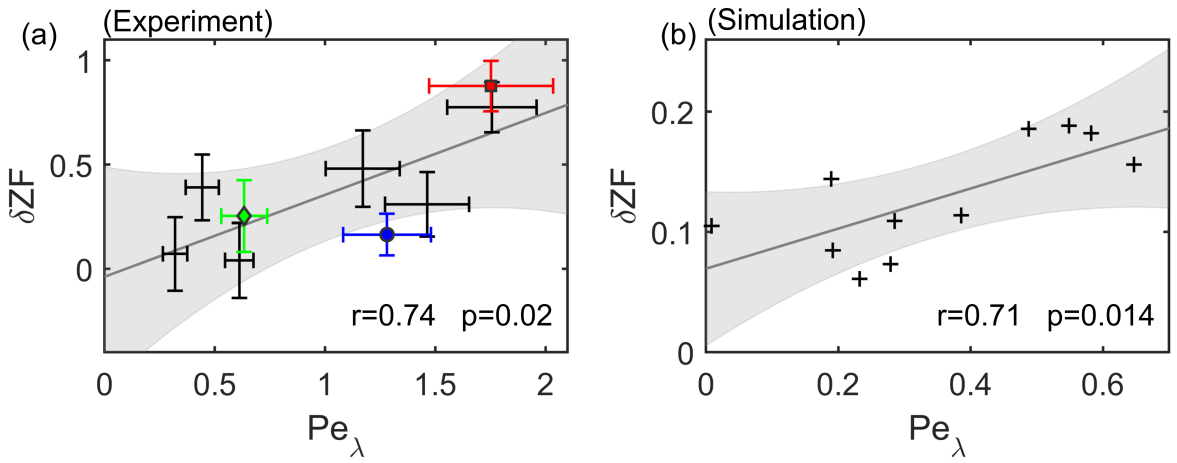

Figure 3.7: (a) Experimental deviation δZF from Eq.(3.2) as a function of the lingering Péclet number Pe_λ. The points with error bars are experimental data, and the solid line shows linear regression fitting of the data points, with the shaded area indicating 95% confidence interval prediction from the fit. All data gathered from 9 bifurcations (including the three bifurcations "BIF-a" "BIF-b" "BIF-c" in Fig. 3.4(a,b,c)) are included in this graph. The Pearson-r correlation coefficient (n=9) is $r = 0.74$ ($p = 0.02$). (b) Correlation between δZF and Pe_λ in simulations (n=12). The crosses are simulation data and the solid line shows linear regression fitting of the data points. The Pearson-r correlation coefficient is $r = 0.71$ ($p = 0.014$). The image has been adapted from reference [22].

Exp	N_{RBC}	Physical time (s)	D_M (μm)	$A_{RBC}(\mu m^2)$	Ht_M	Q_M	Q_{MD}	Q_{SD}
EX1	131	11.57	3.65	21.67	12%	5384	3119	2265
EX2	284	14.53	3.47	20.43	12%	7571	4228	3343
EX3	348	17.01	5.66	19.98	6%	9182	6500	2682
EX4	418	11.57	4.88	19.8	9%	10286	6047	4239
EX5	389	13.15	3.62	20.08	13%	5238	2754	2484
EX6	312	11.26	3.99	19.78	15%	7409	5529	1880
EX7	173	11.26	3.58	20.01	11%	3747	2639	1108
EX8	99	11.26	4.84	19.6	5%	3913	2204	1709
EX9	289	22.5	4.34	19.37	11%	5424	3864	1560

Table 3.1: Spreadsheet of conducted experiments. Data depicted in color corresponds to the representative bifurcations as in Fig. 3.4. The unit of the Q is $\left(\frac{\mu m^3}{s}\right)$.

the experiments reached a maximum value of $Pe_\lambda = 1.75$. This discrepancy can be attributed to differences between the simulation and *in vivo* experimental conditions. One potential factor contributing to this difference is the absence of the endothelial surface layer (ESL) and the RBC glycocalyx in the numerical model. The ESL, with a thickness of approximately 0.4-0.5 μm, and the glycocalyx play important roles in the interactions between RBCs and the vessel wall. While a repulsive cell-wall potential was implemented in the simulations, the complex interactions involving the ESL and glycocalyx were not fully captured. The ESL, with its ciliated structures, may introduce additional confinement or attraction forces on RBCs, which could affect their behavior and the partitioning at bifurcations [3, 109, 110]. Since these effects have not been fully characterized in the literature, they were not explicitly included in our simulations. Nevertheless, despite these limitations, the qualitative similarity between the experiment and simulation results regarding the correlation between the lingering Péclet number Pe_λ and the deviation from the Pries model is noteworthy. It suggests that even without capturing all the intricacies of the in vivo environment, the simulation results still exhibit a similar trend. It emphasizes the importance of considering the lingering effect and its influence on RBC partitioning at bifurcations. It is worth mentioning that, in the simulations, no instances of reverse partitioning (or inversion of the Zweifach-Fung effect) were observed. This observation aligns with the experimental findings, where reverse partitioning only occurred for bifurcations with $Pe_\lambda > 1.75$.

Similarly, we calculated the deviations from the linear partitioning, $FQ_e = FQ_b$, and results are shown in Fig. 3.8(b). The Fig. 3.8(b, d) shows the correlation between the lingering Péclet number and various deviations from both behaviors (Eq. (2) and linear partitioning). We noted $\Delta_{prediction} = \Delta FQ_e{}^{EX} - \Delta FQ_e{}^{prediction}$ the difference of the experimental result with the various predictions (Eq(2) and $FQ_e = FQ_b$), while $\delta_{prediction} \equiv |\Delta_{prediction}|$. Keeping the sign shows if the lingering effect can enhance ($\Delta_{prediction} > 0$) or decrease ($\Delta_{prediction} < 0$) the heterogeneity partitioning of RBCs, with respect to both Pries model and the linear partitioning. However, both positive

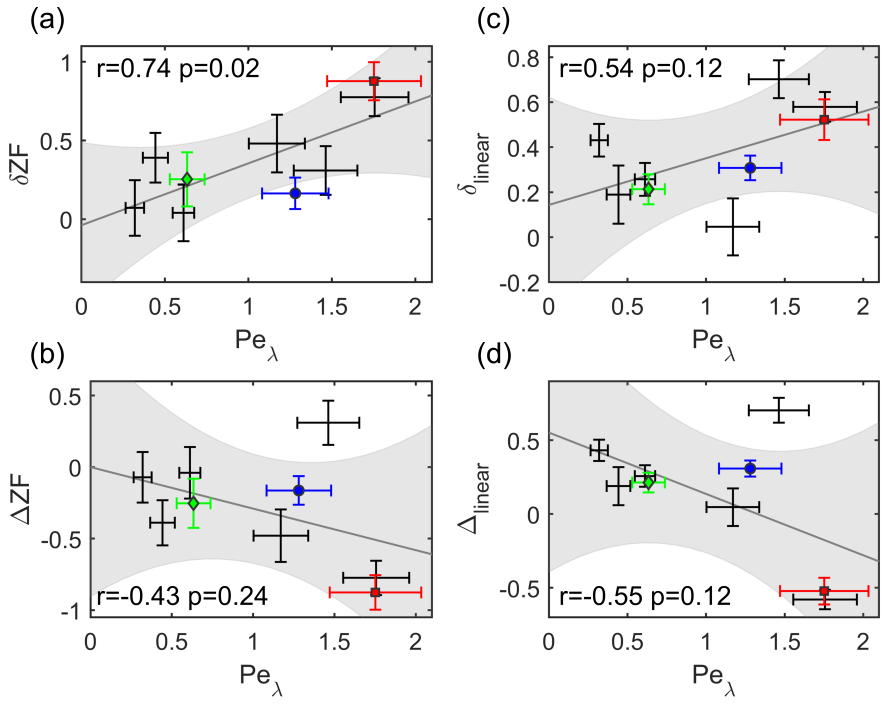

Figure 3.8: Deviation of the Pries model and linear partitioning as a function of the lingering Péclet number Pe_λ. (a, c) Absolute difference of the experimental result with the prediction of Eq.(3.2) and linear partitioning, respectively. (b, d) Difference of the experimental result with the prediction of Eq.(3.2) and linear partitioning, respectively (the sign preserved). The image has been adapted from reference [22].

and negative deviations are observed at high lingering Péclet number, showing that lingering doesn't systematically favor a specific redistribution of the erythrocytes.

3.6.4 Lingering assymetry

For insights into how the lingering behavior could modify RBC partitioning at the bifurcation, we further examined its symmetry between the two daughter branches. Due to cell collisions at the apex, it was not possible to precisely determine the proportion of lingering cells entering each daughter merely by analyzing their trajectories. Therefore, we calculated the average advection time t_a of the cells between the (blue) mask in bifurcation and the (magenta) mask in the daughter Fig. 3.9(a). This advection time was determined by calculating the convolution of the temporal Ht in the daughter mask and that in the bifurcation mask (see Fig. 3.9(b)). We then checked if there was a lingering event at the bifurcation (also monitored in a thin mask) at a time t_a earlier for each cell detection.

We realized that for such sorting, some lingering events at the bifurcation could not be attributed to any advected cell into the daughters. Indeed, the advection time of each cell can vary slightly, depending on its interactions with other cells near the apex. Therefore,

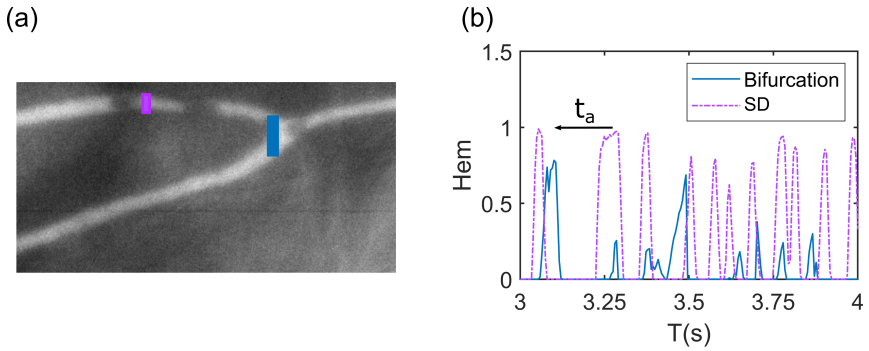

Figure 3.9: Extraction of the advection time t_a. (a) Example of mask set used to determine the advection time t_a of RBCs from the bifurcation (blue mask) to the secondary daughter (SD branch, magenta mask). Equivalent analysis is performed independently for the MD branch.Thin masks used to detect RBCs along time in the bifurcation and one daughter vessel. (b) The Ht in the masks, extracted from the binarized pictures, is measured along time. The average advection time t_a of the cells in the daughter is obtained by convolution of the two signals. The image has been adapted from reference [22].

after being temporally translated by t_a, the cell detection can be located close to the lingering event, but not exactly within its duration. For more accurate characterization, we therefore measured the proximity time t_i between the closest lingering event and the transit time (detection time in the daughter minus t_a) for each cell (Fig. 3.10(a)). Cells with a proximity time $t_i = 0$ can then be determined as lingering. We further defined $dp_\tau = |p_{SD} - p_{MD}|$ as the difference between the proportion of lingering cells in the two daughter branches Fig. 3.10(b). Because cells with a small proximity time t_i might also have been lingering or might have interacted with another cell lingering at the apex, we used the difference between the first two points of the CDF distribution of t_i (Fig. 3.10(c-e)) as errorbars for p_{SD} and p_{MD}. As can be seen in Fig. 3.10(c-e), the proximity time t_i distribution and the proportion of cells identified as lingering are distinct for the two daughters under large Pe_λ. For the experimentally observed cases as highlighted in Fig. 3.10(b), the asymmetry in the proportion of lingering cells is weakly correlated with the lingering intensity Pe_λ.

3.6.5 Origin of lingering

In order to understand what causes the cells to linger, we identified geometrical features of the bifurcations correlating with the lingering Péclet number Pe_λ. Due to the definition of the lingering events as a significant reduction of the RBC velocity at the bifurcation, it is likely that cells linger at the stagnation point, is a specific point within the flow of a fluid where its velocity becomes zero. In our experimental images, the stagnation point of the flow field coincides with the intersection between the bifurcation wall and the flow divider surface (or stagnation streamline in 2D). The flow divider sur-

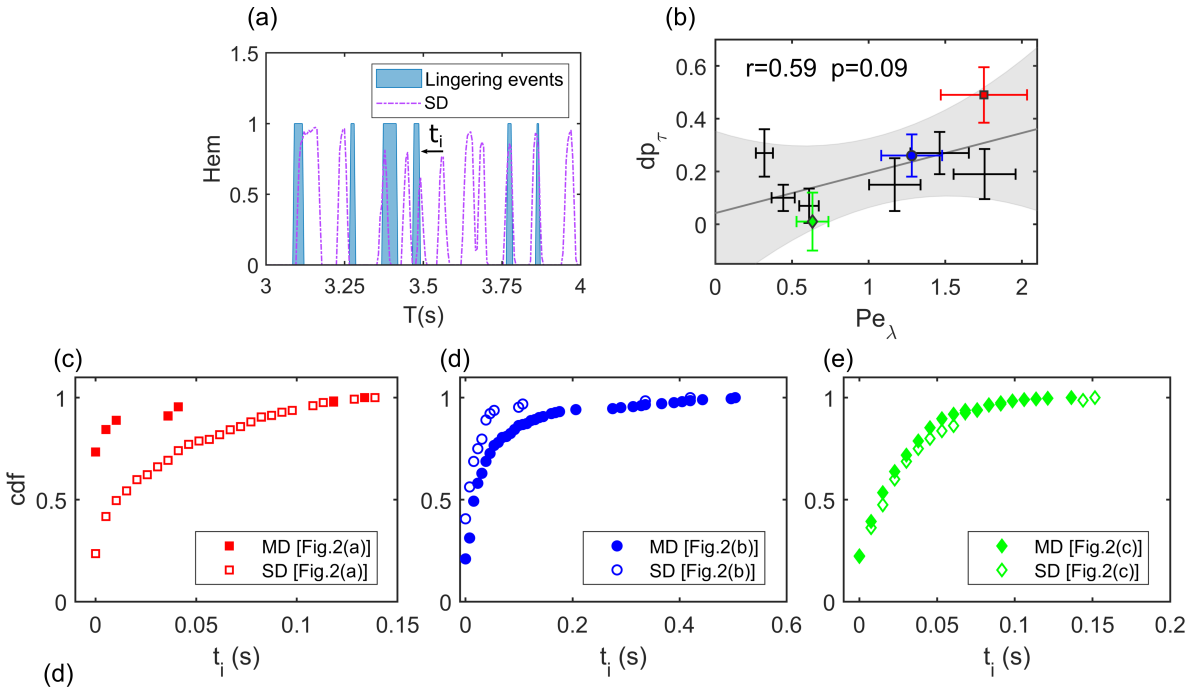

Figure 3.10: Asymmetry in RBC lingering at the bifurcation. (a) Extraction of the proximity time t_i of each cell. The Ht variation over time, extracted from the daughter's mask, is first translated by the average advection time t_a (see Fig. 3.9). Then, for each peak of this Ht along time, a proximity time t_i is obtained as the temporal distance from the closest lingering event. This process is performed independently for the two daughters. (b) The correlation between experimental dP_τ (difference in the proportion of lingering cells in SD, MD calculated from CDFs at $t_i = 0$) and Pe_λ. The Pearson-r correlation coefficient is 0.59 ($p = 0.09$). (c-e) Cumulative Density Function (CDF) of the proximity time to lingering events for both daughters of the three characteristic bifurcations. When a significant difference (considerable dP_τ) is observed in the experiments, higher proportion of lingering cells (and a closer proximity with lingering events) is usually obtained in the daughter branch with the lower fractional RBC flux FQ_e. The image has been adapted from reference [22].

face is defined as the surface separating the streamlines going into each daughter vessel. As demonstrated by previous studies, in blood vessels the flow divider surface can be approximated as a plane [111]. The distance between the apex of the bifurcation and this plane, L_s, is a function of the flow rate and the flow velocity profile [23]. Since the diameter of the mother branch is smaller than the diameter of the RBC in our case, we assumed a plug-flow profile for the velocity, i.e. a velocity distribution mostly flat in the mother vessel. Under these assumptions, the flow divider plane only relies on the fractional flow rate of daughter branches [111].

$$\frac{\mathrm{FQ_{b(MD)}}}{\mathrm{FQ_{b(SD)}}} = \frac{A_{MD}}{A_{SD}}, \tag{3.4}$$

where A_{MD} and A_{SD} are the area of the opposite sides to the flow divider plane in the mother vessel leading to both branches (see Fig. 3.11(a), where the areas are depicted with red and blue stripes, respectively). Those can be obtained as half the area of the mother vessel plus (for A_{MD}) or minus (for A_{SD}) the area between the flow divider plane and the center plane of the vessel. If assuming a cylindrical vessel, A_{MD} and A_{SD} can be calculated as

$$\begin{aligned}
\mathrm{A_{MD}} &= \frac{\pi R_M^2}{2} + 2\int_0^{L_s} \sqrt{R_M^2 - x^2}\, dx = \frac{\pi R_M^2}{2}\left(1 + \frac{2}{\pi}\arcsin\left(\frac{L_s}{R_M}\right) + \frac{2L_s}{\pi R_M^2}\sqrt{R_M^2 - {L_s}^2}\right), \\
\mathrm{A_{SD}} &= \frac{\pi R_M^2}{2} - 2\int_0^{L_s} \sqrt{R_M^2 - x^2}\, dx = \frac{\pi R_M^2}{2}\left(1 - \frac{2}{\pi}\arcsin\left(\frac{L_s}{R_M}\right) - \frac{2L_s}{\pi R_M^2}\sqrt{R_M^2 - {L_s}^2}\right).
\end{aligned} \tag{3.5}$$

based on the Eq.3.4 and Eq.3.5 the position of the stagnation point can be obtained with the following equation:

$$\frac{\mathrm{Q_{MD}}}{\mathrm{Q_{SD}}} = \frac{1 + \frac{2}{\pi}\arcsin\left(\frac{L_s}{R_M}\right) + \frac{2L_s}{\pi R_M^2}\sqrt{R_M^2 - L_s^2}}{1 - \frac{2}{\pi}\arcsin\left(\frac{L_s}{R_M}\right) - \frac{2L_s}{\pi R_M^2}\sqrt{R_M^2 - L_s^2}}, \tag{3.6}$$

where R_M is the radius of the mother branch.

Since the cells at the stagnation point experience the smallest drag force, one can assume that the dominating forces on the cells arise from their interaction with the endothelial layer. In turn, this interaction probably depends on the geometry of the wall at this location, which can mostly be described through its curvature. To determine the curvature of each bifurcation, a circle was fit on the neighborhood of the stagnation point. The curvature is defined as the inverse of the radius of this circle. In order to estimate the measurement uncertainty, we used multiple fit circles, each calculated using a different length of the neighborhood (lengths between 4 μm and 8 μm, centered around the stagnation point). The mean value of the curvatures is taken as the best approximation, while the standard deviation gives the error bars. The results showed the curvature of the bifurcation at the stagnation point correlates with Pe_λ ($r = 0.59$ and $p =$

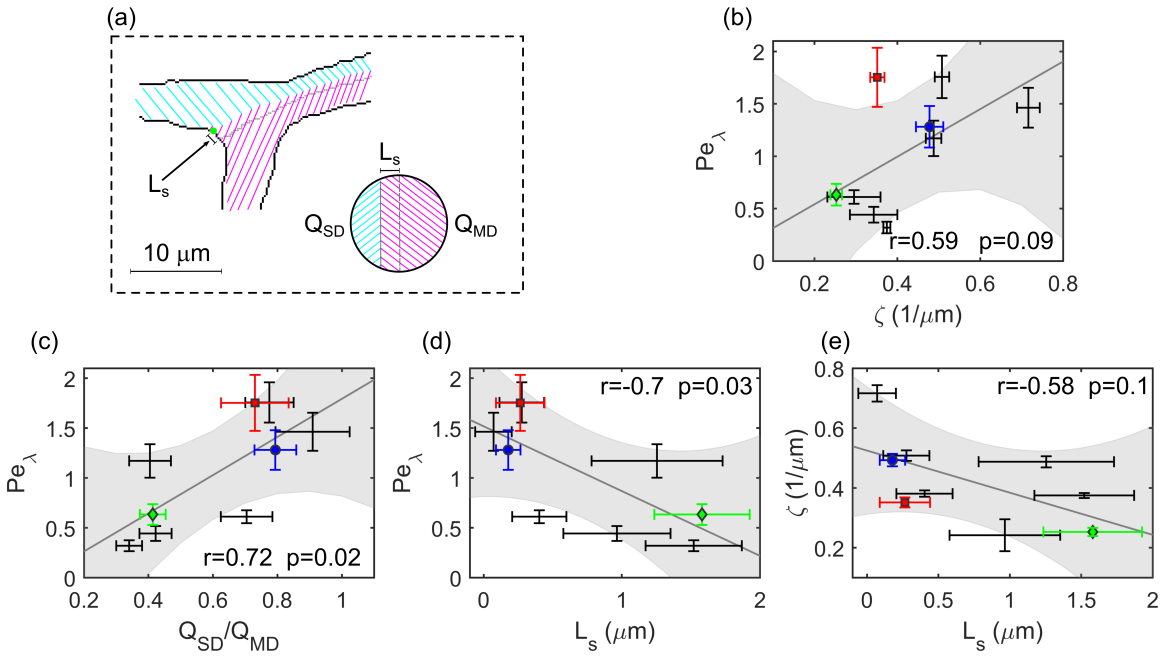

Figure 3.11: Potential origin of RBC lingering. (a) Schematic highlighting the flow split and the stagnation point at bifurcations. Flow in the mother branch splits into flows Q_{MD} and Q_{SD} in the MD and SD branches, respectively. The stagnation point is indicated by the green point, whose distance from the apex L_s is highlighted with the arrow and scale symbol. The filled circle shows an idealized cross-section of the mother vessel with simplified and flat flow separatrix. (b) Correlation of the lingering Péclet number Pe_λ with the curvature ζ of the bifurcation at the stagnation point. (c) Correlation between Pe_λ and the flow rate ratio between the secondary and main daughters Q_{SD}/Q_{MD}. (d) Correlation between Pe_λ and the distance between the stagnation point and the bifurcation apex L_S. (e) Correlation between L_S and the curvature at the stagnation point ζ. In (b-e), the points are experimental data, the solid lines show linear regression fitting of the data points, and the shaded areas indicate the 95% confidence interval prediction from each fit [22].

0.09) (see Fig. 3.11(b)). Interestingly, when testing correlations with further possibly influencing parameters, we found that the lingering Péclet number Pe_λ also correlates with the ratio of the flow rates between the secondary and main daughters Q_{SD}/Q_{MD} (Fig. 3.11(c)). Since this parameter determines the distance L_S between the apex of the bifurcation and the stagnation point through Eq. (3.6), this parameter L_S also correlates with Pe_λ (Fig. 3.11(d)). Furthermore, the bifurcations where the stagnation point is further from the apex generally have a lower curvature at the stagnation point, as shown by Fig. 3.11(e).

We therefore hypothesize that the flow rate ratio determines where the cells can linger, while the curvature of the endothelial layer at this lingering position determines the intensity of the lingering. The lingering Péclet number would then be determined by an interplay between global parameters of the bifurcation (Q_{SD}/Q_{MD}) and local geometries of the endothelial layer (the curvature at the stagnation point, ζ). When it comes to the experimental correlations, the fact that a lower p-value is found between Pe_λ and ζ than Pe_λ and Q_{SD}/Q_{MD} likely arises from the fact that the determination of ζ also relies on the approximation for L_S and then the measurement of Q_{SD}/Q_{MD}. The error propagation on these successive quantities then likely decreased artificially the correlation between Pe_λ and the successively determined parameters L_S and ζ. More geometrical parameters, which failed to demonstrate a significant correlation with Pe_λ, are included in the Fig. 3.12

3.7 Discussion

Our study demonstrates, for the first time *in vivo*, that RBC lingering (i.e. cells temporarily residing near the bifurcation apex with diminished velocity) constitutes an effective mechanism that significantly modified the partitioning of cells through capillary bifurcations. Therefore, it should be taken into account when predicting the Ht distribution in microvascular networks using simplistic mathematical models based on existing empirical laws.

Existing literature has extensively tested and validated the Zweifach-Fung effect in microvascular bifurcations at the arteriolar level, mostly through microfluidic experiments or numerical simulations. Nonetheless, studies that experimentally quantify in vivo the effect of RBC-bifurcation interactions are rare and it remains largely unknown how well the classic Pries-Secomb model describes the RBC partitioning at the excessively-confined capillary level [16, 112], where the cell-free layer (a key constituent in the empirical model of Pries et al. [10, 20, 40]) becomes negligible and the cells virtually squeeze through vessels in close contact. Previous numerical and in vitro works suggested that the branching geometry and cross-sections of the daughter branches can indeed bias the partitioning of capsules at a bifurcation, depending on the size and deformability of the capsule [113]. Considering much higher confinement reflecting capillary blood flow, our study represents the first in vivo demonstration of the microscopic effect of the bifurcation's local geometric feature, and provides a mechanistic justification through significant cell-wall interactions, namely lingering, on the partitioning of

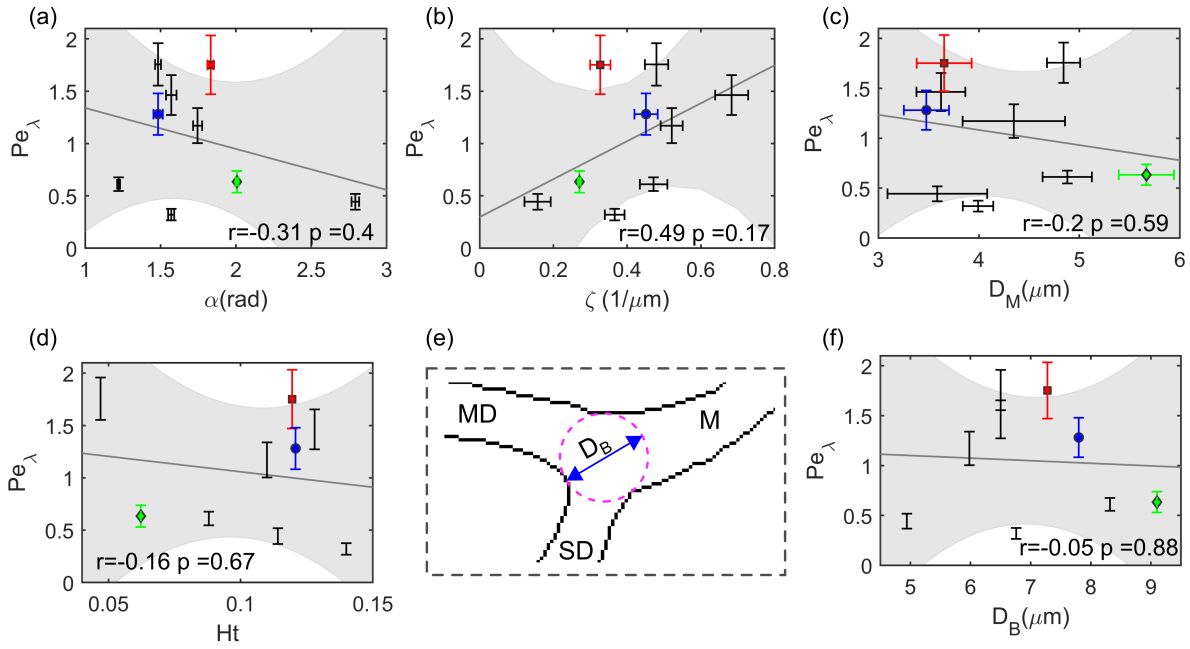

Figure 3.12: Other bifurcation properties or flow conditions showing no significant linear correlation with the lingering Péclet number. (a) opening angle formed by the two daughter vessels. (b) Curvature of the endothelium at the apex of the bifurcation. (c) Diameter of the mother vessel. (d) Ht in the mother vessel. (e) The (purple) dashed circle is fit to the bifurcation and we defined the diameter of the circle as a diameter of the bifurcation. The letters M, MD and SD refers to the Mother, Main Daughter and Secondary Daughter, respectively. (f) Diameter of the bifurcation. The image has been adapted from reference [22].

RBCs.

Furthermore, we have shown that RBC lingering is inherently associated with a certain degree of asymmetry between the daughter branches (Fig. 3.10), which can either weaken the intrinsic Zweifach-Fung effect (thus rescuing disadvantaged low-flow branches and reducing unnecessary RBC-devoid vessels in the microvasculature), or reinforce it (thus enhancing advantageous high-flow branches and exacerbating the Ht heterogeneity on the network level). Indeed, Fig. 3.8 illustrates that both positive and negative deviations from the empirically predicted partitioning by Pries et al. [40] can be observed at a high lingering Péclet number. A similar trend is observed for deviations from the linear scaling (which hypothesizes that the fractional erythrocyte flow rate equals the fractional blood flow rate $FQ_e = FQ_b$, see Fig. 3.8). The key finding is that the lingering phenomenon is a prevalent mechanism in the capillary network, subject to fine-tuning of the fractional blood flows and geometrical features of the bifurcation. We demonstrate that, under the assumption of plug flow given highly-confined cell motion, the lingering Péclet number (Pe_λ) correlates with the flow rate ratio Q_{SD}/Q_{MD} (MD and SD refer to the main daughter and secondary daughter branches, respectively). This ratio Q_{SD}/Q_{MD} determines the position of the stagnation point, where the local curvature is further associated with the lingering intensity.

Since lingering can substantially influence the RBC partitioning at capillary bifurcations (in extreme cases revert it), one can expect that lingering may play a key role in shaping the microcirculatory network, possibly contributing to the alterations of vascular networks as observed, e.g. in aneurysms and tumors. Additionally, since the deformability of RBCs affects their characteristic lingering time and, consequently, their partitioning, lingering might be a route through which the microvascular blood flow is impaired in diseases involving hardening of RBCs, such as malaria and sickle cell disease [98, 114–118]. Further in vivo investigations with rigidified RBCs should be performed in future work to test this hypothesis experimentally.

Finally, this work highlights the need for more models dedicated to RBC studies considering high confinement, as observed in microcirculatory environments entailing the lingering phenomena. Our results underline the importance of input parameters, such as the flow split at the bifurcation and the curvature of the apex region of the bifurcation.

Chapter 4

In vitro experiment

In this chapter, we present the results from an in vitro experiment conducted on a microfluidic T-junction. The main focus of our study was twofold: the lateral distribution of particles in the mother branch and the development of the CFL after the bifurcation. We investigated these aspects for both rigid and healthy cells and compared the differences between them under different Re, ranging from 6 to 24. The experimental setup included a specially designed microfluidic chip, where we carefully controlled the flow conditions to observe the behavior of particles as they passed through the T-junction. We analyzed the lateral distribution of particles and compared the characteristics between rigid and healthy cells. Additionally, we examined the development of the CFL for both cell types at different Re. The main result of this chapter have been published in reference [24].

4.1 Introduction

Blood circulation is a vital process that ensures the supply of oxygen and essential nutrients to our organs through the complex network of blood vessels in the human body. Within this complex circulatory system, the bifurcating and branching vessels play a significant role in influencing the distribution and partitioning of RBCs based on their Ht. Such bifurcating vessels can strongly affect the distribution and Ht partition of passing RBCs [3, 20]. The rigidity of RBCs can have detrimental effects on blood flow, particularly within the microcirculation. Diseases such as malaria, diabetes, sickle cell disease, and acanthocytosis are known to exhibit increased RBC rigidity and impaired deformability. This rigidity can impair the partitioning of RBCs through the microvascular bifurcation, leading to compromised blood flow dynamics. The altered mechanical properties of rigid RBCs contribute to microcirculatory dysfunction and can exacerbate the pathophysiology associated with these conditions [98, 114–118]. However, the fundamental mechanisms through which rigid RBCs modify blood flow have not been characterized extensively.

The partitioning of RBCs through vessel bifurcations is considered a non-trivial aspect of their flow in the circulatory system [37]. In recent years, numerous studies have

dedicated their efforts to investigating the factors that contribute to deviations from the well-established empirical model proposed by Pries [10, 13]. Among these factors, particular attention has been given to the influence of cell focusing and the formation of the CFL along the daughter vessels [15]. These studies aim to gain a deeper understanding of the mechanisms governing RBC distribution and flow dynamics in the microvascular network, shedding light on the complex behavior of RBCs during their journey through vessel bifurcations. The formation of a CFL is crucial for blood flow in vivo, as it reduces its hydrodynamic resistance [56, 57]. Furthermore, it is important for various biomedical applications such as plasma separation, especially in complex geometries, [59, 119–121] and highly relevant for disease diagnostics of cells with impaired deformability [2, 122, 123]. Such an impaired RBC deformability severely impacts the viscosity and the shear-thinning behavior of blood and RBC suspensions, thus affecting hemorheology, flow resistance, and microvascular perfusion [38, 124–126]. Moreover, RBC deformability can influence the emergence of a CFL or cell-depleted zones in complex microfluidic geometries that are often used in lab-on-a-chip devices [13, 67, 127].

The formation and characteristics of the CFL in microfluidic devices are influenced by several factors. These factors include the Ht (the volume fraction of RBCs in blood), the dimensions of the microfluidic channels, and the flow rate of the fluid [59,121]. Moreover, changes in the CFL in dilute suspensions can also arise from geometric features of the channel, such as confinement, [128–130] constrictions, [67, 119] and bifurcations [12, 13]. Therefore, the formation of a CFL of healthy RBC suspensions in complex geometries, such as vessel networks has received increasing attention in recent experimental and numerical investigations [13, 14, 131–134]. Although the biophysical RBC properties, such as their deformability, were found to influence the CFL as well, [67, 68] detailed knowledge about the effects of RBCs with impaired deformability on the spatiotemporal RBC organization and the partitioning in complex geometries remains scarce.

In this study, we investigate the impact of RBCs rigidity on the phenomenon of cell focusing and the subsequent formation of a CFL within a bifurcating microfluidic channel. We aim to understand how the rigidity of RBCs alters their behavior during flow, specifically in terms of their distribution and the formation of the CFL along the channel walls. Therefore, we employ a technique to artificially increase their rigidity. By treating the RBCs with glutaraldehyde, we induce a controlled rigidification, allowing us to study their behavior in a well-defined manner. We then observe and analyze the spatial distribution of these rigidified RBCs at different positions within the microfluidic T-junction. Our investigation focuses on studying the evolution of RBCs distribution across the width of the channel in addition to observing the formation of a CFL along both the mother and subsequent daughter channels. In order to gain a comprehensive understanding of the effects of RBC rigidity, we compare our findings on rigid RBCs with investigations conducted on healthy cells at equivalent RBC concentrations ($0.1 - 5\%Ht$). Our observations reveal a significant impact of RBC rigidity on the organization of RBCs at the bifurcation point following the mother channel. Specifically, we observe distinct lateral distributions of RBCs in the daughter channels, indicating a clear difference between the behavior of rigid and healthy RBCs. The altered RBC

organization highlights the influence of rigidity on the partitioning and flow dynamics of RBCs within the microfluidic system. The magnitude of this effect increases with increasing inertia. In addition, our study examines the development of the CFL within the daughter vessels of the bifurcation. By tracking the evolution of the CFL in three differents position in the daughter branch, we gain insights into how the rigidity of RBCs influences the formation and characteristics of this layer. The observed changes in the CFL provide valuable information about the flow dynamics and distribution of RBCs within the daughter vessels. Our findings contribute to a better understanding of the complex interplay between RBC rigidity and the development of the CFL, shedding light on the mechanisms underlying RBC behavior in microvascular bifurcations. Our work offers further insights into the flow behavior of RBCs with impaired deformability and how rigid cells can impair blood circulation.

4.2 Materials and Methods

4.2.1 Sample preparation

Blood is taken with informed consent from healthy voluntary donors. It is suspended in phosphate-buffered saline (PBS) solution (Gibco PBS, Fisher Scientific, Schwerte, Germany) and centrifuged at 1500 g for five minutes to separate RBCs and plasma. Sedimented RBCs are subsequently resuspended in PBS and the centrifugation and washing steps are repeated three times. For the final suspensions, Ht concentrations of $0.1\%Ht$, $1\%Ht$, and $5\%Ht$ are adjusted in a PBS solution that contains $1g\,L^{-1}$ bovine serum albumin (BSA, Sigma-Aldrich, Taufkirchen, Germany) as shown in Fig. 4.1. Furthermore, samples with artificially rigidified RBCs are prepared. For this, washed RBCs are incubated in a 0.1% glutaraldehyde (GA, grade I solution, Merck KGaA, Darmstadt, Germany) solution for one hour according to Abay et,al [135]. Subsequently, RBCs are washed with PBS to remove excess GA and are suspended in a PBS/BSA solution at the same concentrations as for healthy RBCs. Blood withdrawal, sample preparation, and experiments were performed according to the guidelines of the Declaration of Helsinki and approved by the ethics committee of the 'Ärztekammer des Saarlandes' (approval number 51/18).

4.2.2 Fabrication of master for microfluidic devices

In the production of a microfluidic chip through the application of soft lithography, a series of individual processing steps becomes imperative. The end result is a reverse pattern etched onto a silicon wafer, commonly referred to as a master mold. This master mold serves as a template, enabling the replication of identical structures using polydimethylsiloxane (PDMS).
Initiating the process with a silicon wafer, we proceed to coat it with a photoresist whose thickness is meticulously adjusted via spin-coating, as illustrated in Fig. 4.2(a, b). This light-sensitive photoresist comes in two distinct forms, each dictating its reaction

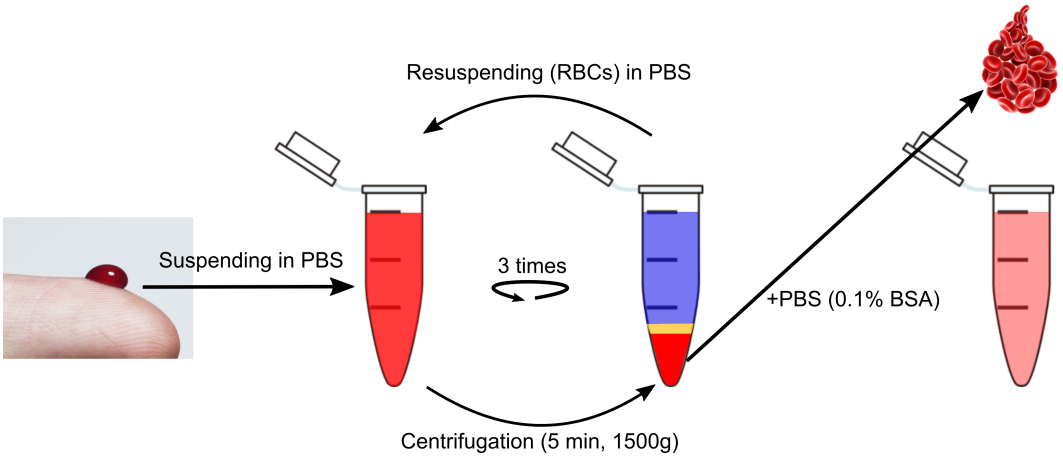

Figure 4.1: Schematic representation of the RBCs suspension preparation.

upon exposure to light radiation. For our intended purpose, the choice is the negative photoresist SU-8, signifying its solidification under UV exposure. This is in contrast to a positive photoresist, which exhibits the opposite behavior. Subsequently, a binary lithography mask, comprising a transparent film embedded with the imprinted lateral channel designs, is brought into direct contact with the photoresist. This assembly is then subjected to collimated UV light from above, as depicted in Fig. 4.2(c). To ensure stability and prevent any shifts during this process, a glass plate is securely affixed using vacuum suction. Thoroughly rinsing the illuminated silicon wafer with acetone effectively dissolves and removes the unexposed photoresist. This action leaves behind a replica of the mask on the wafer substrate, achieving the desired thickness, as illustrated in Fig. 4.2(d). The next step involves strengthening the substrate on the wafer by baking the assembly in an oven at 80°C, enhancing its mechanical robustness. The resulting relief structure on the wafer's substrate now serves as the negative mold for the microchannels, shaping the foundation for the subsequent stages of the microfluidic device fabrication.

4.2.3 PDMS

PDMS utilization is widespread due to an array of advantageous properties. PDMS is the optical transparency, chemical inertness, and non-toxicity, well-suited for observing living cells under a brightfield microscope. Additionally, PDMS excels in replica molding. With a low elastic modulus, it possesses high deformability that facilitates the release from molds [136]. PDMS can replicate complex geometric features at nanometer scale [137]. Typically supplied as a two-component siloxane liquid, PDMS consists of prepolymers, a blend of siloxanes (Si–O–Si) with methyl, vinyl, or hydro side and terminal groups. The other component is the curing agent, a shorter polymer enriched with hydro groups and a platinum catalyst. These components are mixed in a 10:1 ratio and cured at room temperature or through heat application [136]. PDMS's Young's

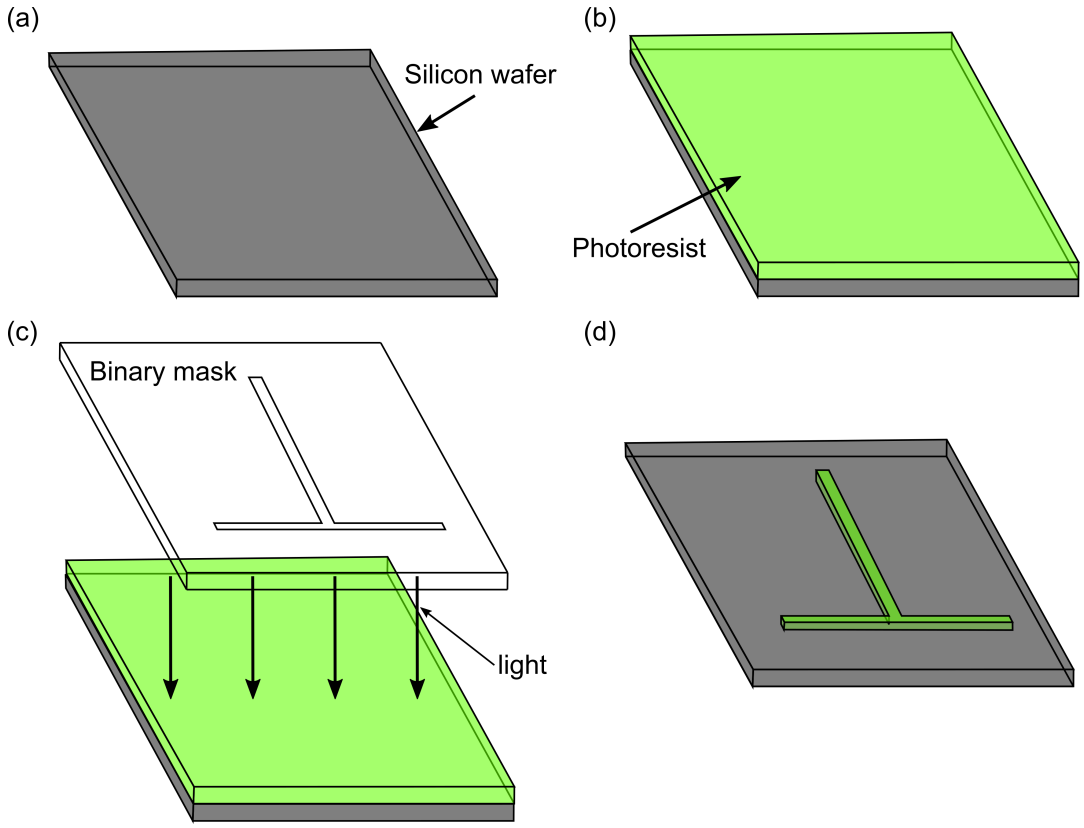

Figure 4.2: Illustration of master fabrication process. (a) A silicon wafer as the substrate upon which the fabrication process will be performed. (b) A layer of photoresist is meticulously spread onto the silicon wafer through spin coating. (c) A binary mask containing the desired geometrical patterns is positioned over the photoresist layer. Upon UV light exposure, partial polymerization of the resist occurs, leading to the formation of the intended structures. (d) Remove the sections of the photoresist that were not subjected to UV light exposure. The image has been adapted from reference [72].

modulus varies from 0.5 MPa to 4 MPa, depending on curing conditions. Simultaneously, its high Poisson ratio of 0.5 makes the polymer almost incompressible, reflecting its characteristic elasticity akin to rubber materials. Structural deformation remains within the range of approximately 10% bar. Notably, PDMS plays a pivotal role in the development of microfluidic devices, representing essential components of biological micro-electromechanical systems (MEMS), and the methodology of soft lithography is instrumental in their creation.

4.2.4 lab-on-a-chip device

he fabrication process of the microfluidic structure involved several steps. The master wafer was placed within a petri dish and coated with PDMS. Following the curing process, the PDMS layer could be detached from the master wafer. To accelerate the process of reproducing, molds were generated by embedding the master chip in epoxy resin. The epoxy resin was mixed with a curing agent and left to react at room temperature for one day. Once the epoxy mold was hardened and the master chip was removed, the mold will primed for the creation of new chips.

PDMS was poured into the epoxy mold and could be placed in a vacuum chamber to remove the air bubbles. Then, the mold, with the PDMS, was subjected to overnight curing at 70°C in an oven. After removing the mold from the oven and allowing it to cool for 30 minutes at room temperature, the resulting chip was cautiously removed to prevent damage to the mold. This chip was then cut into the desired shape. The tubing used was flexible micro medical-grade polyethylene tubing with inner and outer diameters of 0.86mm and 1.32mm, respectively. Ultimately, the chip was affixed to an optical slide using plasma bonding. To achieve this, both the chip and the slide were placed in a plamsa cleaner. With the channel structure facing upwards, the surfaces were activated during a 60-second plasma treatment conducted in a low-pressure air atmosphere. The pressure was gauged visually based on the color and intensity of the plasma glow. Following this treatment, the two surfaces were immediately brought into contact (see Fig. 4.3).

4.2.5 Microfluidic setup

In our experimental setup, we utilize a microfluidic chip featuring a T-junction geometry to study the behavior of RBCs. The RBC suspensions are carefully pumped through this custom-designed chip. The microfluidic device is fabricated using polydimethylsiloxane (PDMS, RTV 615A/B, Momentive Performance Materials, Waterford, NY) through standard soft lithography [138]. The T-channel has a height of $H = 54\mu m$ in z-direction and consists of an inlet channel, referred to as mother channel, with a width of $W_M = 104\mu m$, and a length $L_M = 3cm$ in the flow direction. At the T-bifurcation within the microfluidic chip, the mother channel divides into two daughter outlet channels. Each of these daughter channels has a width denoted as $W_D = 54\mu m$ and extends for a length of $L_D = 1.75cm$. Figure 4.4(a) shows a schematic representation of the

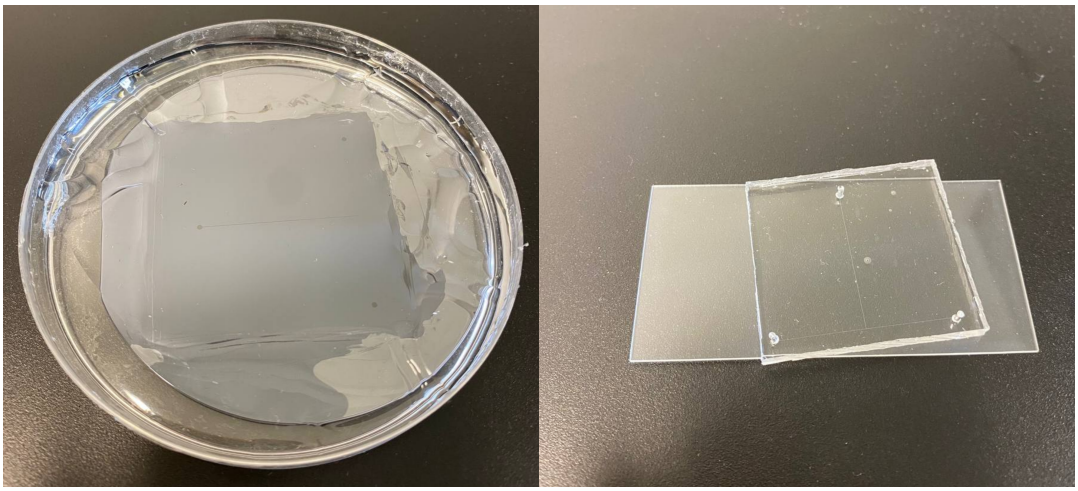

Figure 4.3: The channel structure on the silicon wafer is depicted on the left side, while the right side displays the PDMS chip affixed onto a glass slide.

microfluidic T-junction and the used coordinate systems. The mother and daughter channels are connected with rigid medical-grade polyethylene tubing ($0.86mm$ inner diameter, Scientific Commodities, Lake Havasu City, AZ) to the sample and waste containers, respectively. The microfluidic device is mounted on an inverted microscope (Eclipse TE2000-S, Nikon, Melville, New York), equipped with a LED illumination and a $40\times$ air objective (Plan Fluor, Nikon, Melville, NY) with a numerical aperture $NA = 0.6$. A high-precision pressure device (OB1-MK3, Elveflow, Paris, France) is used to pump the suspensions through the channel at constant pressure drops of $p = 200mbar$, $400mbar$, $600mbar$, and $800mbar$.

In our microfluidic experiments, we explore both symmetric and asymmetric flow rates in the daughter vessels of the T-bifurcation. In the case of symmetric flow rates, both daughter vessels have the same length denoted as L_D. To introduce an asymmetric flow rate, we modify the length of one daughter vessel while keeping the other daughter channel's length constant at L_D. Specifically, we shorten the length of one daughter channel to $L_\mathrm{D}^* = 3L_\mathrm{D}/4$, $L_\mathrm{D}/2$, or $L_\mathrm{D}/4$, as shown in Fig. 4.5. This adjustment in length results in a decreased hydraulic resistance in the shortened daughter channel, consequently leading to an increase in flow rate within that specific vessel. To quantify the degree of asymmetry, we define the asymmetry ratio as $\mathrm{AR} = L_\mathrm{D}/L_\mathrm{D}^*$. In the case of a symmetric bifurcation, the asymmetry ratio is equal to one, indicating an equal flow distribution between the daughter vessels. Microfluidic experiments are performed both with symmetric as well as asymmetric flow rates in both daughter vessels. For the symmetric case, both daughters have the same length L_D.

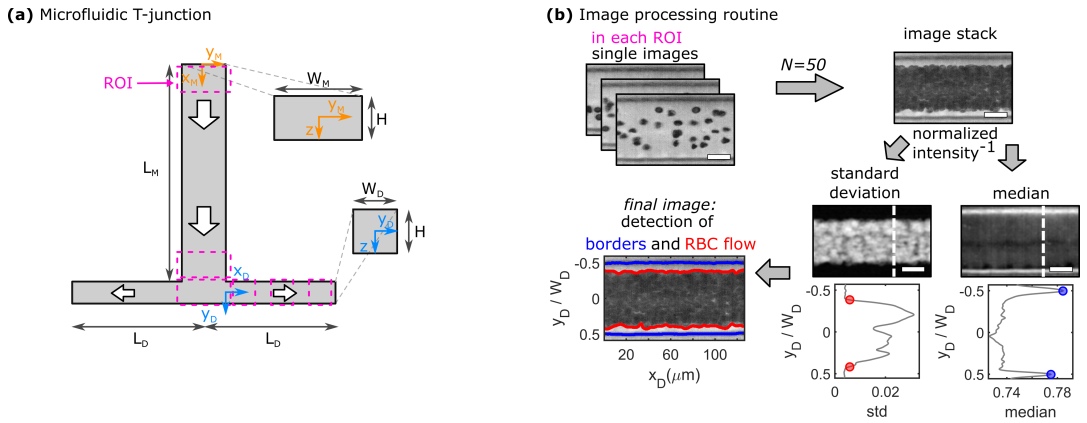

Figure 4.4: Schematic representation of the microfluidic setup and the experimental data analysis routine. (**a**) T-junction geometry, consisting of an inlet mother channel with width W_{M}, height H, and length L_{M} and two outlet daughter channels each with width W_{D}, height H, and length L_{D}. Dashed magenta boxes correspond to different regions of interest (ROI) for data acquisition in the mother and daughter vessels. (**b**) Image processing routine to determine the CFL thickness. Scale bars represent 20 μm. 50 single images are stacked and the standard deviation and median of the intensity are derived from the inverted image. Along each vertical pixel line, the intensity's standard deviation and the intensity's median are calculated. Two representative plots of the two parameters are shown below the images, corresponding to a horizontal position marked by the dashed white lines. Red dots correspond to a threshold value of 0.5% of the measured maximum inverted intensity to detect the RBC flow and blue dots highlight the peak position of the median intensity, which corresponds to the position of the walls. The red and blue lines in the final image correspond to the determined channel borders and borders of the RBC flow, respectively. The image has been adapted from reference [24].

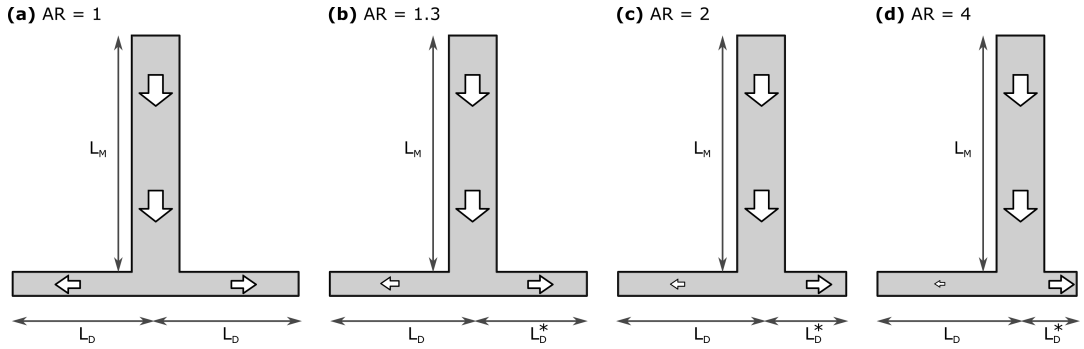

Figure 4.5: Microfluidic T-junction chips with varying asymmetry ratios. Each panel represents a different T-junction chip configuration. Panel (a) depicts the symmetric shape, where the lengths of the daughter branches are equal. Panels (b), (c), and (d) show T-junction chips with different asymmetry ratios, achieved by shortening the length of one daughter branch while keeping the other constant. The asymmetry ratio is defined as $\mathrm{AR} = L_\mathrm{D}/L_\mathrm{D}^*$, where L_D is the length of the daughter branch and L_D^* is the shortened length in the asymmetric cases. The image has been adapted from reference [24].

4.2.6 Data acquisition and analysis

In order to investigate the changes in RBC distribution across the channel width and identify the presence of the CFL, we recorded the RBC flow at various regions of interest (ROIs) along the flow direction. The magenta boxes shown in Fig. 4.4(a) highlight the specific ROIs chosen for analysis. These ROIs are strategically placed to capture important positions within the microfluidic setup. Specifically, we selected two ROIs at the beginning and end of the mother channel prior to the bifurcation, providing insights into the RBC behavior in those regions. Additionally, an ROI was positioned at the T-bifurcation to examine the partitioning of RBCs at that location. Furthermore, we placed three ROIs in the daughter channels after the bifurcation to study the RBC distribution and CFL formation in those areas. At low Ht ($\leq 1\% Ht$), a high-speed camera (MEMRECAM GX1, NAC Image Technology, Salem, MA) with a frame rate of $20 fps$ (frames per seconds) is used, which allows us to resolve the trajectories and determine the velocities of individual RBCs by means of particle-tracking velocimetry (PTV). Therefore, the positions of individual RBCs are determined in each frame and linked in consecutive frames to calculate the RBC trajectories using a self-written MATLAB (The MathWorks, Natick, MA) PTV algorithm. Based on those trajectories, the velocity profile and the RBC distribution across the channel width in y-direction are calculated.

In order to assess the impact of inertial forces, the Re Re is calculated, which relates the inertial and viscous forces in the system. The Re is defined as $\mathrm{Re} = u_\mathrm{max} D_\mathrm{h} \rho / \eta$, where $\rho = 1 g\, cm^{-3}$ represents the fluid density, the maximum cell velocity u_max in the channel center, $\eta = 1.2 mPa\, s$ is the dynamic viscosity of the fluid, and the hydraulic diameter of the rectangular microfluidic channel $D_\mathrm{h} = 2 W_\mathrm{M} H / (W_\mathrm{M} + H)$. Representative velocity profiles in the mother and daughter channels are shown in Fig. 4.6, and the

corresponding Re is depicted in Fig. 4.7, indicating values of $\mathrm{Re} = 6 - 24$, consistently greater than one. This confirms the significant contribution of inertial forces, highlighting their non-negligible influence in the microfluidic system.

At higher RBC concentrations, individual cells cannot be discriminated and the cell distribution across the channel width and the CFL cannot be determined based on the RBC trajectories. Therefore, RBC flow is recorded with a high-speed camera (Fastec HiSpec 2G, FASTEC Imaging, San Diego, CA) at a lower frame rate of $1500 fps$. A self-written MATLAB program is used to determine the channel borders, the core RBC flow, and thus, the thickness of the CFL, as exemplified in Fig. 4.4(b). First, 50 images of the recorded sequence are inverted and then stacked. Second, the pixel-wise standard deviation and median of the intensity in the stack are calculated. Regions with a high standard deviation correspond to locations in the channel where the image intensity fluctuates the most, hence the core RBC flow. The median of the intensity is most prominent at the channel borders, which do not change their position over the image sequence. Based on the peak positions of the median inverted intensity and a threshold of 0.5% of the measured maximum inverted intensity, the channel borders and the region of the RBC flow are determined, respectively. Subsequently, the thickness of the CFL is calculated for each vertical pixel line. A representative depiction of the resulting final image of the border and core RBC flow detection is shown in the bottom left of Fig. 4.4(b). Experimental CFL results are shown as mean values with corresponding standard deviations between different measurements as error bars.

4.3 Results

4.3.1 RBC focusing and distribution at low concentrations in the microfluidic T-junction

At finite inertia ($\mathrm{Re} > 1$), particles and cells in dilute suspensions can show ordering and flow focusing in straight vessels and channel [84]. In the mother channel of the microfluidic device, we observe a significant focusing phenomenon of RBCs along the flow direction. This is clearly demonstrated in Fig. 4.8, where we compare the distribution of healthy and rigid RBCs at a Ht $0.1\%Ht$ and Re ranging from 6 to 24. Each panels in Fig. 4.8 correspond to a x-position close to the end ($x_\mathrm{M} = L_\mathrm{M}$) of the mother channel. At the beginning of the mother vessel ($x_\mathrm{M} \approx 0$), cells are homogeneously distributed across the channel width for both healthy and rigid RBCs. Furthermore, RBCs flow in the close vicinity of the channel walls. However, at the end of the mother vessel ($x_\mathrm{M} = L_\mathrm{M}$), the focusing effect becomes more pronounced as the Re increases, indicating the influence of inertial forces on the RBC behavior. At Re equal to or greater than 12, we observe a distinct spatial organization of RBCs, with healthy and rigid cells exhibiting different positioning within the channel. Healthy cells are focused on three equilibrium positions, namely one in the channel center and two close to the borders. On the other hand, rigid RBCs preferentially flow in the center of the channel. Furthermore, both healthy and rigid RBCs exhibit a pronounced CFL close to the channel walls at $x_\mathrm{M} = L_\mathrm{M}$.

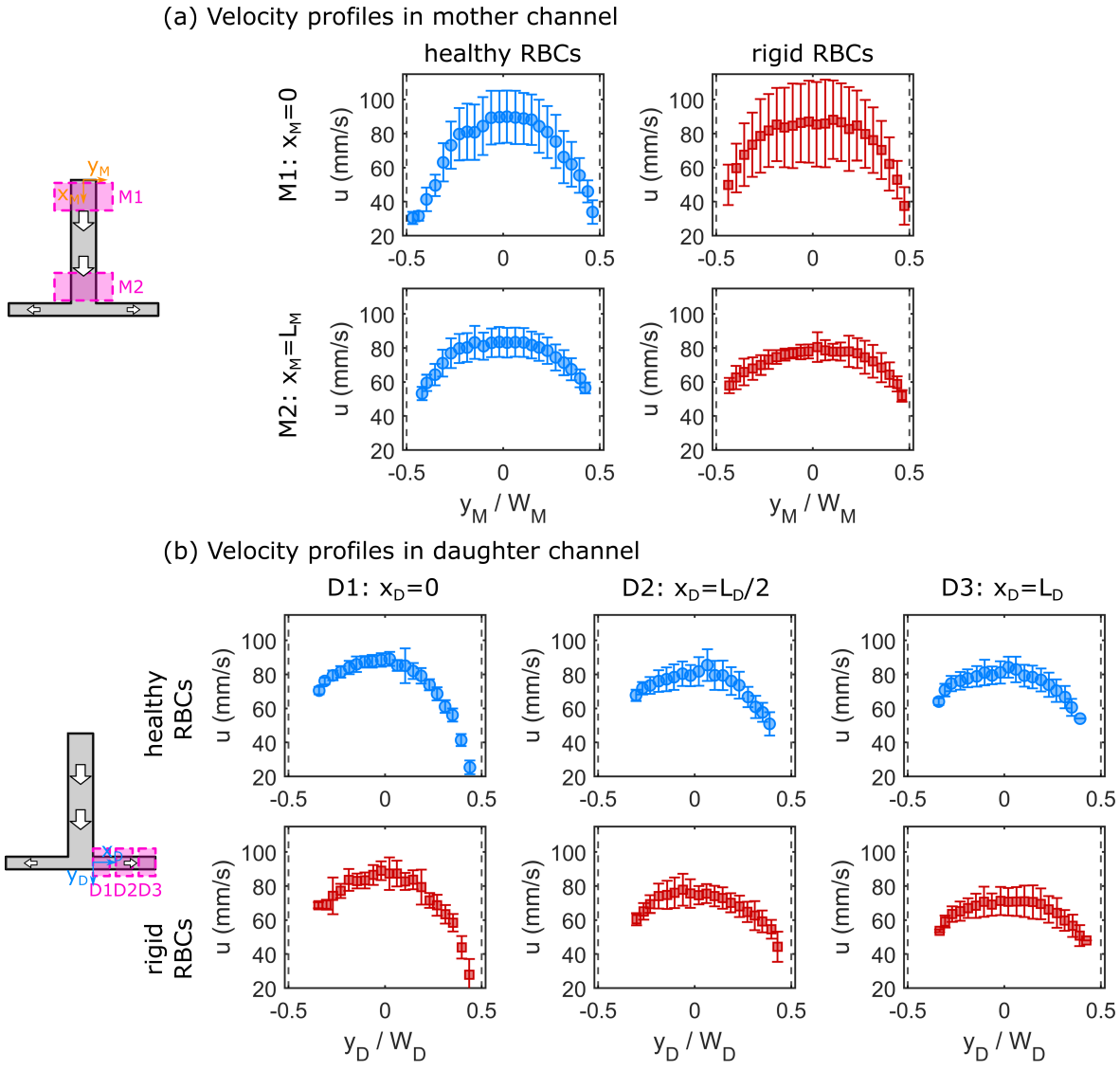

Figure 4.6: Velocity profiles at multiple positions in the T-junction. Data is representatively shown for a pressure drop of $p = 200mbar$, which results in Re = 6. (a) Velocity profiles in the mother channel for (left) healthy and (right) rigid RBCs at the (top) beginning ($x_\mathrm{M} \approx 0$) and (bottom) end ($x_\mathrm{M} = L_\mathrm{M}$) of the mother vessel. (b) Velocity profiles in the daughter channel for (top) healthy and (bottom) rigid cells at three positions along the flow direction. The image has been adapted from reference [24].

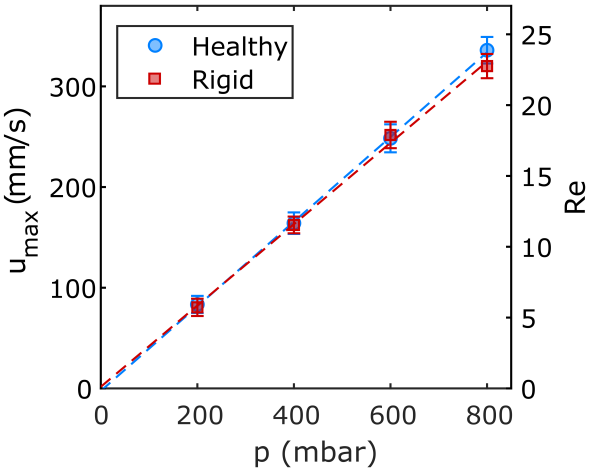

Figure 4.7: Maximum velocity $u_{\max}$ and Re as a function of the applied pressure drop p for healthy and rigid RBCs. Dashed lines correspond to linear fits of the experimental data. The image has been adapted from reference [24].

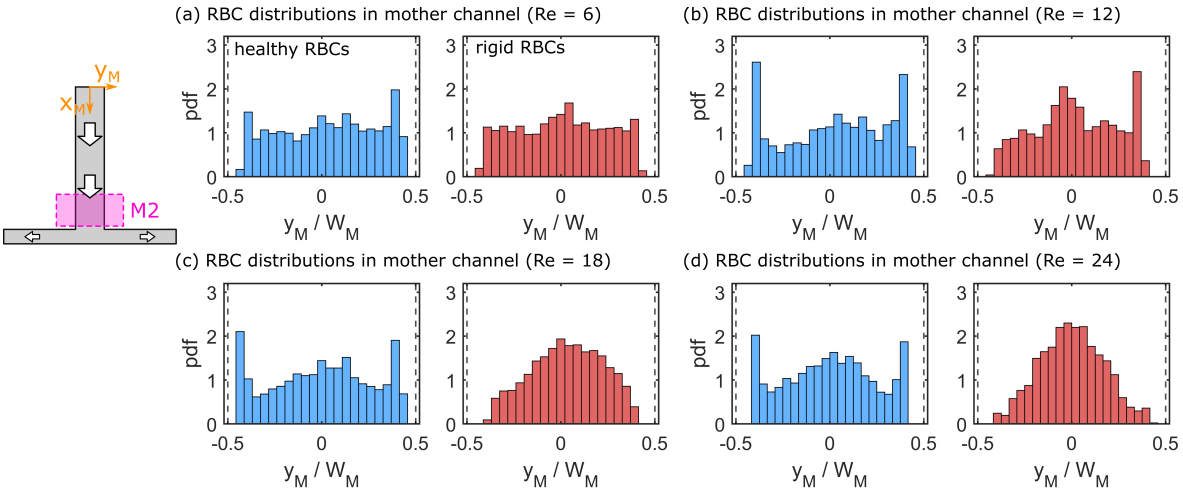

Figure 4.8: Probability density distributions (pdf) for healthy and rigid RBCs at the end of the mother channel ($x_{\mathrm{M}} = L_{\mathrm{M}}$) in a microfluidic T-junction. Panels (a) to (d) correspond to different Re of 6, 12, 18, and 24, respectively, with a Ht of $0.1\%Ht$. In each panel, the left side represents the pdf for healthy RBCs, while the right side represents the pdf for rigid RBCs. The image has been adapted from reference [24].

At the T-bifurcation, the flow of RBCs from the mother channel splits into two daughter branches. To investigate the behavior of RBCs in the daughter channels, we track their movement at three specific positions. The first position, labeled as D1, corresponds to the beginning of the daughter branches ($x_D \approx 0$). The second position, D2, is located approximately at the middle of the daughter branches ($x_D \approx L_D/2$). Lastly, the third position, D3, represents the end of the daughter branches ($x_D \approx L_D$). To simplify the analysis and description of the RBC distribution within the daughter channels, we adopt a simplified notation based on the top view projection of the T-junction. Specifically, we define positions in the daughter channels as "up" when $-0.5 \leq y_D/W_D < 0$, indicating locations towards the upper portion of the channel width. Conversely, positions are labeled as "down" when $0 \leq y_D/W_D \leq 0.5$, representing locations closer to the lower portion of the channel width. This notation helps differentiate and classify the RBC distribution in relation to the vertical axis within the daughter channels. Hence, the upper CFL in the daughter branches corresponds to the continuation of the CFL in the mother channel. Figure 4.9 depicts the distribution of RBCs across the width of the daughter channels after the symmetric bifurcation, with each panel corresponding to a specific Re. The top row of panels shows the RBC distribution for healthy cells, while the bottom row represents the distribution for rigid cells. For Re larger than 18, we observe a distinct behavior in the RBC distribution across the daughter channels. After the T-bifurcation in D1, there is a prominent accumulation of healthy RBCs at an off-centered position near the upper channel wall ($y_D/W_D \approx -0.28$). This accumulation gradually diminishes as we move away from the upper wall (y_D/W_D) towards the center of the channel. It is worth noting that the RBC flow is concentrated near the down wall ($y_D/W_D = 0.5$) in D1, while a significant upper CFL ($-0.5 \leq y_D/W_D \leq -0.3$) is formed. As the RBCs flow through the daughter vessels (D2 and D3), the peak in the RBC distribution diminishes, resulting in a more uniform distribution across the channel width for healthy cells. Additionally, a CFL appears in the region between $0.3 \leq y_D/W_D \leq 0.5$ as the RBCs flow through the daughter branches.

In contrast to healthy cells, rigid RBCs exhibit a broader off-centered peak around $y_D/W_D \approx 0.2$ immediately after the bifurcation in D1, as shown in the bottom panel of Fig. 4.9. As they flow along the daughter channel, more rigid RBCs migrate towards the upper half of the channel ($-0.5 \leq y_D/W_D \leq 0$). Notably, the peak in the distribution at $y_D/W_D \approx 0.2$ persists for rigid RBCs until the exit of the daughter vessel at D3. Furthermore, as the Re increases, these distinct focusing effects for healthy and rigid RBCs Rynolds number (become more pronounced as shown in Fig. 4.9).

The thickness of the CFL at the end of the mother vessel ($x_M = L_M$) plays a crucial role in determining the flow characteristics and hemodynamics within the microfluidic system. Figure 4.10 provides insights into the dependency of the CFL thickness on both Re and RBC concentration for both rigid and healthy cells. In Fig. 4.10(a), the CFL thickness is investigated as a function of Re at a constant RBC concentration of $0.1\%Ht$. It is observed that within the range of investigated pressure drops, the CFL thickness shows only a slight increase with increasing Re for both rigid and healthy cells. This finding suggests that changes in the flow rate or velocity alone do not significantly affect

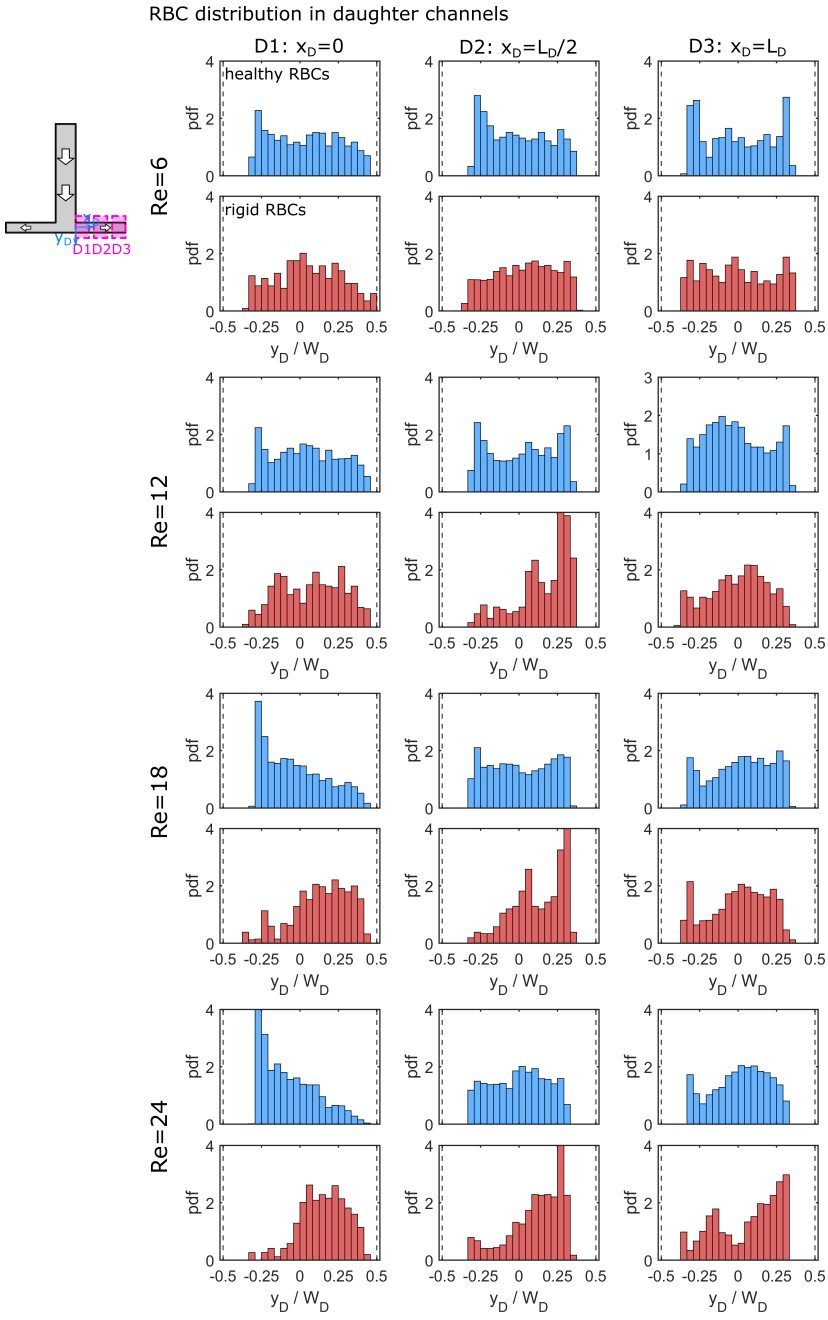

Figure 4.9: The figure presents pdf illustrating the distribution of healthy and rigid RBCs across the width of the daughter channels following the symmetric bifurcation. Each panel in the figure corresponds to a specific Re, with a Ht of 0.1%Ht. The top row of panels represents the RBC distribution for healthy cells, while the bottom row is for rigid cells. Panels correspond to Re values of 6, 12, 18, and 24, respectively. Within each panel, three different positions along the daughter branches are depicted. The image has been adapted from reference [24].

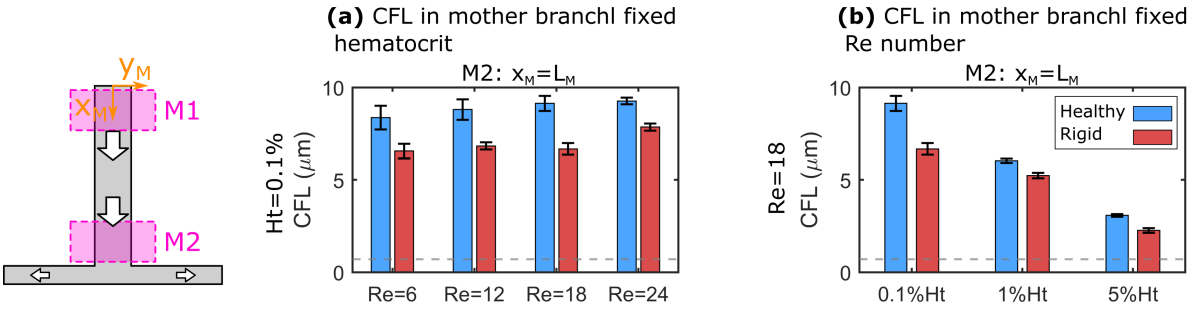

Figure 4.10: (a) CFL at the end of the mother channel as a function of Re at 0.1%Ht. (b) CFL at the end of the mother channel as a function of the RBC concentration at Re = 18. Horizontal lines correspond to the optical resolution limit of two pixels. The image has been adapted from reference [24].

the CFL thickness in this range. On the other hand, Fig. 4.10(b) explores the CFL thickness as a function of RBC concentration at a constant Re of 18. Interestingly, a strong decrease in the CFL thickness is observed with increasing RBC concentration. Moreover, a notable difference is observed between rigid and healthy RBCs in terms of CFL formation. Rigid RBCs tend to form a smaller CFL compared to healthy RBCs, particularly at low RBC concentrations. This observation is consistent with previous studies [59]. This difference is most pronounced at low RBC concentrations.

We further examine how an asymmetric bifurcating flow affects the RBC partitioning and the CFLs at the bifurcation. Figure 4.11(a) shows representative image stacks for the bifurcating flow of a 0.1%Ht healthy RBC suspension at different asymmetry ratios AR. This asymmetry leads to different flow rates as well as to different CFLs in both daughter vessels. To assess the relative RBC partitioning and flux, individual RBCs are tracked at the T-junction, representatively shown for 90 trajectories at AR = 4 in Fig. 4.11(a). The two colors represent trajectories that end in either the left or the right daughter channel. The fraction of RBCs that end in the shorter daughter vessel n^* with respect to the total number of RBCs that enter the bifurcation n_0 is plotted as a function of the asymmetry ratio for healthy and rigid cells in the top panel of Fig. 4.11(b). In the case of a symmetric bifurcation (AR = 1), we find $n^*/n_0 = 0.5$. However, with increasing AR > 1, the number of RBCs that flow into the short daughter channel increases. This increase seems to be more pronounced for rigid than for healthy RBCs. Moreover, as visible from the snapshots in Fig. 4.11(a), two distinct CFLs emerge close to the two channel borders in each daughter vessel. In Fig. 4.9, we observe that the down CFL at the impacting wall is essentially zero, while the upper CFL closer to the mother channel is more pronounced. The ratio between the two upper CFLs of the short and long daughter CFL*/CFL is shown in the bottom panel of Fig. 4.11(b). Here, we find that with increasing AR the CFL*/CFL ratio decreases.

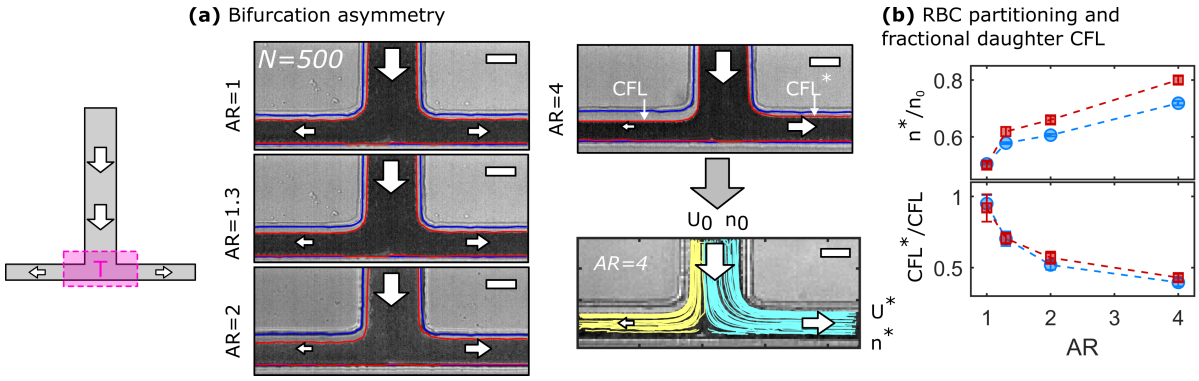

Figure 4.11: (a) Stacks of 500 images showing RBC partitioning at the bifurcation for different asymmetry ratios AR. The red and blue lines in the image stack correspond to the channel borders and the RBC flow, respectively. For AR = 4, representative trajectories are shown. Scale bars represent $50\mu m$. (b) Relative RBC flux in the shorter daughter vessel n^*/n_0 (top) and the ratio of the upper CFL between the short and the long daughter $\mathrm{CFL}^*/\mathrm{CFL}$ as a function of AR. The image has been adapted from reference [24].

4.3.2 CFL development in symmetric daughter vessels

To analyze the development of the CFL in the daughter vessels after the bifurcation, a dedicated image processing routine, as depicted in Fig. 4.4(b), is employed. This routine involves stacking 50 images at each region of interest (ROI) and determining the positions of the RBC core flow and the channel borders. The resulting data provides valuable insights into the CFL formation and its evolution along the daughter vessels. Fig. 4.12 presents representative images at three different positions along the daughter vessels, allowing us to observe the progression of the CFL. The labels "up" and "down" correspond to the CFL in the negative and positive y_D-directions, respectively, as determined by the histogram-based analysis shown in Fig. 4.9. These images provide visual evidence of how the CFL develops and varies along the daughter vessels, shedding light on the flow behavior and the spatial distribution of RBCs in these regions.

Figure 4.12(b) shows the development of the asymmetric up and down CFLs along the flow direction in the daughter for different Re. At Re = 6, the upper CFL is constant in the first two regions and slightly decreases at the end of the daughter vessel. Rigid RBCs show similar behavior as healthy RBCs at Re = 6. However, they generate a smaller CFL compared to healthy cells. At $x_\mathrm{D} = 0$, the down CFL is essentially zero, since cells that flow in the center of the mother channel are pushed against the wall in the stagnation area of the bifurcation. As the cells travel along the daughter, the down CFL consistently builds up for both rigid and healthy RBCs. Similar to the upper CFL, the down CFL for healthy cells is larger than for rigid cells at the end of the daughter channel. However, for Re=6, the thickness of the down CFL does not seem to have reached the thickness of its upper counterpart, thus forming an asymmetric CFL at the end of the daughter branch at $x_\mathrm{D} = L_\mathrm{D}$.

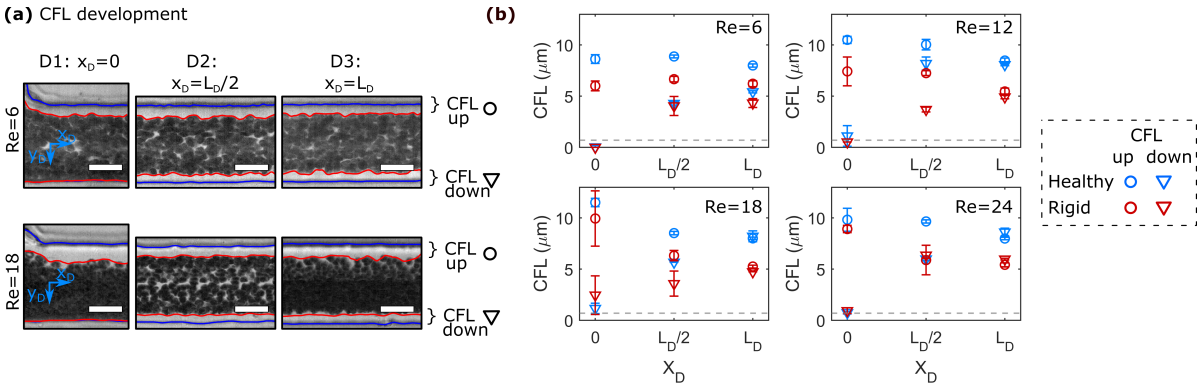

Figure 4.12: CFL development along the flow direction in the daughter vessels. (a) Representative superimposed images for a 0.1%Ht RBC suspension at three positions in the daughter channel at Re = 18 for (top) rigid and (bottom) healthy RBCs. The red and blue lines in the images correspond to the channel borders and the RBC flow, respectively. Scale bars represent 20μm. Up and down CFL correspond to the CFL in negative and positive y_D-direction, respectively. (b) Up and down CFL for a 0.1%Ht RBC suspension as a function of x_D for different Re. The image has been adapted from reference [24].

Increasing Re affects the CFL development in the daughter vessel as follows:

(i) At the beginning of the daughter vessel at $x_D = 0$, increasing Re leads to an increase in the upper CFL for both healthy and rigid RBCs. Due to the increased inertia, RBCs that initially flow in a central position of the mother channel are pushed into the T-junction wall opposite the mother channel. Therefore, the down CFL is still zero. Moreover, RBCs that flow at streamlines close to the channel walls in the mother channel are pushed away from the wall to positions closer to the center of the daughter channel, thus forming a larger CFL directly after entering the daughter branch at $x_D = 0$, reminiscent of cell-depleted zones generated by lip vortices in other complex flow fields of RBC suspensions [34].

(ii) In the second region of interest at $x_D = L_D/2$, the thickness of the upper CFL decreases for Re > 12 compared to the upper CFL at the entrance of the daughter vessel. Opposite to this trend, the down CFL increases.

(iii) At the end of the daughter vessel at $x_D = L_D$, experiments at Re ≥ 12 result in the formation of an equal thickness in the up and down CFL. This symmetric CFL at $x_D = L_D$ is independent of Re within the investigated regime.

4.4 Discussion

Flowing through the inlet mother channel, RBCs are focused to specific positions along the channel width for healthy and rigid RBCs, as shown in Fig. 4.8(a). For healthy RBCs, the emergence of two pronounced peaks close to the walls of the channel at the

end of the mother channels is in contrast to the idea of an RBC core flow near the channel center, accompanied by a CFL near the channel walls [3,39]. Non-uniform RBC distributions in straight channels have previously been reported Zhou [139]. observed so-called off-center two-peak profiles for healthy RBCs in straight channels with dimensions on the same order of magnitude as the mother channel in this study. The authors argue that the emergence of these off-center two-peak profiles is co-determined by the spatial decay of hydrodynamic lift and the global deficiency of RBC dispersion in dilute suspensions [139]. The positions of the peaks move towards the channel centerline along the flow direction until they stabilized around $y/W \approx \pm 0.4$, similar to the peak positions observed in Fig. 4.8 at the end of the mother channel. However, in their study, these peculiar RBC distributions emerged at negligible inertia ($\mathrm{Re} < 2 \times 10^{-4}$). [139] For dilute suspensions with Hts $< 1\%$ shown in Fig. 4.8 at $\mathrm{Re} > 1$, focusing effects can severely impact the spatiotemporal distribution of particles and cells in tubes and microchannels.

In general, lateral migration and focusing of particles in circular pipes due to inertial lift forces was first reported by Segré and Silberberg [81]. Inertial focusing is mainly driven by two dominating opposing forces. On one hand, the wall-induced lift force, due to the interaction between the particle and the channel wall, pushes the particle away from the wall. On the other hand, the shear gradient-induced lift force, due to the curvature of the velocity profile in the channel, directs the particle away from the channel center [68,84]. These forces drive particles and cells towards specific equilibrium positions in the channel cross-section, which depend on the channel geometry, particle size and rigidity, and flow velocity. In square or rectangular microchannels, focusing of particles or cells is achieved for particle $\mathrm{Re_p}$ of the order of equal or larger than one, where $\mathrm{Re_p} = \mathrm{Re}(a/D_\mathrm{h})^2$ with the particle or cell size a. Further, a certain length L_f is required for particles to reach stable equilibrium positions along the flow direction [68]. For rectangular channels, different stable focusing positions located near the faces of the channel exist. Depending on the aspect ratio of the channel cross-section, the distance from the inlet, and Re, particles and cells can be focused towards the wide channel faces or both the short and wide faces [140–146]. For the experiments shown in Fig. 4.8, and with the RBC diameter $a = 8\ \mu m$, we find $\mathrm{Re_p} \approx 0.24$, $L_\mathrm{f} \approx 1\ mm$, and $\mathrm{Re} = 24$. Although the $\mathrm{Re_p}$ is smaller than one, we expect inertial lift forces to partially affect RBC ordering and influence the observed distributions of healthy RBCs at $\mathrm{Re} > 1$. The lift force acting on the RBCs and hence, the focusing and separation of cells, further depend on their shape [125, 147–149]. In our study, the RBCs are rigidified in stasis where the cells exhibit a biconcave disk-like shape. While the healthy RBCs are able to adapt their shape according to the flow conditions in the channel, rigid RBCs retain their shape fixed in stasis. Hence, the difference in the distribution of rigid RBCs shown in Fig. 4.8, emerges as a consequence of their impaired deformability, which results in different shapes in flow, in agreement with studies on particles and ellipsoids [147] and rigid RBCs [148]. Furthermore, Shen [13] investigated the effect of RBC deformability on the inversion of Ht partition at microfluidic bifurcations. At low RBC concentrations, they observed an inversion of the Ht profiles that we observe for healthy and rigid cells. However, instead of using GA to irreversibly fix the RBC shape, the authors used

different dextran concentrations to tune the viscosity contrast between the inner cytosol and surrounding fluid. This changes the dynamics of lift and hydrodynamic interactions of cells, as well as their transient shape dynamics [150], and might therefore lead to contradictory behavior with respect to the results reported in Fig. 4.8.

At the bifurcation at the end of the mother channel, we observe RBC partitioning, which is affected by the asymmetry ratio of the T-channel, as shown in Fig. 4.11, as well as distinct distributions for healthy and rigid RBC, shown in Fig. 4.8. Early theoretical model predictions [111] and experiments [11] on microvascular bifurcations revealed a nonlinear relation between the fractional RBC flux and the fractional bulk flow rate at $\mathrm{Re} \ll 1$. The classical Zweifach-Fung effect states that the daughter vessel with the highest flow rate will collect a higher Ht. [37]. One simple rationalization is that the RBCs focus on the streamlines with a higher flow rate, while the CFL is formed and contains the streamlines with lower flow rates. The daughter vessel with the highest flow rate then collects blood enriched in RBCs, while the other collects a bigger proportion of blood depleted from RBCs. The focusing and characteristics of the CFL are important parameters influencing the partitioning of RBCs at bifurcations. Recent studies highlighted that the asymmetry of cell focusing observed after a bifurcation can significantly modify the partitioning of RBCs in subsequent bifurcations [13, 15, 134, 151]. Additionally, it has been shown that at low Ht, RBC flow tends to deviate from the Zweifach-Fung effect and that deformability plays an important role in this reverse behavior of partitioning [13].

Additionally to our results on the RBC focusing phenomenon, we provide further insight into the CFL formation along the mother and daughter channels and their dependency on the applied pressure drop, Ht, and cell rigidity, as highlighted in Fig. 4.10 and Fig. 4.12. The formation of a CFL is attributed to the tendency of RBCs to laterally migrate away from the vessel wall. The main driving forces for this migration include size exclusion effects due to the finite size of the RBC, boundary interactions, and macromolecular layer exclusion effects due to the inner lining of the vessel, and the curvature of the velocity profile in the vessel that produces a tendency for migration toward the vessel centerline [3,20,59,152]. As shown in Fig. 4.8 and Fig. 4.12, we do not observe a CFL at the beginning of the mother channel and similarly, at the beginning of the daughter vessel for the down CFL.

For straight microfluidic channels, the CFL growth along the flow direction was investigated before. Zhou [139] recently investigated the CFL growth in a straight rectangular channel comparable to the dimensions of the mother channel used in this study, however, at negligible inertia $\mathrm{Re} \ll 1$ using numerical simulations and microfluidic experiments. At low RBC concentrations, they observed a build-up of the CFL that followed a power-law behavior with exponents between 0.26 and 0.4. The CFL in their simulations increased over a length of $28 \times L/D_\mathrm{h}$ without saturation. In their microfluidic experiments, the CFL growth occurred over more than $46 D_\mathrm{h}$ without reaching an equilibrium for RBC concentrations of 1%. In our study at $\mathrm{Re} > 1$, the RBC travel over roughly $350 \times L/D_\mathrm{h}$ at the end of the daughter vessel showing both saturation and recovery of symmetry. Based on the evolution of the lower CFL in the daughter vessel in

the experiments, shown in Fig. 4.12, we consider the CFL to have reached a steady state at $x_{\mathrm{D}} = L_{\mathrm{D}}/2$ ($\approx 175 D_{\mathrm{h}}$) for $0.1\%Ht$. Our numerical simulations further show that the length to reach the steady-state CFL is not significantly influenced by Re. However, the simulations also demonstrate that healthy RBCs achieve their equilibrium CFL under flow faster than rigid cells. For higher RBC concentrations in the experiments, the CFL saturates even faster. This is due to enhanced RBC interactions and collisions in the RBC core flow that increase with the Ht and that push the cells toward the channel walls.

Besides this dependency of the CFL growth on the RBC concentration, the magnitude of the CFL decreases with increasing Ht. Additionally, we find that the CFL thickness is always smaller for rigid RBCs compared to healthy RBCs under the same experimental conditions (Re and Ht) and at the same position (x_{D} or x_{M}), in agreement with previous studies [67, 127, 132, 133]. In bifurcating microfluidic channels, the partitioning and flow of RBC suspensions and the emergent CFL revealed heterogeneous RBC distributions, skewed and blunt velocity profiles, and an enhancement of the thickness of the CFL at higher Ht [12, 19, 131, 153–155]. Yamamoto [14] studied the partitioning of RBCs through asymmetric bifurcating microchannels at $0.5\%Ht$. They observed that with an increasing fractional flow rate in the daughter vessels, the CFL ratio between the mother and the daughter vessel decreases, similar to our results shown in Fig. 4.11(a). While other numerical studies already showed that rigidification of RBCs tends to decrease the CFL width [156, 157], those previous studies do not provide a comparison with experimental data as our study does. This is particularly relevant since most of the combined studies showed some discrepancies between simulations and experiments [2, 139].

Understanding the distribution profile and CFL development in bifurcation channels is paramount to understanding the flow and RBC in vascular networks. In such network structures, which often consist of multiple series-connected bifurcations, the CFL in successive bifurcations is crucially impacted by the RBC distribution in the previous bifurcation [18, 132, 133, 158]. Zhou [134] found that changing the fractional flow rate between the daughter vessels leads to a complete depletion of RBCs in one branch of the successive bifurcation. Similarly, the distinct RBC distributions of healthy and rigid RBCs in the different ROIs in the daughter vessels (see Fig. 4.9) would lead to dramatically different RBC organizations in subsequent branching channels. Namely, the formation of a pronounced peak of rigid cell concentration close to the lower daughter walls is a potential mechanism through which rigid cells can perturb the healthy flow of RBCs in the circulatory network.

4.5 Conclusions

Studying the effect of RBC rigidity in microfluidic flows advances our knowledge of blood flow in vivo and is crucial to understand the impact of pathological RBC changes on their flow properties, especially in complex geometries, such as bifurcating vessels and networks. In this study, we performed microfluidic measurements at various positions along

the channel flow direction in a bifurcating microchannel to understand the RBC flow behavior, their lateral organization across the channel width, and the CFL phenomenon covering a broad Ht and Re range of $0.1 - 5\%Ht$ and $\mathrm{Re} = 6 - 24$, respectively.

In the mother channel, we observe different RBC focusing patterns that result in the emergence of two peaks close to the channel walls for healthy cells, while rigid RBCs predominantly flow along the channel centerline. Arriving at the bifurcation, these differences lead to distinct RBC distributions in the daughter vessels for rigid and healthy RBCs, which persist until the end of the channel. Our microfluidic in vitro experiments on artificially hardened RBC with GA show that the partition at the level of the bifurcation depends strongly on RBC deformability. Further, we reveal how the bifurcation affects the development of the different CFLs in the daughter branches. Our numerical simulations further demonstrate that the length to reach the steady-state CFL depends on cell rigidity. Since the distribution of RBCs after a bifurcation has been shown to be a determining factor for the distribution of RBCs in the microcirculatory network [134], the higher concentration close to the lower daughter walls demonstrated by our study for rigid cells is a potential mechanism through which blood flow can be modified by pathologically stiffened cells. Our findings highlight the importance of understanding the influence of RBC rigidity on partitioning in complex flow fields, and thus oxygen delivery in the microcirculatory network.

Chapter 5

Conclusion and outlook

In conclusion, our thesis comprises two pivotal research streams, each offering a unique perspective on the significance of partitioning of RBCs in microcapillary bifurcations. Chapter 3 delved into our in vivo investigations using the golden hamster, elucidating the profound effects of 'lingering' behavior on the partitioning of RBCs at microcapillary bifurcations. Moving forward to Chapter 4, we shifted our focus to in vitro experiments, specifically scrutinizing the deformability index of RBCs and its influence on the development of capillary flow patterns at a T-bifurcation, as well as the lateral distribution of RBCs. These two complementary lines of inquiry collectively enhance our understanding of the complex relationship between RBC deformability and microcapillary hemodynamics. By bridging the gap between in vivo and in vitro data, our research contributes valuable insights that have the potential to inform advancements in the field of medical science.

In the first part for the in vivo experiment, our research represents a groundbreaking advancement in our understanding of RBCs behavior within microvascular networks, particularly at capillary bifurcations. We have discovered a phenomenon we call "RBC lingering," where RBCs temporarily residing near the apex of bifurcations, slowing down their velocity. This lingering effect significantly alters how RBCs are distributed through these bifurcations. As a result, when creating mathematical models to predict Ht distribution in microvascular networks, we must now account for this phenomenon, rather than relying solely on existing empirical laws. Previous studies have extensively investigated the Zweifach-Fung effect in microvascular bifurcations, mainly at the arteriolar level, primarily using microfluidic experiments or numerical simulations. However, there has been a rarity of experimental studies that quantitatively measure the in vivo impact of RBC-bifurcation interactions. Moreover, the classic Pries-Secomb model, which is widely used to describe RBC partitioning, has not been thoroughly validated for the highly confined capillary level, where the CFL, a crucial element in the empirical model of Pries et al., becomes negligible. Our research bridges this gap by demonstrating the microscopic effects of local geometric features at bifurcations, emphasizing intense cell-wall interactions, specifically RBC lingering, on RBC partitioning.
Additionally, we have established that RBC lingering is inherently linked to a degree

of asymmetry between the daughter branches, which can either weaken or reinforce the Zweifach-Fung effect. This means that RBC lingering can either benefit low-flow branches or enhance high-flow branches, ultimately affecting Ht distribution in the microvasculature. Our findings indicate that the extent of RBC lingering, quantified by the Péclet number, correlates with the flow rate ratio $\left(\frac{Q_{SD}}{Q_{MD}}\right)$, the stagnation point's position and local curvature.
Importantly, our research has significant implications for understanding how the microvascular network remodels during development or in disease states. RBC distribution plays a critical role in vascular remodeling, influencing wall shear stress differences in neighboring branches. Given that lingering can substantially influence RBC partitioning at capillary bifurcations, it may contribute to observed alterations in vascular networks, such as those seen in aneurysms and tumors. Furthermore, in diseases involving RBC hardening, like malaria and sickle-cell disease, RBC deformability affects lingering time and, consequently, partitioning.

In second part for the in vitro experiment, our investigation provides valuable insights into the behavior of RBCs in microfluidic channels, with a focus on their lateral migration, CFL, and partitioning at bifurcations. The key findings and implications of this study can be summarized as follows:

- **Lateral migration RBCs:** our research has illuminated differences in the behavior of RBCs within the mother channel and their subsequent impact on RBC distributions in the daughter vessels. Notably, we observed different focusing patterns for healthy and rigid RBCs in the mother channel. Healthy RBCs tended to concentrate near the channel walls, resulting in the emergence of two distinct peaks, whereas rigid RBCs predominantly flowed along the channel centerline. As these RBCs reached the bifurcation point, these discrepancy in their distribution persisted, influencing the RBC profiles within the daughter vessels and continuing until the end of the channel.

- **RBC partitioning at bifurcations:** The study observed that the partitioning of RBCs at bifurcations was influenced by factors such as the asymmetry of the bifurcation, flow rates in daughter vessels, and RBC deformability. The classical Zweifach-Fung effect, where the daughter vessel with the highest flow rate collects a higher Ht, was confirmed, but it was also noted that deformability could lead to deviations from this behavior at low Ht.

- **Characteristics of the CFL:** The formation and characteristics of the CFL, a region depleted of cells near the vessel wall, were investigated. The CFL thickness decreased with increasing Ht and was smaller for rigid RBCs compared to healthy RBCs. The CFL developing along the flow direction in the daughter branches was also analyzed, and it was found to depend on various factors, including RBC concentration, deformability, and flow rate.

5.1 Future prospects

In the first part for the in vivo experiment, we have identified a fascinating avenue of research that builds upon our current findings. Our research has highlighted the significant impact of RBC deformability on various aspects of blood flow dynamics. To further explore and validate these insights, we plan to embark on a new investigation. In this upcoming research, we intend to artificially rigidify RBCs using a substance such as diamide. These rigidified RBCs will then injected into the microvascular system of the hamster. To distinguish between rigid and healthy cells within the same network, we will employ different fluorescent dyes and wavelengths during microscopic analysis. This approach will allow us to gather data specifically for rigid and healthy RBCs within the same microvascular system. By comparing their behavior and distribution under different conditions and within the same physiological context, we aim to gain a deeper understanding of the functional differences between these two RBC populations. The insights derived from this research can have significant implications for various fields, including hematology, microfluidics, and biomedical engineering. We anticipate that this study will contribute to a more comprehensive understanding of the role of RBC deformability in vascular dynamics, potentially leading to advancements in the diagnosis and treatment of blood-related disorders and the design of more effective microfluidic devices.

In our continued pursuit of understanding the behavior of RBCs in microvascular networks, we have devised a novel experimental approach to further explore the dynamics of RBC partitioning after bifurcations, particularly in the context of asymmetrical CFL development. Our new microfluidic chips, as depicted in Fig. 5.1, feature a unique design that incorporates two consecutive T-junctions within the same microchannel system. The T-channel within this microfluidic chip maintains a height (H) of 50 ± 1 μm in the z-direction. It consists of an inlet channel, known as the mother channel, with a width (W_M) of 100 ± 1 μm and a length (L_M) of 2 cm in the flow direction. At the T-bifurcation, the mother channel splits into two daughter outlet channels, each with a width (W_D) of 50 ± 1 μm. However, we have introduced a deliberate variation in the lengths (L_D) of these daughter branches. Our configurations are as follows: For Fig. 5.1(a-c), L_D is equal to 2.5 mm, 5 mm, and 7.5 mm respectively. Subsequently, beyond the first bifurcation, the daughter branches split into two secondary daughter branches, each having the same width as the initial daughter branches (W_D). These secondary branches share a common length (L_{DD}) of 10 mm. The key distinction lies in the length of the daughter branches extending from the first bifurcation to the second bifurcation. This deliberate modification allows us to investigate a critical parameter: the minimum length required for the empirical model to accurately describe RBC partitioning at the second bifurcation. By systematically varying the length of these daughter branches and carefully controlling flow rates and Ht levels, we aim to establish empirical criteria that can effectively predict and explain the partitioning behavior observed in the second bifurcation. This empirical model will help us better grasp the complex interplay between RBC properties, flow dynamics, and microchannel geometries. This research endeavor

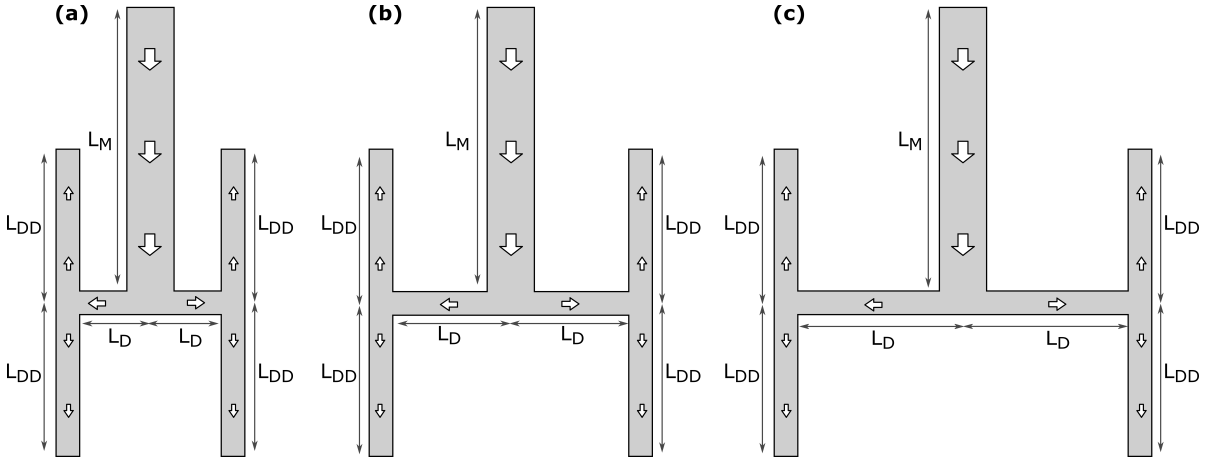

Figure 5.1: Microfluidic T-Junction Bifurcation with Two Consecutive Bifurcations in Sequence. Configuration variations include daughter branch lengths of, (a) $L_D = 2.5\ mm$, (b) $L_D = 5\ mm$, (c) $L_D = 7.5\ mm$

holds great promise in advancing our understanding of hemodynamics and RBC behavior in microvascular networks. It has the potential to yield valuable insights into the factors that influence RBC partitioning and distribution in real-world biological systems. Ultimately, our findings may contribute to the development of more accurate predictive models and innovative approaches for studying blood flow in health and disease.

Bibliography

[1] O. Baskurt, B. Neu, and H. J. Meiselman, "Red blood cell aggregation," 2011.

[2] D. A. Fedosov, B. Caswell, A. S. Popel, and G. E. Karniadakis, "Blood flow and cell-free layer in microvessels," *Microcirculation*, vol. 17, no. 8, pp. 615–628, 2010.

[3] T. W. Secomb, "Blood flow in the microcirculation," *Annual Review of Fluid Mechanics*, vol. 49, pp. 443–461, 2017.

[4] R. Hoffman, E. J. Benz Jr, L. E. Silberstein, H. Heslop, J. Anastasi, and J. Weitz, *Hematology: basic principles and practice*. Elsevier Health Sciences, 2013.

[5] A. S. Popel and P. C. Johnson, "Microcirculation and hemorheology," *Annu. Rev. Fluid Mech.*, vol. 37, pp. 43–69, 2005.

[6] K. Svanes and B. Zweifach, "Variations in small blood vessel hematocrits produced in hypothermic rats by micro-occlusion," *Microvascular Research*, vol. 1, no. 2, pp. 210–220, 1968.

[7] Y.-C. Fung, "Stochastic flow in capillary blood vessels," *Microvascular research*, vol. 5, no. 1, pp. 34–48, 1973.

[8] A. Krogh, "Studies on the physiology of capillaries: Ii. the reactions to local stimuli of the blood-vessels in the skin and web of the frog," *The Journal of physiology*, vol. 55, no. 5-6, p. 412, 1921.

[9] B. Klitzman and P. C. Johnson, "Capillary network geometry and red cell distribution in hamster cremaster muscle," *American Journal of Physiology-Heart and Circulatory Physiology*, vol. 242, no. 2, pp. H211–H219, 1982.

[10] A. Pries, K. Ley, M. Claassen, and P. Gaehtgens, "Red cell distribution at microvascular bifurcations," *Microvascular research*, vol. 38, no. 1, pp. 81–101, 1989.

[11] B. M. Fenton, R. T. Carr, and G. R. Cokelet, "Nonuniform red cell distribution in 20 to 100 μm bifurcations," *Microvasc. Res.*, vol. 29, pp. 103–126, jan 1985.

[12] J. M. Sherwood, E. Kaliviotis, J. Dusting, and S. Balabani, "Hematocrit, viscosity and velocity distributions of aggregating and non-aggregating blood in a bifurcating microchannel," *Biomech. Model. Mechanobiol.*, vol. 13, pp. 259–273, apr 2014.

[13] Z. Shen, G. Coupier, B. Kaoui, B. Polack, J. Harting, C. Misbah, and T. Podgorski, "Inversion of hematocrit partition at microfluidic bifurcations," *Microvascular research*, vol. 105, pp. 40–46, 2016.

[14] K. Yamamoto, H. Abe, C. Miyoshi, H. Ogura, and T. Hyakutake, "Study of the Partitioning of Red Blood Cells Through Asymmetric Bifurcating Microchannels," *J. Med. Biol. Eng.*, vol. 40, pp. 53–61, feb 2020.

[15] A. Mantegazza, F. Clavica, and D. Obrist, "In vitro investigations of red blood cell phase separation in a complex microchannel network," *Biomicrofluidics*, vol. 14, no. 1, p. 014101, 2020.

[16] A. Pskowski, P. Bagchi, and J. D. Zahn, "Investigation of red blood cell partitioning in an in vitro microvascular bifurcation," *Artificial organs*, vol. 45, no. 9, pp. 1083–1096, 2021.

[17] Q. Zhou, T. Perovic, I. Fechner, L. T. Edgar, P. R. Hoskins, H. Gerhardt, T. Krüger, and M. O. Bernabeu, "Association between erythrocyte dynamics and vessel remodelling in developmental vascular networks," *Journal of the Royal Society Interface*, vol. 18, no. 179, p. 20210113, 2021.

[18] P. Balogh and P. Bagchi, "The cell-free layer in simulated microvascular networks," *J. Fluid Mech.*, vol. 864, pp. 768–806, apr 2019.

[19] J. M. Sherwood, J. Dusting, E. Kaliviotis, and S. Balabani, "The effect of red blood cell aggregation on velocity and cell-depleted layer characteristics of blood in a bifurcating microchannel," *Biomicrofluidics*, vol. 6, p. 024119, jun 2012.

[20] A. R. Pries and T. W. Secomb, "Blood flow in microvascular networks," in *Microcirculation*, pp. 3–36, Elsevier, 2008.

[21] P. Balogh and P. Bagchi, "Direct numerical simulation of cellular-scale blood flow in 3d microvascular networks," *Biophysical journal*, vol. 113, no. 12, pp. 2815–2826, 2017.

[22] Y. Rashidi, G. Simionato, Q. Zhou, T. John, A. Kihm, M. Bendaoud, T. Krüger, M. O. Bernabeu, L. Kaestner, M. W. Laschke, *et al.*, "Red blood cell lingering modulates hematocrit distribution in the microcirculation," *Biophysical Journal*, vol. 122, no. 8, pp. 1526–1537, 2023.

[23] Q. Zhou, J. Fidalgo, M. O. Bernabeu, M. S. Oliveira, and T. Krüger, "Emergent cell-free layer asymmetry and biased haematocrit partition in a biomimetic vascular network of successive bifurcations," *Soft matter*, vol. 17, no. 13, pp. 3619–3633, 2021.

[24] Y. Rashidi, O. Aouane, A. Darras, T. John, J. Harting, C. Wagner, and S. M. Recktenwald, "Cell-free layer development and spatial organization of healthy and rigid red blood cells in a microfluidic bifurcation," *Soft Matter*, 2023.

[25] R. E. Waugh, M. Narla, C. W. Jackson, T. J. Mueller, T. Suzuki, and G. L. Dale, "Rheologic properties of senescent erythrocytes: loss of surface area and volume with red blood cell age," 1992.

[26] A. M. Forsyth, J. Wan, P. D. Owrutsky, M. Abkarian, and H. A. Stone, "Multiscale approach to link red blood cell dynamics, shear viscosity, and atp release," *Proceedings of the National Academy of Sciences*, vol. 108, no. 27, pp. 10986–10991, 2011.

[27] G. Deplaine, I. Safeukui, F. Jeddi, F. Lacoste, V. Brousse, S. Perrot, S. Biligui, M. Guillotte, C. Guitton, S. Dokmak, *et al.*, "The sensing of poorly deformable red blood cells by the human spleen can be mimicked in vitro," *Blood, The Journal of the American Society of Hematology*, vol. 117, no. 8, pp. e88–e95, 2011.

[28] I. V. Pivkin, Z. Peng, G. E. Karniadakis, P. A. Buffet, M. Dao, and S. Suresh, "Biomechanics of red blood cells in human spleen and consequences for physiology and disease," *Proceedings of the National Academy of Sciences*, vol. 113, no. 28, pp. 7804–7809, 2016.

[29] T. Junt, H. Schulze, Z. Chen, S. Massberg, T. Goerge, A. Krueger, D. D. Wagner, T. Graf, J. E. Italiano Jr, R. A. Shivdasani, *et al.*, "Dynamic visualization of thrombopoiesis within bone marrow," *Science*, vol. 317, no. 5845, pp. 1767–1770, 2007.

[30] R. K. Andrews, J. López, and M. C. Berndt, "Molecular mechanisms of platelet adhesion and activation," *The international journal of biochemistry & cell biology*, vol. 29, no. 1, pp. 91–105, 1997.

[31] Z. M. Ruggeri and G. L. Mendolicchio, "Adhesion mechanisms in platelet function," *Circulation research*, vol. 100, no. 12, pp. 1673–1685, 2007.

[32] Z. S. Kaplan and S. P. Jackson, "The role of platelets in atherothrombosis," *Hematology 2010, the American Society of Hematology Education Program Book*, vol. 2011, no. 1, pp. 51–61, 2011.

[33] A. Glenn and C. E. Armstrong, "Physiology of red and white blood cells," *Anaesthesia & Intensive Care Medicine*, vol. 20, no. 3, pp. 170–174, 2019.

[34] M. Brust, C. Schaefer, R. Doerr, L. Pan, M. Garcia, P. E. Arratia, and C. Wagner, "Rheology of Human Blood Plasma: Viscoelastic Versus Newtonian Behavior," *Phys. Rev. Lett.*, vol. 110, p. 078305, feb 2013.

[35] S. P. Sutera and R. Skalak, "The history of poiseuille's law," *Annual review of fluid mechanics*, vol. 25, no. 1, pp. 1–20, 1993.

[36] H. L. Goldsmith, G. R. Cokelet, and P. Gaehtgens, "Robin fahraeus: evolution of his concepts in cardiovascular physiology," *American Journal of Physiology-Heart and Circulatory Physiology*, vol. 257, no. 3, pp. H1005–H1015, 1989.

[37] Y. C. Fung and B. W. Zweifach, "Microcirculation: Mechanics of Blood Flow in Capillaries," *Annu. Rev. Fluid Mech.*, vol. 3, pp. 189–210, jan 1971.

[38] S. Chien, "Red cell deformability and its relevance to blood flow," *Annu. Rev. Physiol.*, vol. Vol. 49, pp. 177–192, 1987.

[39] G. R. Cokelet and H. L. Goldsmith, "Decreased hydrodynamic resistance in the two-phase flow of blood through small vertical tubes at low flow rates.," *Circ. Res.*, vol. 68, pp. 1–17, jan 1991.

[40] A. R. Pries, B. Reglin, and T. W. Secomb, "Structural response of microcirculatory networks to changes in demand: information transfer by shear stress," *American Journal of Physiology-Heart and Circulatory Physiology*, vol. 284, no. 6, pp. H2204–H2212, 2003.

[41] K. A. Dora, D. N. Damon, and B. R. Duling, "Microvascular dilation in response to occlusion: a coordinating role for conducted vasomotor responses," *American Journal of Physiology-Heart and Circulatory Physiology*, vol. 279, no. 1, pp. H279–H284, 2000.

[42] L. R. Dodd and P. C. Johnson, "Diameter changes in arteriolar networks of contracting skeletal muscle," *American Journal of Physiology-Heart and Circulatory Physiology*, vol. 260, no. 3, pp. H662–H670, 1991.

[43] C. Michel and F. Curry, "Microvascular permeability," *Physiological reviews*, 1999.

[44] A. S. Popel, P. C. Johnson, M. V. Kameneva, and M. A. Wild, "Capacity for red blood cell aggregation is higher in athletic mammalian species than in sedentary species," *Journal of applied physiology*, vol. 77, no. 4, pp. 1790–1794, 1994.

[45] M. L. Ellsworth and R. N. Pittman, "Evaluation of photometric methods for quantifying convective mass transport in microvessels," *American Journal of Physiology-Heart and Circulatory Physiology*, vol. 251, no. 4, pp. H869–H879, 1986.

[46] A. Nakano, Y. Sugii, M. Minamiyama, and H. Niimi, "Measurement of red cell velocity in microvessels using particle image velocimetry (piv)," *Clinical hemorheology and microcirculation*, vol. 29, no. 3-4, pp. 445–455, 2003.

[47] G. J. Tangelder, D. W. Slaaf, A. Muijtjens, T. Arts, M. Oude Egbrink, and R. S. Reneman, "Velocity profiles of blood platelets and red blood cells flowing in arterioles of the rabbit mesentery.," *Circulation Research*, vol. 59, no. 5, pp. 505–514, 1986.

[48] T. Secomb, R. Hsu, and A. Pries, "Blood flow and red blood cell deformation in nonuniform capillaries: effects of the endothelial surface layer," *Microcirculation*, vol. 9, no. 3, pp. 189–196, 2002.

[49] C. Pozrikidis, *Modeling and simulation of capsules and biological cells*. CRC Press, 2003.

[50] E. R. Damiano and T. M. Stace, "A mechano-electrochemical model of radial deformation of the capillary glycocalyx," *Biophysical Journal*, vol. 82, no. 3, pp. 1153–1175, 2002.

[51] A. R. Pries, T. W. Secomb, and P. Gaehtgens, "The endothelial surface layer," *Pflügers Archiv*, vol. 440, pp. 653–666, 2000.

[52] M. Cabel, H. J. Meiselman, A. S. Popel, and P. C. Johnson, "Contribution of red blood cell aggregation to venous vascular resistance in skeletal muscle," *American Journal of Physiology-Heart and Circulatory Physiology*, vol. 272, no. 2, pp. H1020–H1032, 1997.

[53] J. J. Bishop, A. S. Popel, M. Intaglietta, and P. C. Johnson, "Rheological effects of red blood cell aggregation in the venous network: a review of recent studies," *Biorheology*, vol. 38, no. 2-3, pp. 263–274, 2001.

[54] T. W. Secomb, B. Styp-Rekowska, and A. R. Pries, "Two-dimensional simulation of red blood cell deformation and lateral migration in microvessels," *Annals of biomedical engineering*, vol. 35, pp. 755–765, 2007.

[55] O. K. Baskurt and H. J. Meiselman, "Blood rheology and hemodynamics," in *Seminars in thrombosis and hemostasis*, vol. 29, pp. 435–450, Copyright© 2003 by Thieme Medical Publishers, Inc., 333 Seventh Avenue, New ..., 2003.

[56] R. Fåhraeus, "The Suspension Stability of Blood," *Physiol. Rev.*, vol. 9, pp. 241–274, apr 1929.

[57] R. Fåhræus and T. Lindqvist, "THE VISCOSITY OF THE BLOOD IN NARROW CAPILLARY TUBES," *Am. J. Physiol. Content*, vol. 96, pp. 562–568, mar 1931.

[58] C. Alonso, A. Pries, and P. Gaehtgens, "Time-dependent rheological behavior of blood at low shear in narrow vertical tubes," *American Journal of Physiology-Heart and Circulatory Physiology*, vol. 265, no. 2, pp. H553–H561, 1993.

[59] S. Kim, P. K. Ong, O. Yalcin, M. Intaglietta, and P. C. Johnson, "The cell-free layer in microvascular blood flow," *Biorheology*, vol. 46, no. 3, pp. 181–189, 2009.

[60] A. R. Pries, D. Neuhaus, and P. Gaehtgens, "Blood viscosity in tube flow: dependence on diameter and hematocrit," *American Journal of Physiology-Heart and Circulatory Physiology*, vol. 263, no. 6, pp. H1770–H1778, 1992.

[61] S. Yamaguchi, T. Yamakawa, and H. Niimi, "Cell-free plasma layer in cerebral microvessels," *Biorheology*, vol. 29, no. 2-3, pp. 251–260, 1992.

[62] J. O. Barber, J. P. Alberding, J. M. Restrepo, and T. W. Secomb, "Simulated two-dimensional red blood cell motion, deformation, and partitioning in microvessel bifurcations," *Annals of biomedical engineering*, vol. 36, pp. 1690–1698, 2008.

[63] N. Tateishi, Y. Suzuki, M. Soutani, and N. Maeda, "Flow dynamics of erythrocytes in microvessels of isolated rabbit mesentery: cell-free layer and flow resistance," *Journal of biomechanics*, vol. 27, no. 9, pp. 1119–1125, 1994.

[64] M. Soutani, Y. Suzuki, N. Tateishi, and N. Maeda, "Quantitative evaluation of flow dynamics of erythrocytes in microvessels: influence of erythrocyte aggregation," *American Journal of Physiology-Heart and Circulatory Physiology*, vol. 268, no. 5, pp. H1959–H1965, 1995.

[65] M. Sharan and A. S. Popel, "A two-phase model for flow of blood in narrow tubes with increased effective viscosity near the wall," *Biorheology*, vol. 38, no. 5-6, pp. 415–428, 2001.

[66] W. Reinke, P. Gaehtgens, and P. Johnson, "Blood viscosity in small tubes: effect of shear rate, aggregation, and sedimentation," *American Journal of Physiology-Heart and Circulatory Physiology*, vol. 253, no. 3, pp. H540–H547, 1987.

[67] A. Abay, S. M. Recktenwald, T. John, L. Kaestner, and C. Wagner, "Cross-sectional focusing of red blood cells in a constricted microfluidic channel," *Soft Matter*, vol. 16, no. 2, pp. 534–543, 2020.

[68] H. Amini, W. Lee, and D. Di Carlo, "Inertial microfluidic physics," *Lab Chip*, vol. 14, no. 15, p. 2739, 2014.

[69] Y. Suzuki, N. Tateishi, M. Soutani, and N. Maeda, "Flow behavior of erythrocytes in microvessels and glass capillaries: effects of erythrocyte deformation and erythrocyte aggregation," *International Journal of Microcirculation*, vol. 16, no. 4, pp. 187–194, 1996.

[70] A. R. Pries, T. Secomb, T. Gessner, M. Sperandio, J. Gross, and P. Gaehtgens, "Resistance to blood flow in microvessels in vivo.," *Circulation research*, vol. 75, no. 5, pp. 904–915, 1994.

[71] H. Goldsmith and S. Mason, "Axial migration of particles in poiseuille flow," *Nature*, vol. 190, no. 4781, pp. 1095–1096, 1961.

[72] D. A. Kihm, "Deformability-induced effects of red blood cells in flow," 2021.

[73] F. Azelvandre and C. Oiknine, "Effet fahraeus et effet fahraeus-lindqvist: resultats experimentaux et modeles theoriques," *Biorheology*, vol. 13, no. 6, pp. 325–335, 1976.

[74] J. H. Barbee and G. R. Cokelet, "Prediction of blood flow in tubes with diameters as small as 29 μ," *Microvascular Research*, vol. 3, no. 1, pp. 17–21, 1971.

[75] L. Bayliss, "Rheology of blood and lymph," *Deformation and flow in biological systems*, pp. 355–415, 1952.

[76] P. Gaehtgens, "Flow of blood through narrow capillaries: rheological mechanisms determining capillary hematocrit and apparent viscosity," *Biorheology*, vol. 17, no. 1-2, pp. 183–189, 1980.

[77] C. B. McKay and H. J. Meiselman, "Osmolality-mediated fahraeus and fahraeus-lindqvist effects for human rbc suspensions," *American Journal of Physiology-Heart and Circulatory Physiology*, vol. 254, no. 2, pp. H238–H249, 1988.

[78] A. A. Stadler, E. P. Zilow, and O. Linderkamp, "Blood viscosity and optimal hematocrit in narrow tubes," *Biorheology*, vol. 27, no. 5, pp. 779–788, 1990.

[79] M. F. Kiani and A. G. Hudetz, "A semi-empirical model of apparent blood viscosity as a function of vessel diameter and discharge hematocrit," *Biorheology*, vol. 28, no. 1-2, pp. 65–73, 1991.

[80] K. C. Warnke and T. C. Skalak, "The effects of leukocytes on blood flow in a model skeletal muscle capillary network," *Microvascular research*, vol. 40, no. 1, pp. 118–136, 1990.

[81] G. Segré and A. Silberberg, "Radial Particle Displacements in Poiseuille Flow of Suspensions," *Nature*, vol. 189, pp. 209–210, jan 1961.

[82] B. Ho and L. Leal, "Inertial migration of rigid spheres in two-dimensional unidirectional flows," *Journal of fluid mechanics*, vol. 65, no. 2, pp. 365–400, 1974.

[83] P. Vasseur and R. Cox, "The lateral migration of a spherical particle in two-dimensional shear flows," *Journal of Fluid Mechanics*, vol. 78, no. 2, pp. 385–413, 1976.

[84] D. Di Carlo, "Inertial microfluidics," *Lab Chip*, vol. 9, no. 21, p. 3038, 2009.

[85] E. S. Asmolov, "The inertial lift on a spherical particle in a plane poiseuille flow at large channel reynolds number," *Journal of fluid mechanics*, vol. 381, pp. 63–87, 1999.

[86] S. Berger, a. L. Talbot, and L. Yao, "Flow in curved pipes," *Annual review of fluid mechanics*, vol. 15, no. 1, pp. 461–512, 1983.

[87] A. J. Chung, "A minireview on inertial microfluidics fundamentals: Inertial particle focusing and secondary flow," *BioChip Journal*, vol. 13, pp. 53–63, 2019.

[88] W. A. Braff, M. Z. Bazant, and C. R. Buie, "Inertial effects on the generation of co-laminar flows," *Journal of Fluid Mechanics*, vol. 767, pp. 85–94, 2015.

[89] D. R. Gossett, H. T. K. Tse, J. S. Dudani, K. Goda, T. A. Woods, S. W. Graves, and D. Di Carlo, "Inertial manipulation and transfer of microparticles across laminar fluid streams," *Small*, vol. 8, no. 17, pp. 2757–2764, 2012.

[90] I. Bernhardt and J. C. Ellory, *Red cell membrane transport in health and disease*. Springer Science & Business Media, 2013.

[91] A. Bogdanova and L. Kaestner, "The red blood cells on the move!," 2018.

[92] F. Kogan, "Malaria burden," in *Remote Sensing for Malaria*, pp. 15–41, Springer, 2020.

[93] N. Mohandas and X. An, "Malaria and human red blood cells," *Medical microbiology and immunology*, vol. 201, no. 4, pp. 593–598, 2012.

[94] A. Dondorp, C. Ince, P. Charunwatthana, J. Hanson, A. v. Kuijen, M. Faiz, M. Rahman, M. Hasan, E. B. Yunus, A. Ghose, *et al.*, "Direct in vivo assessment of microcirculatory dysfunction in severe falciparum malaria," *The Journal of infectious diseases*, vol. 197, no. 1, pp. 79–84, 2008.

[95] A. M. Dondorp, P. A. Kager, J. Vreeken, and N. J. White, "Abnormal blood flow and red blood cell deformability in severe malaria," *Parasitology today*, vol. 16, no. 6, pp. 228–232, 2000.

[96] K. Peikert, A. Danek, and A. Hermann, "Current state of knowledge in chorea-acanthocytosis as core neuroacanthocytosis syndrome," *European journal of medical genetics*, vol. 61, no. 11, pp. 699–705, 2018.

[97] A. Darras, K. Peikert, A. Rabe, F. Yaya, G. Simionato, T. John, A. K. Dasanna, S. Buvalyy, J. Geisel, A. Hermann, *et al.*, "Acanthocyte sedimentation rate as a diagnostic biomarker for neuroacanthocytosis syndromes: experimental evidence and physical justification," *Cells*, vol. 10, no. 4, p. 788, 2021.

[98] A. Rabe, A. Kihm, A. Darras, K. Peikert, G. Simionato, A. K. Dasanna, H. Glaß, J. Geisel, S. Quint, A. Danek, *et al.*, "The erythrocyte sedimentation rate and its relation to cell shape and rigidity of red blood cells from chorea-acanthocytosis patients in an off-label treatment with dasatinib," *Biomolecules*, vol. 11, no. 5, p. 727, 2021.

[99] C. Siegl, P. Hamminger, H. Jank, U. Ahting, B. Bader, A. Danek, A. Gregory, M. Hartig, S. Hayflick, A. Hermann, *et al.*, "Alterations of red cell membrane properties in nneuroacanthocytosis," *PLoS One*, vol. 8, no. 10, p. e76715, 2013.

[100] M. J. Adjobo-Hermans, J. C. Cluitmans, and G. J. Bosman, "Neuroacanthocytosis: observations, theories and perspectives on the origin and significance of acanthocytes," *Tremor and Other Hyperkinetic Movements*, vol. 5, 2015.

[101] A. Farutin and C. Misbah, "Symmetry breaking and cross-streamline migration of three-dimensional vesicles in an axial poiseuille flow," *Physical review E*, vol. 89, no. 4, p. 042709, 2014.

[102] V. Doyeux, T. Podgorski, S. Peponas, M. Ismail, and G. Coupier, "Spheres in the vicinity of a bifurcation: elucidating the zweifach–fung effect," *Journal of Fluid Mechanics*, vol. 674, pp. 359–388, 2011.

[103] A. Kihm, S. Quint, M. W. Laschke, M. D. Menger, T. John, L. Kaestner, and C. Wagner, "Lingering dynamics in microvascular blood flow," *Biophysical journal*, vol. 120, no. 3, pp. 432–439, 2021.

[104] M. W. Laschke, B. Vollmar, and M. D. Menger, "The dorsal skinfold chamber: window into the dynamic interaction of biomaterials with their surrounding host tissue," *Eur Cell Mater*, vol. 22, no. 147, p. e64, 2011.

[105] X. Xu, S. Xu, L. Jin, and E. Song, "Characteristic analysis of otsu threshold and its applications," *Pattern recognition letters*, vol. 32, no. 7, pp. 956–961, 2011.

[106] I. F. Sbalzarini and P. Koumoutsakos, "Feature point tracking and trajectory analysis for video imaging in cell biology," *Journal of structural biology*, vol. 151, no. 2, pp. 182–195, 2005.

[107] M. O. Bernabeu, M. L. Jones, R. W. Nash, A. Pezzarossa, P. V. Coveney, H. Gerhardt, and C. A. Franco, "Polnet: A tool to quantify network-level cell polarity and blood flow in vascular remodeling," *Biophysical journal*, vol. 114, no. 9, pp. 2052–2058, 2018.

[108] Y. Sugii, R. Okuda, K. Okamoto, and H. Madarame, "Velocity measurement of both red blood cells and plasma of in vitro blood flow using high-speed micro piv technique," *Measurement science and Technology*, vol. 16, no. 5, p. 1126, 2005.

[109] X. Z. Jiang, M. S. Goligorsky, and K. H. Luo, "Cross talk between endothelial and red blood cell glycocalyces via near-field flow," *Biophysical Journal*, vol. 120, no. 15, pp. 3180–3191, 2021.

[110] C. Triebold and J. Barber, "Dependence of red blood cell dynamics in microvessel bifurcations on the endothelial surface layer's resistance to flow and compression," *Biomechanics and Modeling in Mechanobiology*, vol. 21, no. 3, pp. 771–796, 2022.

[111] S. Chien, C. D. Tvetenstrand, M. Epstein, and G. W. Schmid-Schonbein, "Model studies on distributions of blood cells at microvascular bifurcations," *American Journal of Physiology-Heart and Circulatory Physiology*, vol. 248, no. 4, pp. H568–H576, 1985.

[112] S. Ebrahimi and P. Bagchi, "A computational study of red blood cell deformability effect on hemodynamic alteration in capillary vessel networks," *Scientific reports*, vol. 12, no. 1, p. 4304, 2022.

[113] Z. Wang, Y. Sui, A.-V. Salsac, D. Barthès-Biesel, and W. Wang, "Path selection of a spherical capsule in a microfluidic branched channel: Towards the design of an enrichment device," *Journal of Fluid Mechanics*, vol. 849, pp. 136–162, 2018.

[114] J. Stuart and G. Nash, "Red cell deformability and haematological disorders," *Blood reviews*, vol. 4, no. 3, pp. 141–147, 1990.

[115] A. Dondorp, M. Nyanoti, P. Kager, S. Mithwani, J. Vreeken, and K. Marsh, "The role of reduced red cell deformability in the pathogenesis of severe falciparum malaria and its restoration by blood transfusion," *Transactions of the Royal Society of Tropical Medicine and Hygiene*, vol. 96, no. 3, pp. 282–286, 2002.

[116] A. Symeonidis, G. Athanassiou, A. Psiroyannis, V. Kyriazopoulou, K. Kapatais-Zoumbos, Y. Missirlis, and N. Zoumbos, "Impairment of erythrocyte viscoelasticity is correlated with levels of glycosylated haemoglobin in diabetic patients," *Clinical & Laboratory Haematology*, vol. 23, no. 2, pp. 103–109, 2001.

[117] R. Mannino, D. R. Myers, Y. Sakurai, R. E. Ware, G. Barabino, and W. Lam, "Increased erythrocyte rigidity is sufficient to cause endothelial dysfunction in sickle cell disease," *Blood*, vol. 120, no. 21, p. 818, 2012.

[118] F. Reichel, M. Kräter, K. Peikert, H. Glaß, P. Rosendahl, M. Herbig, A. Rivera Prieto, A. Kihm, G. Bosman, L. Kaestner, *et al.*, "Changes in blood cell deformability in chorea-acanthocytosis and effects of treatment with dasatinib or lithium," *Frontiers in Physiology*, p. 556, 2022.

[119] M. Faivre, M. Abkarian, K. Bickraj, and H. A. Stone, "Geometrical focusing of cells in a microfluidic device: an approach to separate blood plasma," *Biorheology*, vol. 43, no. 2, pp. 147–159, 2006.

[120] N. Xiang and Z. Ni, "High-throughput blood cell focusing and plasma isolation using spiral inertial microfluidic devices," *Biomedical microdevices*, vol. 17, no. 6, pp. 1–11, 2015.

[121] S. Tripathi, Y. V. B. Varun Kumar, A. Prabhakar, S. S. Joshi, and A. Agrawal, "Passive blood plasma separation at the microscale: a review of design principles and microdevices," *J. Micromechanics Microengineering*, vol. 25, p. 083001, aug 2015.

[122] V. Clavería, P. Connes, L. Lanotte, C. Renoux, P. Joly, R. Fort, A. Gauthier, C. Wagner, and M. Abkarian, "In vitro red blood cell segregation in sickle cell anemia," *Frontiers in Physics*, p. 712, 2021.

[123] C. Makena Hightower, B. Y. Salazar Vázquez, S. Woo Park, K. Sriram, J. Martini, O. Yalcin, A. G. Tsai, P. Cabrales, D. M. Tartakovsky, P. C. Johnson, *et al.*, "Integration of cardiovascular regulation by the blood/endothelium cell-free layer,"

Wiley Interdisciplinary Reviews: Systems Biology and Medicine, vol. 3, no. 4, pp. 458–470, 2011.

[124] S. Chien, S. Usami, R. J. Dellenback, and M. I. Gregersen, "Blood Viscosity: Influence of Erythrocyte Deformation," *Science (80-.).*, vol. 157, pp. 827–829, aug 1967.

[125] L. Lanotte, J. Mauer, S. Mendez, D. A. Fedosov, J.-M. M. Fromental, V. Claveria, F. Nicoud, G. Gompper, M. Abkarian, J. Mauer, D. A. Fedosov, G. Gompper, S. Mendez, F. Nicoud, and J.-M. M. Fromental, "Correction for Lanotte et al., Red cells' dynamic morphologies govern blood shear thinning under microcirculatory flow conditions," *Proc. Natl. Acad. Sci.*, vol. 113, pp. E8207–E8207, dec 2016.

[126] A. Passos, J. M. Sherwood, E. Kaliviotis, R. Agrawal, C. Pavesio, and S. Balabani, "The effect of deformability on the microscale flow behavior of red blood cell suspensions," *Phys. Fluids*, vol. 31, p. 091903, sep 2019.

[127] H. Fujiwara, T. Ishikawa, R. Lima, N. Matsuki, Y. Imai, H. Kaji, M. Nishizawa, and T. Yamaguchi, "Red blood cell motions in high-hematocrit blood flowing through a stenosed microchannel," *J. Biomech.*, vol. 42, pp. 838–843, may 2009.

[128] B. Kaoui, T. Krüger, and J. Harting, "How does confinement affect the dynamics of viscous vesicles and red blood cells?," *Soft Matter*, vol. 8, no. 35, p. 9246, 2012.

[129] G. Tomaiuolo, L. Lanotte, G. Ghigliotti, C. Misbah, and S. Guido, "Red blood cell clustering in Poiseuille microcapillary flow," *Phys. Fluids*, vol. 24, p. 051903, may 2012.

[130] C. Iss, D. Midou, A. Moreau, D. Held, A. Charrier, S. Mendez, A. Viallat, and E. Helfer, "Self-organization of red blood cell suspensions under confined 2D flows," *Soft Matter*, vol. 15, no. 14, pp. 2971–2980, 2019.

[131] E. Kaliviotis, J. M. Sherwood, and S. Balabani, "Partitioning of red blood cell aggregates in bifurcating microscale flows," *Sci. Rep.*, vol. 7, p. 44563, apr 2017.

[132] D. Bento, A. I. Pereira, J. Lima, J. M. Miranda, and R. Lima, "Cell-free layer measurements of in vitro blood flow in a microfluidic network: an automatic and manual approach," *Comput. Methods Biomech. Biomed. Eng. Imaging Vis.*, vol. 6, pp. 1–9, may 2017.

[133] D. Bento, C. Fernandes, J. Miranda, and R. Lima, "In vitro blood flow visualizations and cell-free layer (CFL) measurements in a microchannel network," *Exp. Therm. Fluid Sci.*, vol. 109, p. 109847, dec 2019.

[134] Q. Zhou, J. Fidalgo, M. O. Bernabeu, M. S. Oliveira, and T. Krüger, "Emergent cell-free layer asymmetry and biased haematocrit partition in a biomimetic vascular network of successive bifurcations," *Soft Matter*, vol. 17, no. 13, pp. 3619–3633, 2021.

[135] A. Abay, G. Simionato, R. Chachanidze, A. Bogdanova, L. Hertz, P. Bianchi, E. van den Akker, M. von Lindern, M. Leonetti, G. Minetti, C. Wagner, and L. Kaestner, "Glutaraldehyde – A Subtle Tool in the Investigation of Healthy and Pathologic Red Blood Cells," *Front. Physiol.*, vol. 10, pp. 1–14, may 2019.

[136] D. W. Inglis, "A method for reducing pressure-induced deformation in silicone microfluidics," *Biomicrofluidics*, vol. 4, no. 2, 2010.

[137] T. Gervais, J. El-Ali, A. Günther, and K. F. Jensen, "Flow-induced deformation of shallow microfluidic channels," *Lab on a Chip*, vol. 6, no. 4, pp. 500–507, 2006.

[138] J. Friend and L. Yeo, "Fabrication of microfluidic devices using polydimethylsiloxane," *Biomicrofluidics*, vol. 4, p. 026502, jun 2010.

[139] Q. Zhou, J. Fidalgo, L. Calvi, M. O. Bernabeu, P. R. Hoskins, M. S. Oliveira, and T. Krüger, "Spatiotemporal Dynamics of Dilute Red Blood Cell Suspensions in Low-Inertia Microchannel Flow," *Biophys. J.*, vol. 118, pp. 2561–2573, may 2020.

[140] S. C. Hur, H. T. K. Tse, and D. Di Carlo, "Sheathless inertial cell ordering for extreme throughput flow cytometry," *Lab Chip*, vol. 10, no. 3, pp. 274–280, 2010.

[141] A. T. Ciftlik, M. Ettori, and M. A. M. Gijs, "High Throughput-Per-Footprint Inertial Focusing," *Small*, vol. 9, pp. 2764–2773, aug 2013.

[142] J. Zhou and I. Papautsky, "Fundamentals of inertial focusing in microchannels," *Lab Chip*, vol. 13, no. 6, p. 1121, 2013.

[143] T. M. Geislinger and T. Franke, "Hydrodynamic lift of vesicles and red blood cells in flow — from Fåhræus & Lindqvist to microfluidic cell sorting," *Adv. Colloid Interface Sci.*, vol. 208, pp. 161–176, jun 2014.

[144] S. Tanaka and M. Sugihara-Seki, "Inertial focusing of red blood cells suspended in square capillary tube flows," *Journal of the Physical Society of Japan*, vol. 91, no. 8, p. 083401, 2022.

[145] M. Sugihara-Seki and N. Takinouchi, "Margination of platelet-sized particles in the red blood cell suspension flow through square microchannels," *Micromachines*, vol. 12, no. 10, p. 1175, 2021.

[146] D. Oh, S. Ii, and S. Takagi, "Numerical study of particle margination in a square channel flow with red blood cells," *Fluids*, vol. 7, no. 3, p. 96, 2022.

[147] M. Masaeli, E. Sollier, H. Amini, W. Mao, K. Camacho, N. Doshi, S. Mitragotri, A. Alexeev, and D. Di Carlo, "Continuous inertial focusing and separation of particles by shape," *Physical Review X*, vol. 2, no. 3, p. 031017, 2012.

[148] Y. Chen, D. Li, Y. Li, J. Wan, J. Li, and H. Chen, "Margination of stiffened red blood cells regulated by vessel geometry," *Scientific reports*, vol. 7, no. 1, pp. 1–9, 2017.

[149] S. R. Bazaz, A. Mashhadian, A. Ehsani, S. C. Saha, T. Krüger, and M. E. Warkiani, "Computational inertial microfluidics: A review," *Lab on a Chip*, vol. 20, no. 6, pp. 1023–1048, 2020.

[150] S. M. Recktenwald, K. Graessel, F. M. Maurer, T. John, S. Gekle, and C. Wagner, "Red blood cell shape transitions and dynamics in time-dependent capillary flows," *Biophys. J.*, vol. 121, pp. 23–36, jan 2022.

[151] A. Merlo, M. Berg, P. Duru, F. Risso, Y. Davit, and S. Lorthois, "A few upstream bifurcations drive the spatial distribution of red blood cells in model microfluidic networks," *Soft Matter*, vol. 18, no. 7, pp. 1463–1478, 2022.

[152] D. Katanov, G. Gompper, and D. A. Fedosov, "Microvascular blood flow resistance: Role of red blood cell migration and dispersion," *Microvasc. Res.*, vol. 99, pp. 57–66, may 2015.

[153] J. M. Sherwood, D. Holmes, E. Kaliviotis, and S. Balabani, "Spatial Distributions of Red Blood Cells Significantly Alter Local Haemodynamics," *PLoS One*, vol. 9, p. e100473, jun 2014.

[154] E. Kaliviotis, D. Pasias, J. Sherwood, and S. Balabani, "Red blood cell aggregate flux in a bifurcating microchannel," *Med. Eng. Phys.*, vol. 48, pp. 23–30, oct 2017.

[155] E. Kaliviotis, J. M. Sherwood, and S. Balabani, "Local viscosity distribution in bifurcating microfluidic blood flows," *Phys. Fluids*, vol. 30, p. 030706, mar 2018.

[156] X. Yin, T. Thomas, and J. Zhang, "Multiple red blood cell flows through microvascular bifurcations: cell free layer, cell trajectory, and hematocrit separation," *Microvascular research*, vol. 89, pp. 47–56, 2013.

[157] J. Zhang, P. C. Johnson, and A. S. Popel, "Effects of erythrocyte deformability and aggregation on the cell free layer and apparent viscosity of microscopic blood flows," *Microvascular research*, vol. 77, no. 3, pp. 265–272, 2009.

[158] G. Li, T. Ye, B. Yang, S. Wang, and X. Li, "Temporal-spatial heterogeneity of hematocrit in microvascular networks," *Phys. Fluids*, vol. 35, p. 021906, feb 2023.

Acknowledgments

I would like to express my deep gratitude to Prof. Dr. Christian Wagner for the invaluable opportunity he granted me to embark on my Ph.D. journey under his guidance. I also extend my heartfelt thanks to Dr. Alexis Darras and Dr. Steffen M. Recktenwald for always being available for scientific questions and for their invaluable assistance.

My thanks extend to every member of the research group, with whom I shared memorable moments during my Ph.D. years: Prof. Lars Kaestner, Dr. Thomas John, Dr. Andreas Tschöpe, Dr. Alexander Kihm, Dr. Jorge Fiscina, Dr. Greta Simionato, Dr. Stephan Quint, Dr. Rishab Handa, Min Qiao, Marcelle Lopez, Felix Milan Maurer, Mohammed Bendaoud, Mohammed Nouaman, Khadija Larhrissi, Nils Boussard, Agatha Pinto Pino, Vahideh Sardari and to those whom I may unintentionally omit. I also wish to express my thanks to Prof. Dr. Chaouqi Misbah at the LiPhy lab in Grenoble University and Prof. Romen Rodriguez at the University of Barcelona for providing me with the opportunity to work with them as part of my secondment. I'm truly grateful for this experience. Elke Huschens , Nina Apfelbaum, Sara Zimmermann, and Karin Kretsch's support with paperwork and chemical preparations was invaluable.

I'm deeply appreciative of the time and effort put in by the proofreaders who provided valuable feedback on my thesis.

Last but certainly not least, my deepest and most sincere appreciation goes to my wife, my parents and sisters and brother for their unwavering support, boundless encouragement, and unconditional love throughout my academic journey.